UC Berkeley

UC Berkeley Electronic Theses and Dissertations

Title

Highly Scalable Silicon Photonic Switches Based on Waveguide Crossbar with Movable Waveguide Couplers

Permalink

Author

Han, Sangyoon

Publication Date

2016

Peer reviewed|Thesis/dissertation

**Highly Scalable Silicon Photonic Switches
Based on Waveguide Crossbar with Movable Waveguide Couplers**

By

Sangyoon Han

A dissertation submitted in partial satisfaction of the

requirements for the degree of

Doctor of Philosophy

in

Engineering – Electrical Engineering and Computer Sciences

in the

Graduate Division

of the

University of California, Berkeley

Committee in charge:

Professor Ming C. Wu, Chair
Professor Richard S. Muller
Professor Liwei Lin

Spring 2016

Abstract

Highly scalable silicon photonic switches
based on waveguide crossbar with movable waveguide couplers

by

Sangyoon Han

Doctor of Philosophy in Engineering – Electrical Engineering and Computer Sciences

University of California, Berkeley

Professor Ming C. Wu, Chair

Fast optical-circuit-switches (OCS) having a large number of ports can significantly enhance the performance and the efficiency of modern data centers by actively rearranging network patterns. Commercially available optical switches typically operate with the use of moving mirror arrays. These switches can have port counts exceeding 100x100 and insertion losses lower than a few dBs. However, their switching speeds are typically tens-of-milliseconds which limits their applications in highly dynamic traffic patterns. Moreover, the moving-mirror-based optical switches make use of free-space optics that requires manual assembly and, as a result, the costs are high.

Recently, optical switches based on silicon photonics technology have been designed and built. Silicon photonics technology provides an attractive platform for optical switches. In them, light is tightly confined in silicon waveguides due to its high refractive index. The tight confinement allows dense integrations of switch components. By leveraging complementary-metal-oxide-semiconductor (CMOS) fabrication processes, large scale integrated optical circuits can be made at relatively low cost in high volume. Silicon photonic switches with microsecond or nanosecond response times have been demonstrated using thermo-optic effects or electro-optic effects, and silicon photonic switches with integrated CMOS driving circuits have been demonstrated. However, the demonstrations were mostly limited to a small number of ports. This limitation is mainly due to the switch architecture used, which scales port counts by connecting 2x2 switching units serially. In this architecture, switching loss increases rapidly as the number of connected units increases.

In this dissertation, I investigate a new architecture for silicon photonic switches that is highly scalable. The architecture is based on a waveguide crossbar having moving waveguide couplers that configure light paths, so that there is only one switching stage for any given light path regardless of port count. As a result, switching loss does not accumulate as port count increases.

I compare scaling prospects for this architecture with those of previously designed silicon-photonic-switch architectures.

I then investigate three implementations of silicon-photonic-switches that use the proposed architecture. First, the experimental demonstration of a 50x50 silicon photonic switch which I identify as Generation-A (Gen-A) is shown. In Gen-A a vertically moving directional coupler is designed for switching operations, and an electrostatic-cantilever-actuator is designed to move the directional coupler. A waveguide-crossing with ultra-low-optical-loss is designed to minimize crossbar losses. The 50x50 Gen-A switch is monolithically integrated in a chip with less than 9 x 9 mm^2 of area. The response time of the Gen-A switch is 2.5 µs, and its actuation voltage is 14 V.

Second, a silicon-photonic-switch identified as Gen-B that provides point-to-multipoint connections is researched. Laterally moving directional couplers are designed for more precise switching operation than Gen-A. The laterally moving directional couplers in Gen-B direct optical power only to receivers that are meant to subscribe to the sender, unlike broadcast-and-select type switches which waste optical power by sending it to all receivers. The Gen-B switch is demonstrated in 1-to-2 and 1-to-4 switching operations. The response time of the Gen-B switch is 9.6 µs, and its actuation voltage is 10 V.

Finally I present a third case (Gen-C), a design for a silicon-photonic-switch that can process signals having various incoming polarizations is shown. In Gen-C, waveguides are designed to support both TE- and TM-modes, and the two-layer waveguide crossbar is used to eliminate completely any waveguide-crossing losses. The adiabatically tapered waveguide couplers in Gen-C are designed to switch both TE- and TM-modes at the same time while Polarization-Dependent-Loss (PDL) is held to 0.5 dB. The single-stage and two-stage parallel-plate-type electrostatic actuators in Gen-C are specifically designed for digital switching operation.

To my family

Table of Contents

List of Figures

Acknowledgements

I would like to thank my advisor Professor Ming C. Wu for his support and guidance for my graduate study in Berkeley. Without his guidance, I could not make this far. I could become a researcher by watching him and by interacting with him. He has been a great role model showing me how a researcher should think, act, and live.

I would also like to thank Professor Richard S. Muller for his thoughtful discussion and support for this silicon photonic-switch project. His support for the project helped me reaching further with the project. I would like to thank Professor Liwei Lin for serving on my qualifying exam committee and my thesis committee. I would also like to thank Professor Constance Chang-Hasnain for serving on my qualifying exam committee.

There are so many labmates who helped me along the way. I would like to thank my labmates for their friendships and inspirations. Especially, I would like to thank Dr. Tae Joon Seok for being a great senior, and a great mentor. I have learned much important knowledge and many reseach skills from him. His presence inspired me in many ways. I also want to thank Professor Niels Quack for his friendship and mentoring. With his mentoring, I could get on the right track in my graduate study. I would like to thank Dr. Byung-wook Yoo for guiding and mentoring me to become a robust engineer. I learned many important experimental skills from him. I thank Professor Myung-Ki Kim for helping me building a theoretical background.

I also would like to thank Professor Chang-kyu Kim for the advice he provided during his sabbatical stay in Berkeley. His advices encouraged me to move forward. I want to thank Karen Grutter for teaching me her fabrication skills. Her advices on fabrications helped me to find shortcuts. I would like to thank Dr. James Ferrara for his friendship and for teaching me how to live a happy daily life in graduate school. I would also like to thank Phil Sandborn for being a good friend and for having inspiring discussions. I thank Dr. Youmin Wang for being a good friend and for discussions regarding fabrication process. I thank the entire Ming Wu lab members for their support. Especially, I want to thank Professor Kyoung Sik Yu, Anthony Yeh, Dr. Shao Ning Pei, Dr. Jeffery Chou, Dr. Ryan Going, Dr. Michael Eggleston, Dr. Alex Grine, Jeremy Beguelin, Jodi Loo, Kevin Han, Dr. Meer Nazmus Sakib, Dr. Yung Hsiang Lin, and Jean-Etienne Tremblay. I also want to thank Shirely Salanio for her kind and thoughtful advice regarding graduate student matters.

I would like to thank the Korea Foundation for Advanced Studies, CIAN NSF-ERC, and E3S for their generous support. Without funding, I would never have achieved my Ph.D. degree.

Finally, I would like to thank my mom, dad, and brother for their love, support, and advice.

Chapter 1

Introduction

Optical switches are essential building blocks for optically connected networks. They allow dynamic rearrangement of network patterns by exchanging connections between optical links. Since the inventions of optical fiber in mid-20th century, development of fast and scalable optical switches has been a thriving topic in the optical communication community. There have been extensive implementations of optical switches made using various approaches in the last few decades.

One of the most prominent earlier approaches was based on moving micro mirrors. It made use of Micro-Electro-Mechanical-System (MEMS) actuators to move the mirrors and thereby to deflect free-space optical beams between optical fibers for switching. Several world-leading research groups including those at Bell Laboratory [1,2], NTT [3], and Fujitsu [4] pioneered this approach in the 1990s and early 2000s, and their work has led to several successful commercialized products. Optical switches based on this approach generally have high port counts (some exceed 100x100 ports) with low insertion losses (less than 4 dB). An example is the optical switch reported from Bell Laboratory in 2003 [1] which had port count of 1100x1100 and maximum insertion loss of 4 dB. These optical switches have found use in telecommunication networks and data-communication networks that transfer large bandwidth data over long distances.

Despite the major efforts invested in micro-mirror based approaches, the response times have been limited to the range of tens of milliseconds. This limitation results from fundamental tradeoff between the port count and the resonant frequencies of the MEMS actuators [5]. The distance that an optical beam needs to travel increases as the port count increases. In order to keep optical losses and crosstalk levels unchanged while increasing the travel distance of the beam, the size of the beam waist needs to increase. To reflect the larger beam waist, the size of the mirror needs to be larger as well. As a result, mirror masses increase, and therefore the resonant frequencies of the MEMS actuators decrease. Moreover, the optical switches have high manufacturing costs and large sizes due to their free-space optical components.

Because of slow speeds, high costs, and large sizes of the optical switches, a large set of optical networks still rely on electrical switching for which devices are faster, cheaper, and smaller than the optical switches. However, there is a drawback to using electrical switches in optical networks.

To switch optical signals using electrical switches, optical-electrical-optical (OEO) conversions are needed, and the conversions require extra costs and energy. Data centers provide well-known examples of having this drawback. Data centers use optical fibers for communication between large numbers of servers, but the centers typically rely on electrical switching. As a result, a large number of transceivers for optical-electrical-optical (OEO) conversion are required. These are expensive both in money and power. Moreover, electrical switches typically support fixed-data-rates so that frequent upgrades may be needed as data centers evolve to higher data rates. Thus, using optical switches instead of electrical switches is fundamentally more desirable for so long as the performance and the cost of optical switches are comparable. Besides data centers, intra-chip optical communications [6–9], optical imaging [10], and quantum computing [11] are potentially other applications for optical switches if they can be integrated into chip-scale size with significantly fast response times.

Integrated-optics technology offers an alternative approach to the use of actuated micro mirrors for build optical switches. Integrated optics employs waveguides rather than free-space for the propagation of light. Silicon photonics technology is one of the promising candidate for realizing integrated optics [12–20]. This is a technology that uses silicon as an optical medium and for device fabrications leverages complementary-metal-oxide-semiconductor (CMOS) processing technology [21,22]. Thanks to the large refractive index of silicon (3.48 at 1550 nm wavelength), optical modes can be tightly confined to have small device footprints. Cross-sectional areas of typical silicon waveguides are usually less than 1 μm^2, and the guides can be bent to radii smaller than 10 μm. Because silicon photonics technology utilizes CMOS processing technology, monolithic integration with driving electronics is possible. CMOS fabrication techniques are already at a very mature level and it is therefore very beneficial to fabricate silicon photonic elements compatibly with CMOS electronics.

Silicon photonics offers several components that are favorable to build integrated optical switches, and silicon waveguides provide optical paths in the switches having low optical losses. State-of-the-art silicon waveguides presently exhibit optical losses lower than 0.1 dB/cm [23], and we can expect further improvement in this number. Grating couplers allow efficient coupling between silicon waveguides and optical fibers. State-of-the-art grating couplers in silicon photonics have optical losses less than 0.5 dB [24]. Optical modulators allow modulation of light and the modulation enables switching operations. Optical modulators that operate at GHz speeds are available in silicon photonics platforms [25] [26].

Figure 1.1 (a) shows a switching unit made using conventional silicon photonic switches. The switching unit is a waveguide-based Mach-Zehnder Interferometer (MZI). In the MZI, light inserted in either of the inputs splits into the two waveguide arms with equal amounts of power. After going through the waveguide arms, the light from the two arms recombines at the combiner. Depending on the phase difference of the two light paths in the two waveguide arms, light will select its path either to output 1 or output 2. The optical phase modulator at the top waveguide arm modulates the phase difference of the two light paths by modulating the refractive index of the top waveguide arm. The refractive index of the waveguide arm is modulated either by heating the waveguides or by injecting carriers into them. Silicon photonic switches with microsecond

response time have been demonstrated using the heating method [27–30] while switches with nanosecond response time have been demonstrated using the carrier-injection method [31,32].
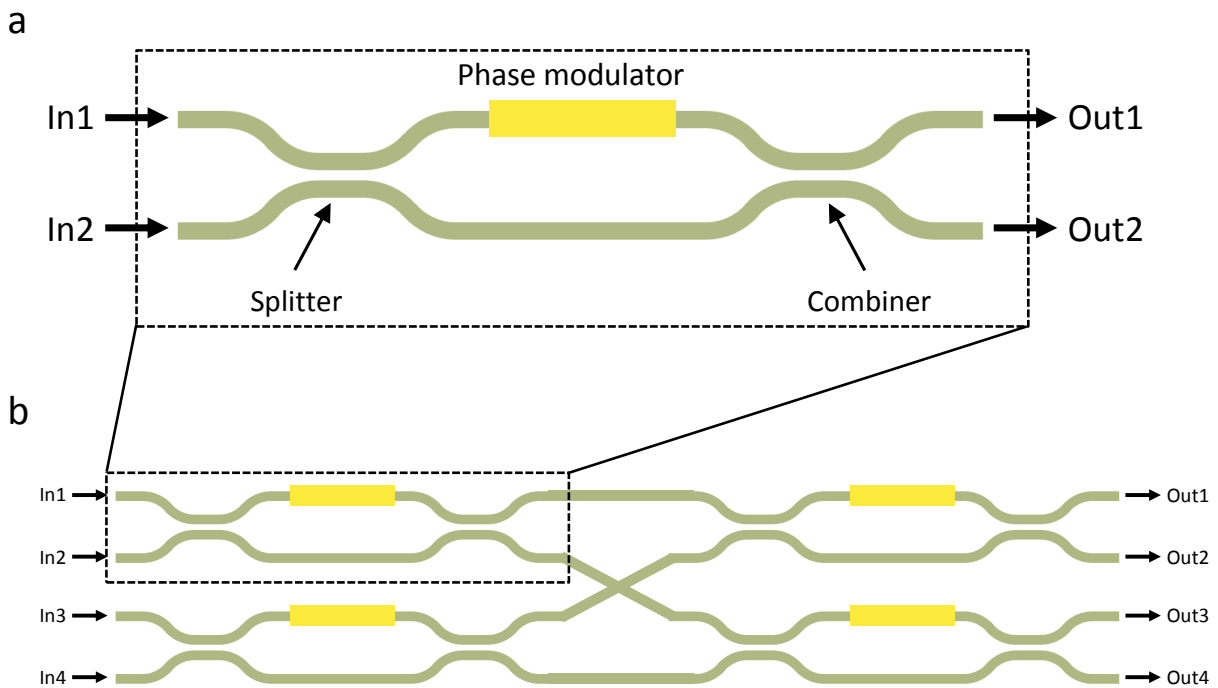
Figure 1.1 Schematics of MZI based silicon photonic switches. (a) switching unit. (b) cascaded 4x4 switch.

Because the silicon waveguides are small, the thermal masses and the cross-sectional areas of the waveguides are also small. As a result, heating-and-cooling or injecting-and-withdrawing can be done in microsecond-times or in nanosecond-times respectively. Thus response times of MZI silicon photonic switches are several orders-of-magnitude smaller than response times in the micro-mirror-based optical switches. Although the MZI silicon photonic switches have shorter response times, the port count numbers are significantly reduced compared to those achieved in mirror-based optical switches. State-of-the-art MZI silicon photonic switches typically have port counts no larger than 8x8 [27–32]. This limitation occurs because the optical losses of the switches increases rapidly as the port count increases. The MZI silicon photonic switches increase their port count by cascading the MZI based switching units (Figure 1.1 (b)). Since each switching unit has a finite optical loss in each switching operation (typically around 0.25 dB) optical loss accumulates as the cascading order increases.

Instead of the MZIs, one can build optical switches with moving waveguides [33,34]. One can switch light between two parallel waveguides by controlling a gap between the two (Figure 1.2). This mechanism is explained in detail in Chapter 2 and Chapter 3. Here, I briefly introduce the concept. When two symmetric waveguides are placed very close to each other, light energy from one waveguide can couple into the other by an evanescent coupling mechanism [35]. When the closely spaced guides extend coupling length, 100 % of the light can be transferred from one

waveguide to the other by controlling the gap spacing (Figure 1.2 (a)). On the other hand, by having a sufficiently large gap spacing, one can suppress the optical coupling between the two waveguides and thus have virtually no optical power transferred from one to the other (Figure 1.2 (b)). Thus by using this method, one can build a switching unit that is much simpler (e.g. employ fewer optical components). With the simple switching method, one can start devising a new switch architecture that is potentially more scalable than that based on cascaded MZI switches.
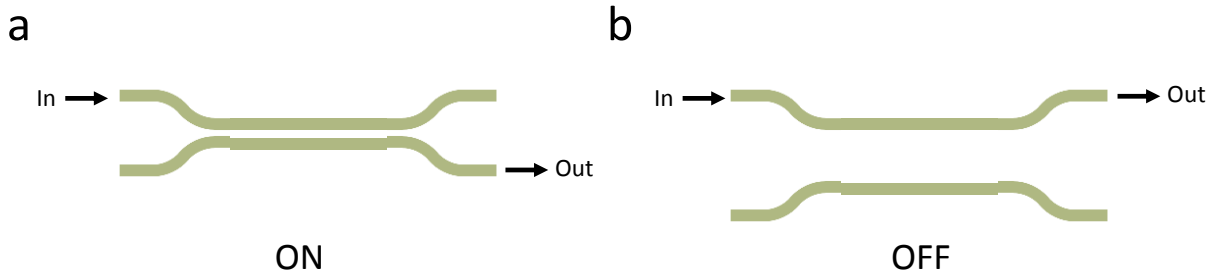
Figure 1.2 Switching method by moving a waveguide to permit or to disallow evanescent coupling. (a) ON-state. (b) OFF-state.

There have been a few demonstrations of silicon photonic switches with moving waveguides [34,36–38]. However, the architectures used in these switches are still similar to those used for the MZI-based switches and thus these switches still have relatively small port counts (such as 2x6 [38]).

In this thesis, I present highly scalable optical switches based on moving waveguides. Figure 1.3 shows the conceptual schematic of the switches, each of which has. The switches have a passive waveguide crossbar that defines the default light paths in the switch. At each grid of the crossbar, there are two movable-waveguide-couplers that configure switchable switchable light paths. The two couplers are connected through 90-degree bends and are located far enough from the crossbar to prevent having optical coupling. When the couplers come sufficiently close to the waveguides in the crossbar to have optical coupling, evanescent optical fields of the coupler waveguides allow transfer of optical power from the coupler waveguides to the crossbar waveguides. In this way, one can switch light from n-th port to m-th port by moving the couplers in cell <n,m> close to the crossbar waveguides (Figure 1.3). The striking advantage of this switch architecture is that any light path in the switch passes through only one set of the couplers. In this way, switching losses at the couplers add only once regardless of the switch's port count. In other words, switching loss does not scale as the port count increases and we can build optical switches having much larger port count without having high optical losses. Now, the only optical losses that scale as the port count are losses from the waveguides and loss from the waveguide crossings. However, optical losses from the waveguides are mostly induced from roughness at the waveguide sidewalls which can be held to acceptable amounts by optimizing designs [23,39] of the waveguides or by optimizing their fabrication processes. Silicon waveguides having optical losses lower than 0.1 dB/cm have already been fabricated. Waveguide crossings having roughly

0.01 dB of optical loss have been reported [40] [41], and the waveguide crossings can be completely eliminated with more sophisticated designs for example two-layer-waveguide designs [42] [43].
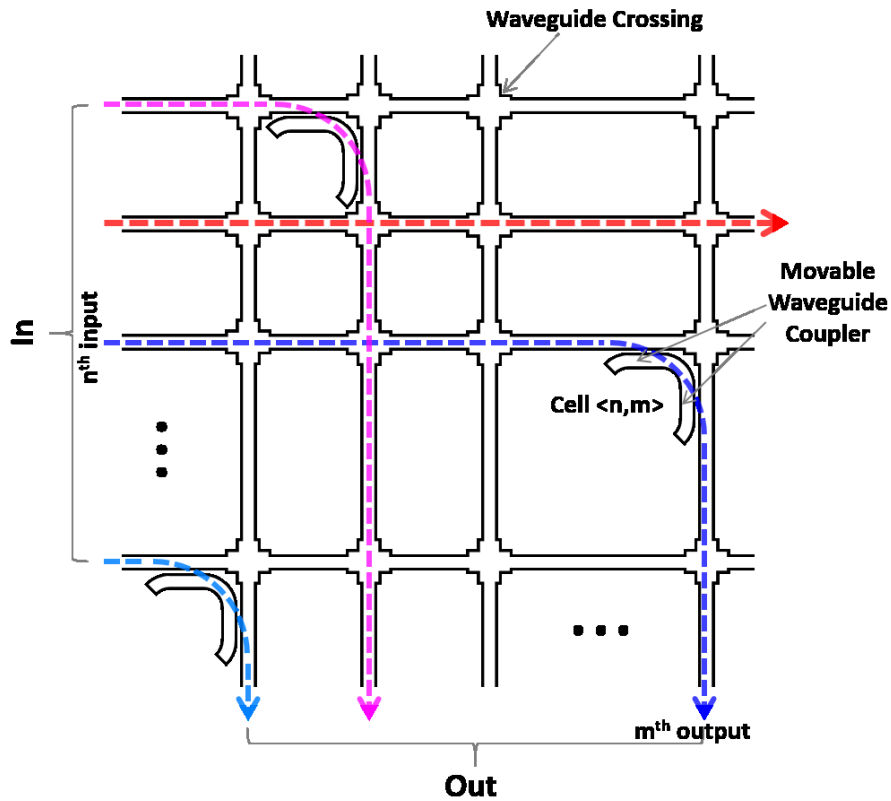
Figure 1.3 Proposed silicon photonic switch architecture: waveguide crossbar with movable waveguide couplers.

Table 1-1 compares the number of components (waveguide crossings and switching elements) needed for our proposed architecture to those present in two prominent MZI-based-architectures when considering their worst-case-switching-paths. Here, the numbers are taken from [44], and worst-case-switching-path means a light path in a switch-array that includes the maximum numbers of waveguide crossings and of switching elements. As listed in Table 1-1, only in our proposed architecture is there only one switching element regardless of the port count N. In Figure 1.4, the optical losses of the longest paths in the different switch architectures are plotted with different port counts. Here, I assumed the optical loss of each waveguide crossing and each switching element is 0.01 dB and 0.25 dB, respectively. As shown from Figure 1.4, for 100x100 switches, the optical losses of MZI-based switches exceed 25 dB. On the other hand, the optical losses of our proposed architecture stay below 2 dB.

5

Table 1-1 Number of waveguide crossings and switching elements in different architectures.

Architecture		Switching elements (maximum number)	Waveguide crossings (maximum number)
Proposed architecture		1	2N-2
MZI-based	PILOSS [29]	N	N-1
	Switch-and-select [27]	$2\log_2 N$	N^2-N
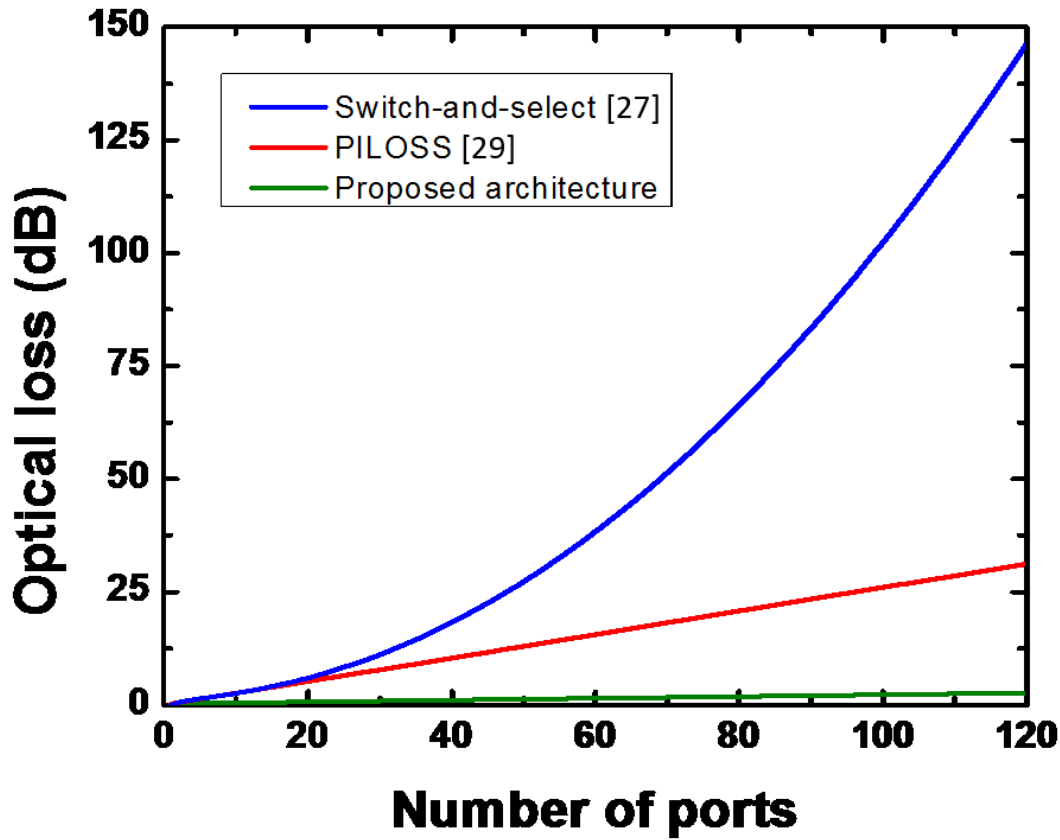
Figure 1.4 Optical loss *vs* Number of ports; comparison between our proposed architecture and the architectures presented in [27] and [29].

In Chapter 2, an experimental demonstration of a 50x50 silicon photonic switch (Gen-A) with microsecond response time is described. This demonstration is the first experimental implementation of our proposed architecture. This switch had the largest port count among the all silicon photonic switches reported at the time it was demonstrated. In chapter 3, a silicon photonic switch that allows point-to-multipoint (Gen-B) is presented. It provides an example of derivatives of our proposed architecture. Gen-B was implemented in 4x20 port count that is smaller scale than that of Gen-A. This was only because we shared fabrication mask space with other projects so that we needed to shrink the area for Gen-B. Optical loss per cell has been

reduced by nearly three times in Gen-B compared to Gen-A. In chapter 4, I show a specific design for a silicon photonic switch that has a two-layer waveguide crossbar and can switch light with any incoming polarization. Since optical fibers carry light with all possible polarization states, the ability to handle any incoming polarization is essential for practical applications.

Chapter 2

50x50 silicon-photonic-switch-array on a waveguide-crossbar with vertically actuated directional couplers

Optical Circuit Switches (OCS) can help data center networks to use their full bandwidth capacity by reconfiguring network topology according to traffic demand. At the present time, micro-mirror-based 3D-MEMS-switches are the most prominent commercially available systems. They use a pair of 2-axis micro-mirror arrays to direct input from a two-dimensional array of fibers to any output in similarly dimensioned arrays [45]. Switches having 1100 ports have been reported [1], and 320x320 switches are commercially available [46]. Other large-scale switches use individual piezoelectric actuators to align fiber collimators [47]. The response times of these switches are on the order of 10 ms. They are based on free-space optics, which requires precision assembly, and as a result, their costs are high.

Integrated photonic switches can potentially reduce the cost by orders-of-magnitude. Switches based on Planar-Lightwave-Circuits (PLC) are one of the most mature integrated photonic switches. Optical switches having 32x32 ports and insertion losses of 6.5 dB have been reported [48]. However, the switch sizes are nearly 10 cm x 10 cm. Moreover, switching is done by tuning the refractive indices of SiO_2 waveguides by heating-and-cooling. As a result, the switches need to dissipate high power from joule heating. Semiconductor-optical-amplifier (SOA) based switches have also been reported. In these, switching is done by amplifying-and-attenuating input-optical-signals. As a result, SOAs consumes high power for amplification and they add noise to the optical signal [49–51].

Silicon photonics offers an attractive alternative for integrated photonic switches [6,7,9,13,14,16,17,19–22,52–55]. Light is tightly confined in silicon due to its high refractive index [56,57]. The nanometer-scale waveguides are sometimes called "photonic wires." By leveraging on advanced complementary-metal-oxide-semiconductor (CMOS) fabrication processing, very large scale silicon photonic integrated circuits can be made economically in high volume. Silicon photonic switches with microsecond [27–30] or nanosecond [31,32] response times have been built on the same chips as integrated CMOS driving circuits [58,59]. However,

8

almost all the cited demonstrations were limited to relatively low port counts. This limitation is mainly due to their cascaded 2x2 architecture which leads to relatively high optical loss that grows with port counts.

In this chapter, we report on a 50x50-port silicon photonic switch. We designed and implemented the switch based on the architecture that we proposed in Chapter 1. The switch had the largest port count among all silicon photonic switches presented at the time it was demonstrated. A 50x50 silicon photonic switch has been integrated on a die area of 9x9 mm², with a switching voltage of 14 V and a switching time of 2.5 μs.

2.1 Design of Switch Generation-A

Figure 2.1 illustrates the architecture of the 50x50 switch which has a design similar to that of a crossbar network [60]. The network is terminated with grating couplers [61,62] to optical fibers. At each node of the crossbar, there are switching cells that configure light paths (Figure 2.1 (b)). The switch cells have two states, a drop-state and a through-state. In the through-state, the light from the input port propagates to a through port. In the drop-state, the light from the input port makes a 90-degree turn and propagates to a drop port. By coordinating the states of the cells, light from any input fiber can be switched to any output fiber. We identify this switch as switch Generation-A.
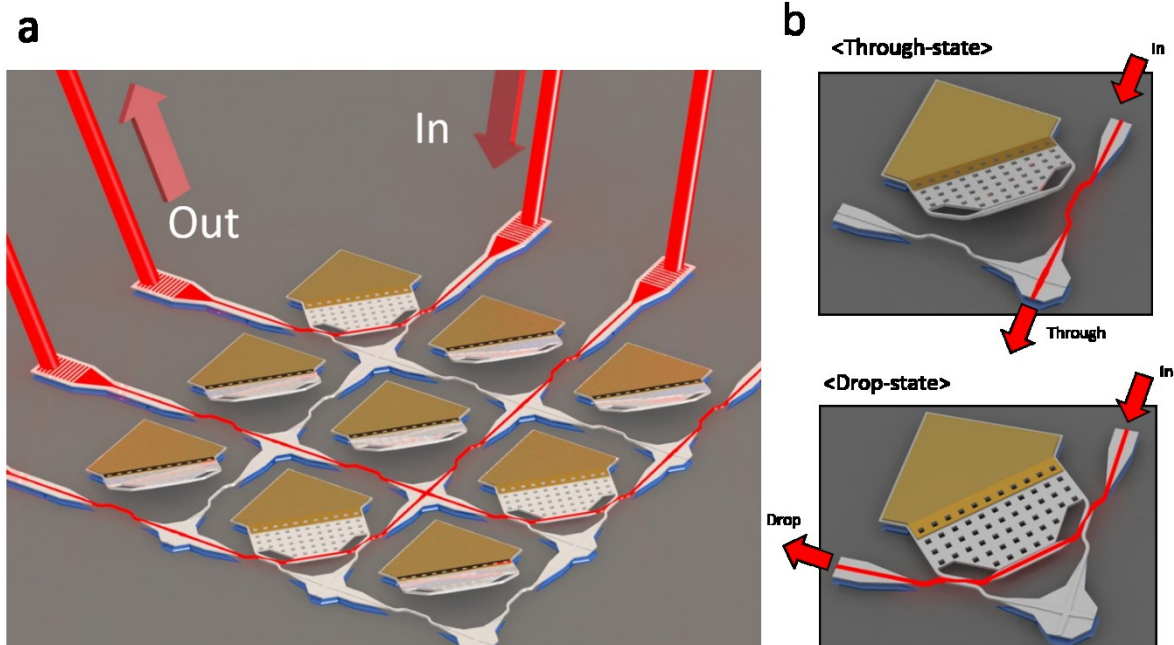
Figure 2.1 (a) Switch architecture overview. (b) Through-state (up), drop-state (down). Modified and reprinted from [63].

Figure 2.2 (a) shows the schematic of a switch cell which consists of two pairs of movable directional couplers, a waveguide crossing, a MEMS cantilever, and a metal pad. One movable directional coupler consists of two waveguides; one of the waveguides is connected to the waveguide crossing that is sitting on top of silicon dioxide layer; the other waveguide is attached to the MEMS cantilever. Figure 2.2 (b) shows the cross-sectional view of the cell. A bias voltage can be applied to the MEMS cantilever through the metal pad, while the silicon substrate is grounded. When bias voltage is not applied, the MEMS cantilever is slightly bent upward by stress of the metal layer. The layer consists of two stacks of metals; chrome at bottom and gold on top. By controlling the thicknesses of the stacks, we can control the amount of stress, and thus the amount of bending of the cantilever. When bias voltage is applied, the MEMS cantilever moves downward in response to electrostatic force exerted from the substrate. The amount of displacement is controlled precisely by the bias voltage. At an optimum bias, light is coupled to the orthogonal waveguide through the two-directional couplers. In the absence of bias, light simply propagates towards the through port without interruption.
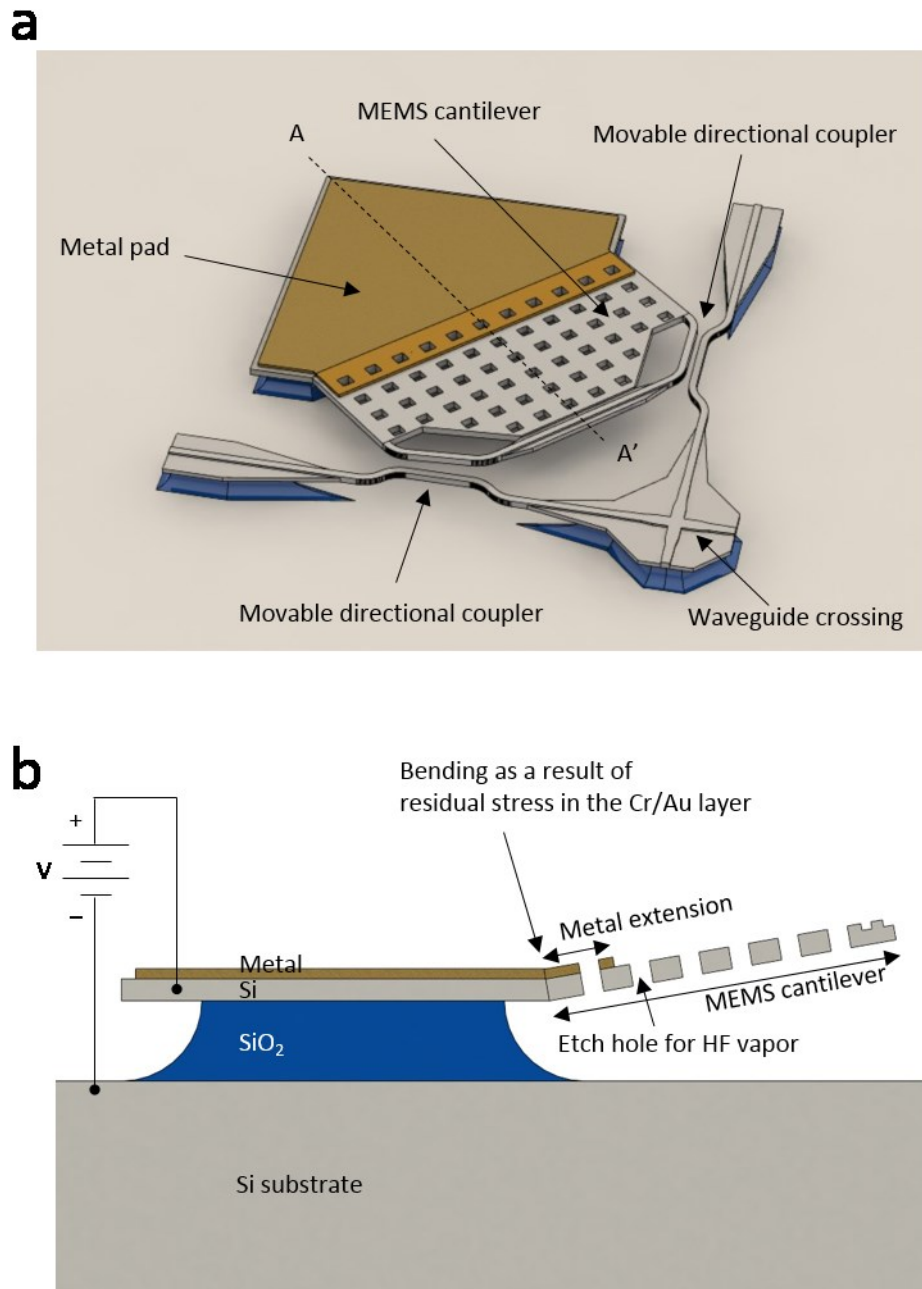
Figure 2.2 (a) Schematic of the switch cell. (b) Cross-sectional view of the switch cell. Figure modified and reprinted from [63].

2.1.1 Vertically moving directional coupler

Optical switching is realized by physically moving one arm of the directional coupler in which there are two symmetric waveguides (Figure 2.3). The coupling is varied by moving one of the waveguides vertically with a MEMS actuator. When the vertical offset is zero, the two waveguides are strongly coupled. The lateral-gap spacing at zero offset is defined lithographically. To achieve a short coupling distance, we designed the gap to be 250 nm which is the resolution limit of our

lithography tool. The thickness of the waveguides (220 nm) is set by the silicon-layer thickness of the SOI wafer. With the gap size and the thickness of the waveguide, we optimized its length and width to achieve 100 % power transfer at 1550 nm wavelength. This is obtained with a waveguide width of 350 nm and a coupling length of 11.9 μm (Figure 2.3(a)). In the off state, the waveguides are separated vertically by 1000 nm, The coupling reduces exponentially and at this spacing, the two waveguides are essentially uncoupled (Figure 2.3 (b)).
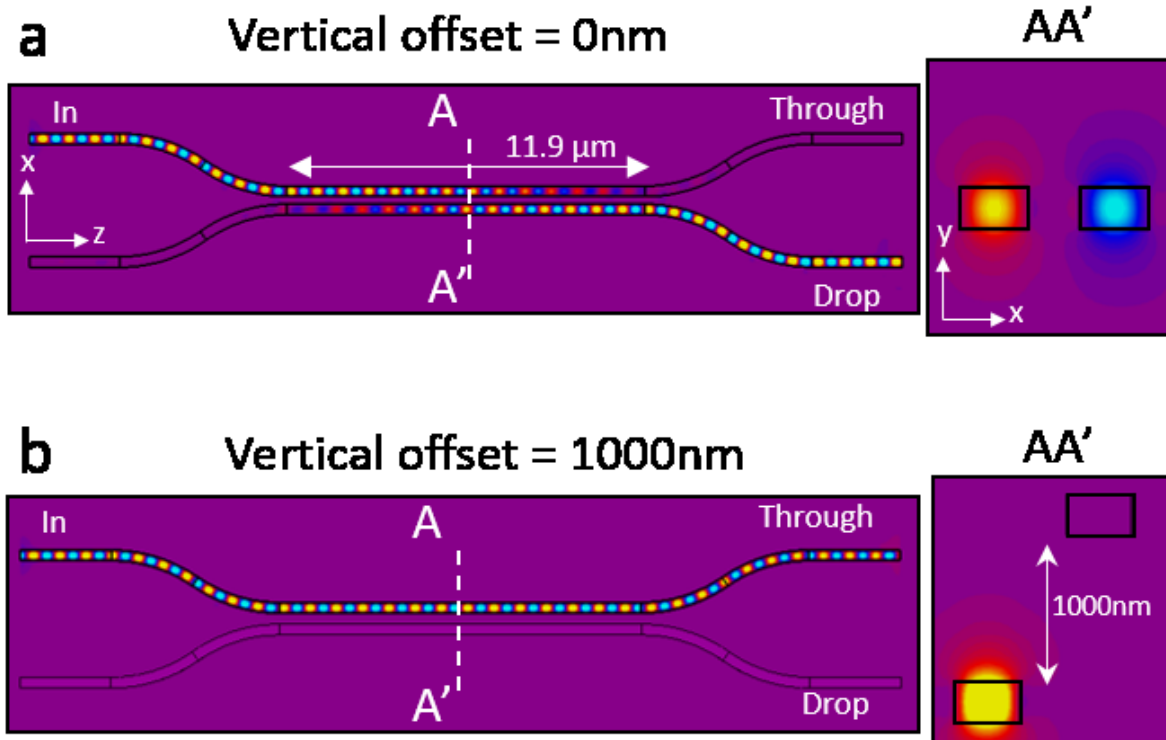
Figure 2.3 Simulated H_y field (y-component of magnetic field) profile of the directional coupler at 1550 nm wavelength. (a) Vertical offset of 0 nm. (b) Vertical offset of 1000 nm. Modified and reprinted from [63].
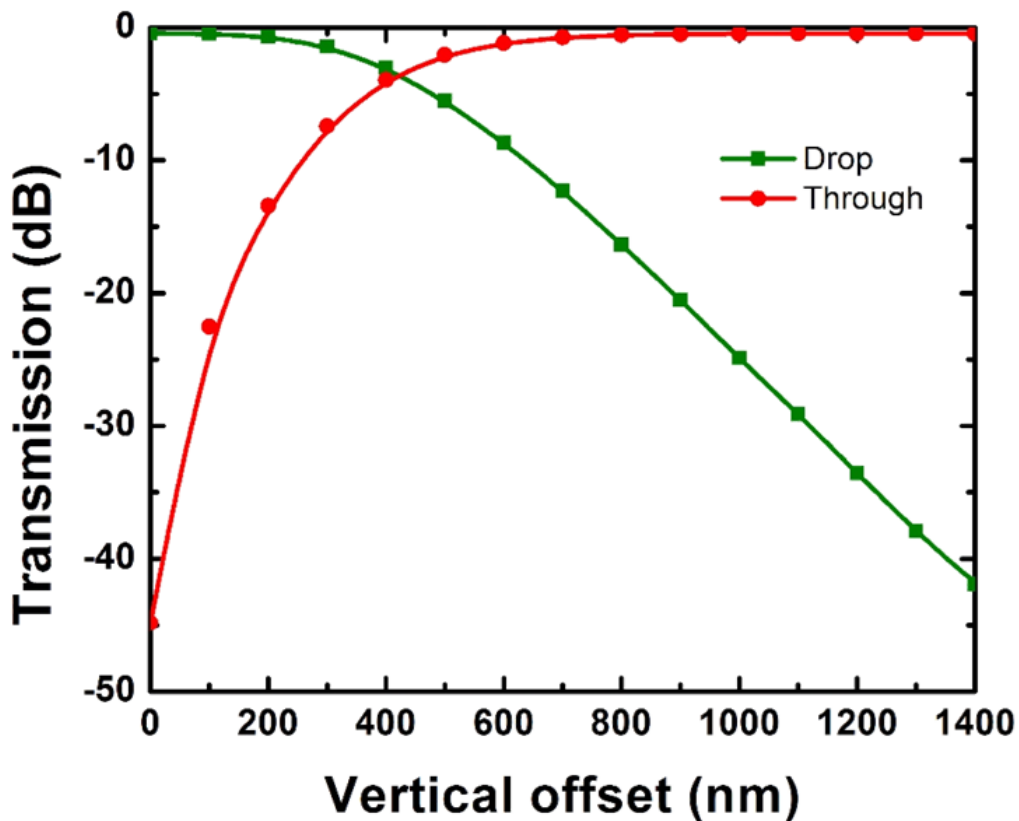
Figure 2.4 Simulated transmission characteristics of vertically moving directional coupler. Modified and reprinted from [63].

Figure 2.4 shows the simulated transmission characteristics of the directional coupler at various vertical offsets. The simulations were done using CST STUDIO SUITE [64]. The configurations of the simulations are same as those shown in Figure 2.3. With a vertical offset of 1000 nm, the optical power at the drop port is less than -20 dB relative to the input power. Thus, we can efficiently switch the directional coupler on and off with a small movement of the movable waveguide.

2.1.2 Ultra-low-loss waveguide crossing

In an NxN optical-crossbar switch, the longest light path has a total of 2N-2 waveguide crossings. The major optical-loss mechanism of a waveguide crossing is light scattering due to the abrupt change in the refractive-index profile at the cross points. In order to minimize the scattering, we used a Multi-Mode-Interference (MMI) [35] design to concentrate light at the centers of the cross points. By having multi-modes in waveguides, we can manipulate the light pattern by controlling interference between different modes. When this is done, the light does not "see" the abrupt

refractive-index change and the scattering loss is markedly reduced. Figure 2.5 (a) shows the simulated optical-mode profile in our ultra-low-loss-waveguide crossing using CST STUDIO SUITE [64]. It consists of a rib waveguide with 70 nm etch depth on 220 nm thick silicon that has been pre-formed as part of the silicon-on-insulator (SOI) wafer used to begin the processing. The 70 nm etch depth is defined on the 220 nm-thick silicon by dry etching. The waveguide is tapered from 1 to 2 μm before the MMI. We ran a parameter sweep of the taper length and the MMI length to minimize the scattering loss. With a taper length of 3.5 μm and an MMI length of 13.5 μm, a very low optical insertion loss of 0.015 dB is obtained (Figure 2.5 (b)). The crosstalk to the orthogonal port is less than -66 dB. In a 50x50 crossbar switch, the longest path has 98 crossings, which corresponds to 1.47 dB of optical insertion loss.
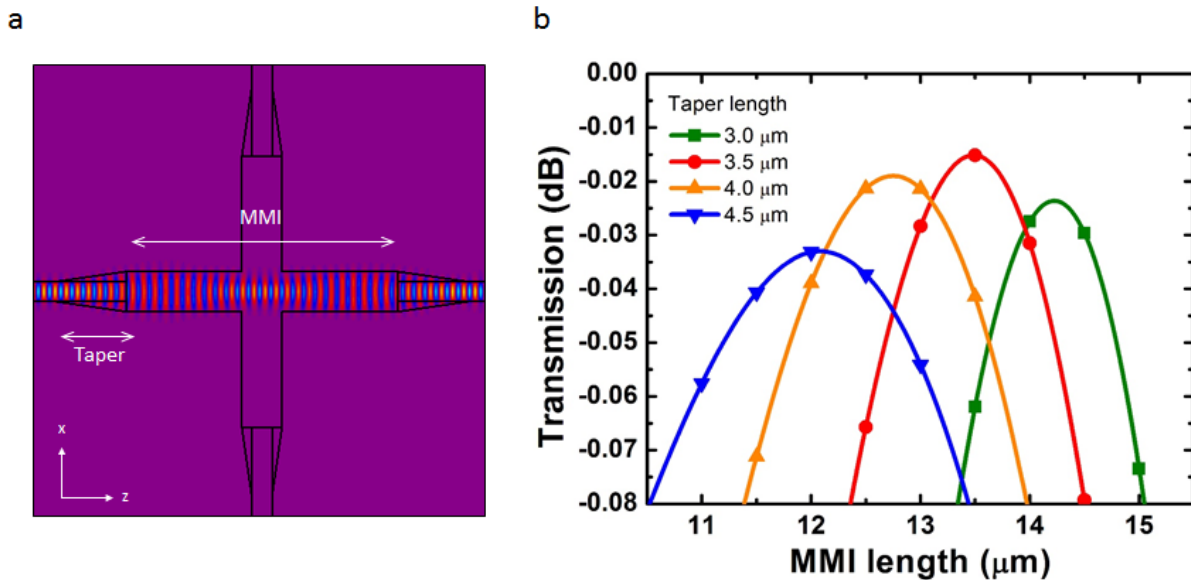
Figure 2.5 Simulation of Ultra-Low-Loss Waveguide crossing. (a) Simulated H_y-field (magnetic field in y-direction) profile with taper length = 3.5 μm, and MMI length = 13.5 μm. (b) Optical insertion loss of various taper lengths and MMI lengths.

2.1.3 Electrostatic MEMS cantilever actuator

Electrostatic MEMS cantilever actuators control the vertical offsets of the directional couplers. Figure 2.2 (b) shows the cross-section of a cantilever actuator. The actuator is capacitive type and thus consumes power only when the cantilever is moving. To produce the initial lift of the cantilever, we coat metal on the hinge of the cantilever. The metal coating consists of 5 nm thick Cr and 30 nm thick Au and extends to the cantilever by 6 μm ("Metal extension" in Figure 2.2 (b)). We coat the metal by using electron-beam evaporation and define it using a photoresist lift-off process. There is tensile stress in the Cr/Au layer, which originates from the electron-beam evaporation method. The tensile stress in the Cr/Au layer bends the cantilever upward in a similar manner as bi-morph [65]. The displacement of the cantilever tip is 1.5 μm at zero bias, which is sufficient to turn off the directional couplers. We modeled the actuator using a simple electrostatic cantilever model. A resonant frequency [66] and a pull-in voltage [67] of a simple electrostatic cantilever can be calculated with the following equations.

14

$$f_{res} = \frac{3.52}{2\pi}\sqrt{\frac{Et^2}{12\rho l^4}}$$

$$V_{pull-in} = \sqrt{\frac{3Et^3 z_0{}^3}{10\varepsilon_0 l^4}}$$

The descriptions and values of the parameters are listed in Table 2-1. Using the equations (2.1) and (2.2) and the values of the parameters, the resonant frequency and the pull-in voltage of the actuator were calculated to be 179 kHz and 24 V, respectively.

Table 2-1: Descriptions of parameters and values for the cantilever actuator.

Parameter	Description	Value
E	Young's modulus of silicon	150 GPa
ρ	Density of silicon	2.32 g·cm^{-3}
ε_0	Permittivity of air	8.85 x 10^{-12} F/m
t	Thickness of the cantilever	220 nm
l	Length of the cantilever	40 µm
z_0	Gap between the cantilever and the substrate	3 µm
t_{Cr}	Thickness of Cr layer	5 nm
t_{Au}	Thickness of Au layer	30 nm

2.2 Fabrication of switch

The 50x50 switch was fabricated in the Marvell Nanofabrication Lab at University of California, Berkeley. We used a 6-inch silicon-on-insulation (SOI) wafer with a 220-nm thick silicon layer and a 3-µm thick buried oxide (BOX) layer. There were three lithography steps with a 248-nm Deep-Ultra-Violet (DUV) stepper. The first two defined the partial- and full-etch areas of the silicon layer. The third step followed by electron-beam evaporation of metals (Cr, Au) and metal-lift-off-processes defines the metal-coated area. Hydrofluoric acid (HF) vapor etching was introduced to release the MEMS actuators and the directional couplers as the last fabrication step. The detailed process flow of the fabrication is shown in Figure 2.6. We started the process by depositing a 100-nm thick low-temperature-oxide (LTO) on a fresh SOI wafer using Low-Pressure-Chemical-Vapor-Deposition (LPCVD). After the deposition, the first lithography step was done to define an etch mask using photoresist. Then the LTO layer was dry-etched with an Inductively-Coupled-Plasma-Etcher until the underlying Si layer was revealed. After the etching, the photoresist was removed with oxygen plasma and the Si layer was dry-etched 70 nm deep having the LTO layer

as a hard mask. The etching was done with a Transformer-Coupled-Plasma-Etcher (TCPE). A second lithography step was done to define a photoresist etch mask for 220-nm-deep-etching of the Si layer. Dry-etching using the TCPE was done after the lithography to etch the Si layer down to the BOX layer. After the dry-etching, the photoresist was removed using an oxygen plasma and the third photo-lithography step was done for a metal lift-off process. Following the lithography step, 5 nm of Cr and 30 nm of Au were deposited on the wafer using an electron-beam evaporator. After the evaporation, a lift-off process was done to define geometries in the metal layer. As a final step, HF vapor etch was used to undercut the BOX layer under the directional couplers and the MEMS actuators. During the vapor etch step, the directional couplers and the MEMS actuators were released in air for actuation (Figure 2.6 (m)). SEM images of the fabricated 50x50 switch is shown in Figure 2.7. The cell size of the switch is 160 x 160 μm^2 and the whole 50x50 switch chip including grating couplers occupies less than 9 x 9 mm^2 of area.
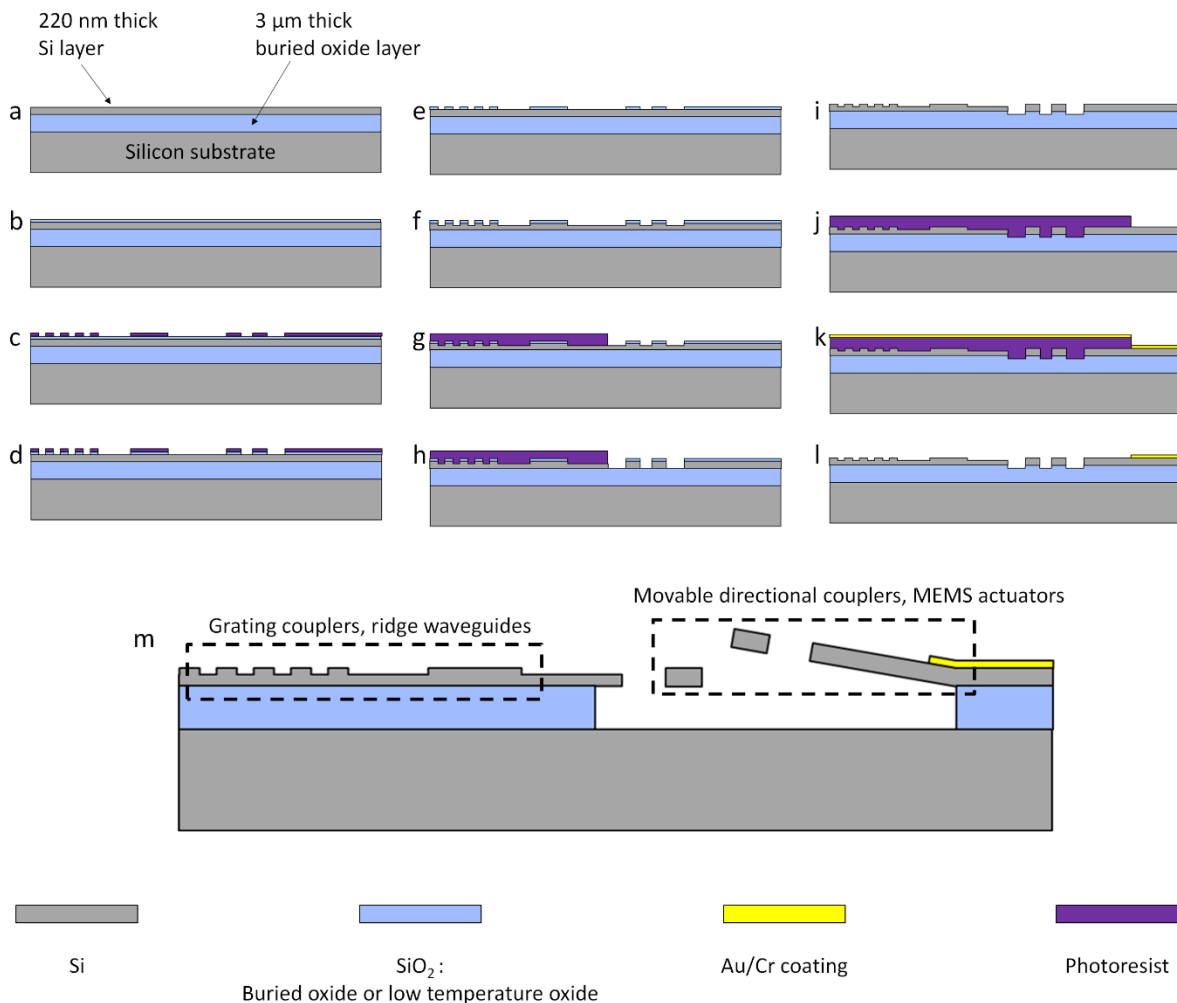
Figure 2.6 Cross-sections indicating process flow of the switch. (a) The process was started from a SOI wafer with 220 nm thick Si layer and, 3 µm thick buried oxide layer. (b) 100 nm thick LTO layer was deposited on the wafer (LTO deposited on the backside of the wafer is not drawn for simplicity.). (c) Photoresist was patterned on top of the LTO layer for an etch mask. (d) The LTO layer was etched until the Si layer was revealed. (e) The photoresist was removed. (f) The Si layer was etched 70 nm deep with LTO layer as etch hard mask. (g) Photoresist was patterned on top of the wafer for an etch mask. (h) The Si layer is

16

fully etched with photoresist and LTO layer as etch masks. (i) Photoresist was removed. (j) Photoresist was patterned on top of the wafer for metal lift-off process. (k) 5 nm thick Cr and 30 nm thick Au was deposited. (l) Metal was lifted-off. (m) The directional couplers and the MEMS actuators were released in air with HF vapor etching.

a

100 μm

b

20 μm

c

2 µm

d

10 µm
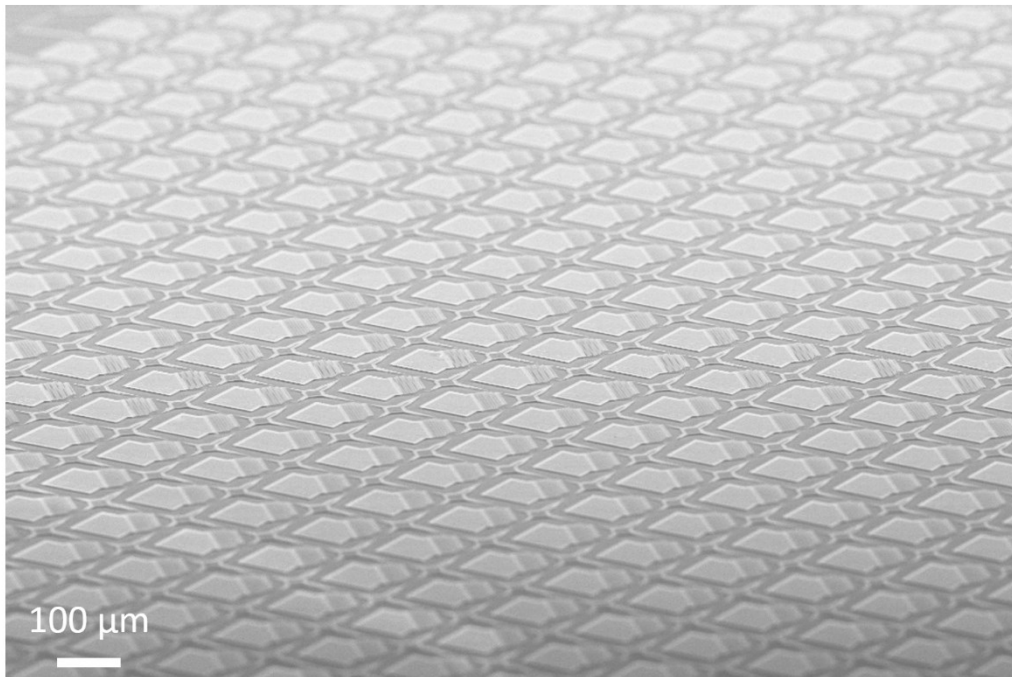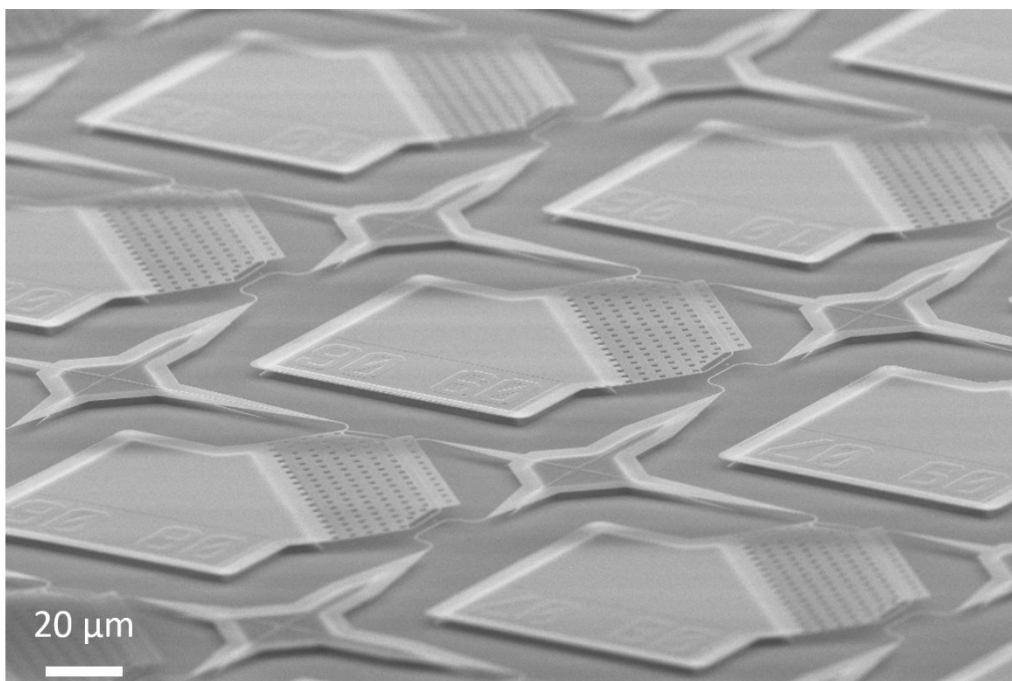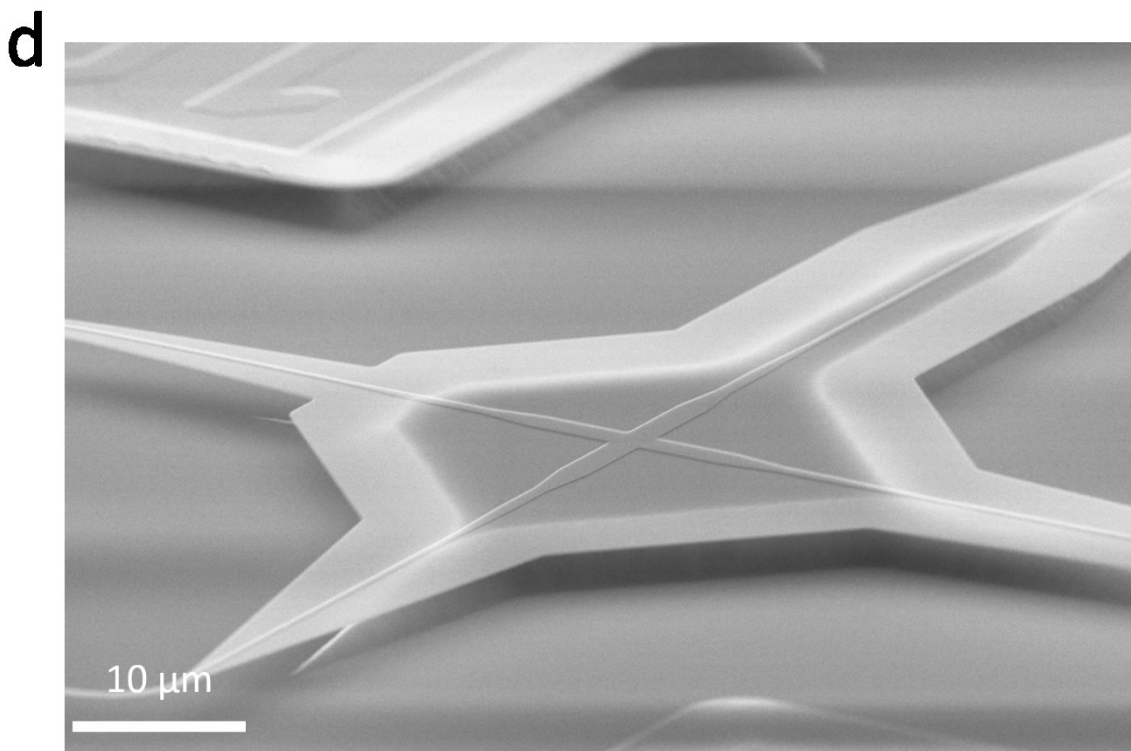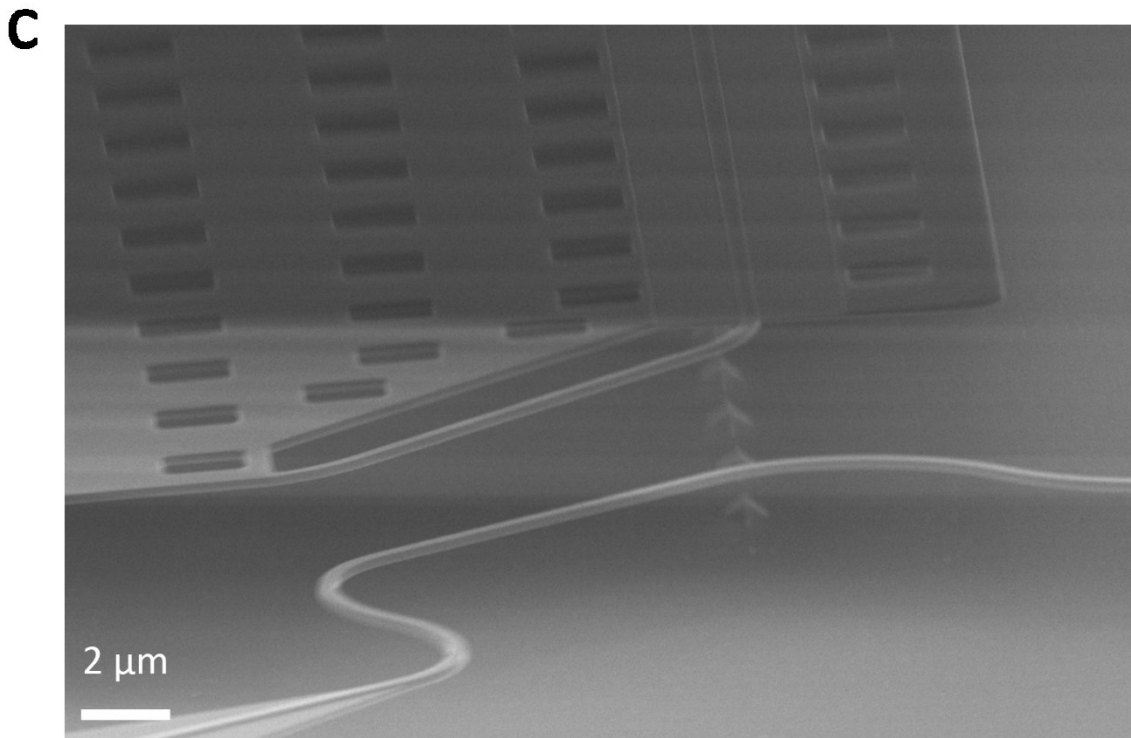
Figure 2.7 SEM images of the fabricated switch. (a) 50x50 switch. (b) Zoomed view. (c) Directional coupler. (d) Waveguide crossing.

2.3 Measured switch characteristics

2.3.1 Measurement method
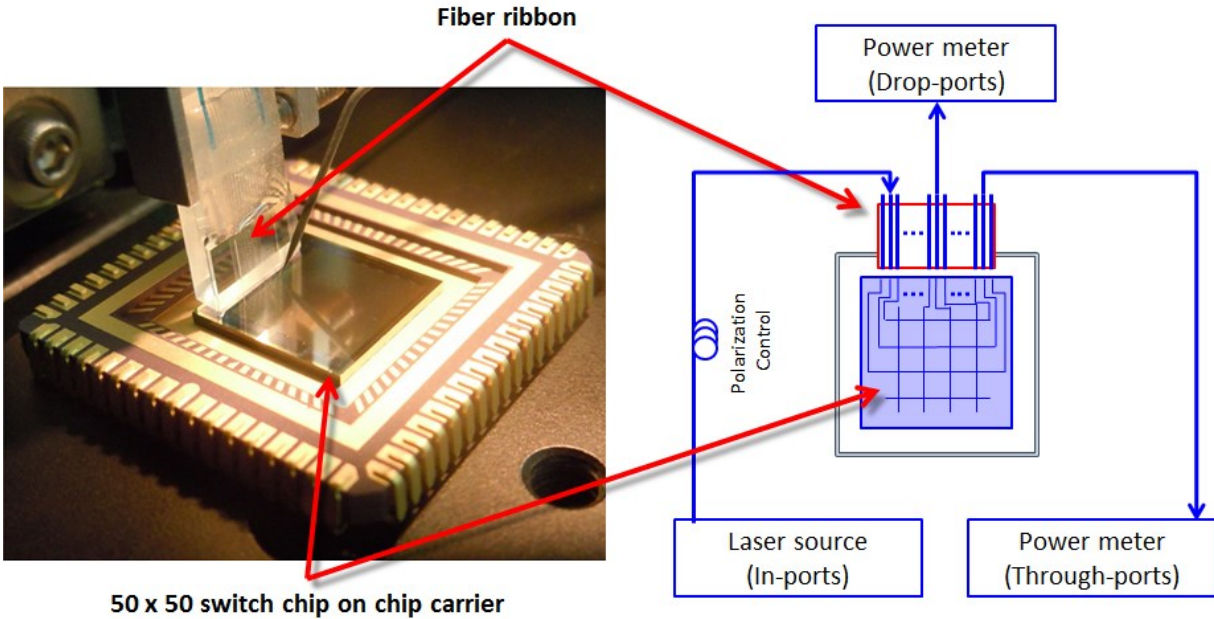
Figure 2.8 A photo (left) and a schematic (right) of the measurement setup. Modified and reprinted from [63].

Figure 2.8 shows the measurement setup we use to characterize the fabricated switch chip. There are two major part in the measurement setup: an optical probing part and an electrical probing part. For optical probing, we use a fiber-ribbon that has equally spaced fibers in a one-dimensional array. There are 24 fibers in the fiber ribbon; they are spaced 127 μm apart, and the polishing angle of the fibers is 13 degrees. The fibers are polarization-maintaining (PM) and single-mode (SM) type. The fiber-ribbon is attached to an alignment stage. These controls allow us to align the fiber ribbon to the chip with precision. The fibers in the ribbon are connected either to a laser source or to an optical power meter to measure optical I/O, and there is a polarization controller connected in front of the laser source to launch TE-mode light to a grating coupler.

The chip is mounted on a chip carrier which functions as a mechanical holder and as a ground plane for the Si-chip substrate. On the chip, there are sets of grating-coupler arrays for coupling between the fibers and the devices. The grating couplers in the array are spaced with a 127 μm pitch in order to match the spacing of the fibers in the fiber ribbon. The relative locations between the fiber ribbon and a selected grating-coupler array can be adjusted using the alignment stage. For coarse alignment, we use an optical microscope to monitor location of the fiber ribbon relative to the grating-couple array. For fine alignment, we utilize an alignment-grating-coupler-pair which consists of two of the grating couplers connected to each other. The pair of grating couplers are located at each end of the array and are connected to each other by

a short waveguide. By sending light to one end of the grating coupler and measuring the optical power coming out of the other end, we can determine how good the alignment is. We optimize the alignment by moving the fiber ribbon and monitoring the optical power coming out. When the output optical power is at maximum, we know that the alignment is optimized and all the grating-couplers laid between the alignment-grating-coupler-pair are aligned to the corresponding fibers in the fiber ribbon.

For electrical probing, we use a tungsten probe tip having a 5 μm tip-radius. The probe tip is mounted on a three-axis probe manipulator. We touch down the probe tip on bias-pads to apply voltage to the actuators in the switch cells.

2.3.2 Voltage transfer curve measurement
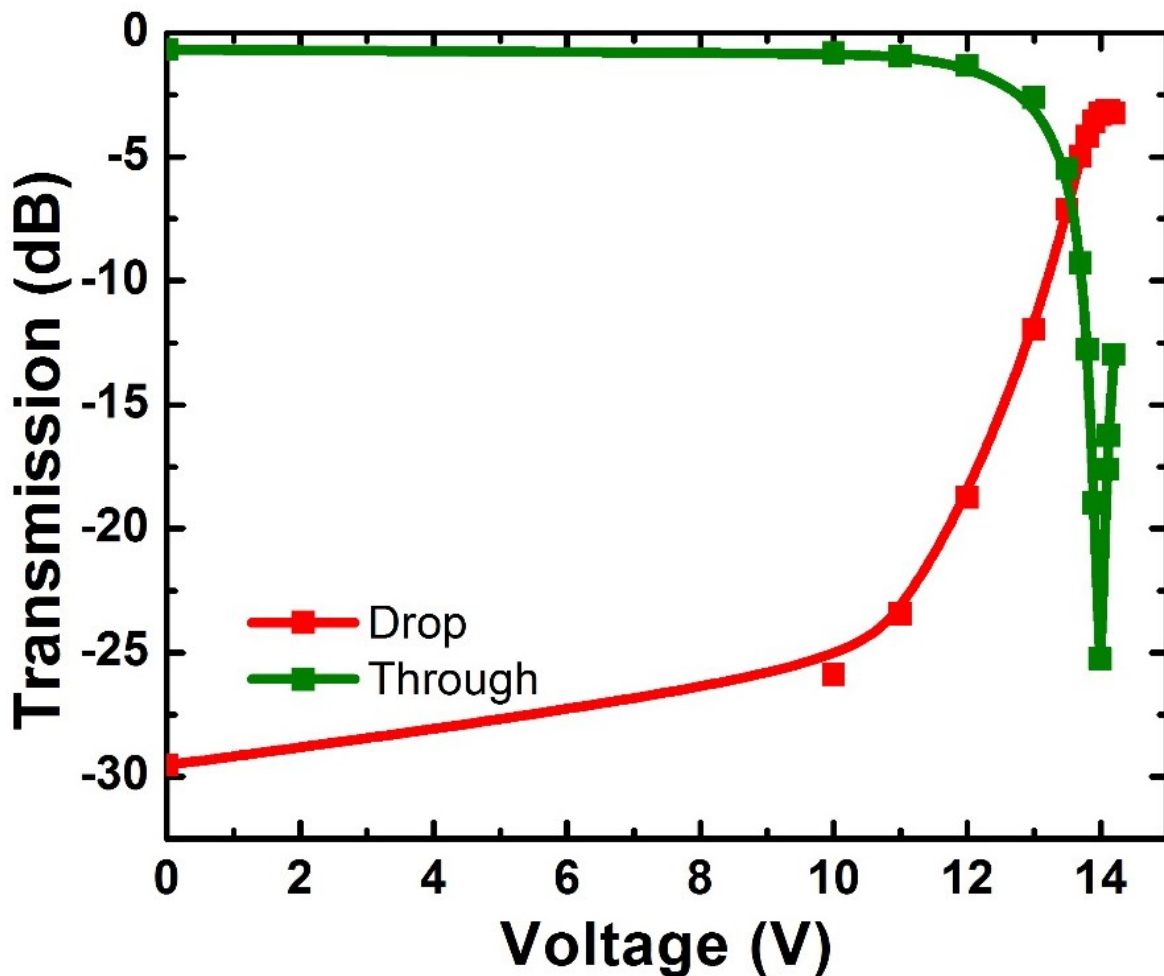
Figure 2.9 Measured transmission characteristics of a switch cell with different bias voltages.

The individual switch cells are tested by applying voltage bias between the substrate and the cantilever actuators. Figure 2.9 shows the measured optical-transmission characteristics of a switch cell with different bias voltages. The moving waveguide of the directional coupler is placed at different vertical locations with different bias voltage. When the moving waveguide is placed parallel to the static waveguide, the optical power transferred to the drop-port is maximized configuring our design for the coupler. This maximum defines an optimal voltage for switching. As shown in Figure 2.9, the optimal voltage is near 14 V. The extinction ratio of the drop port is 26 dB and the extinction ratio of the through port is 25 dB.

2.3.3 Spectral response measurement
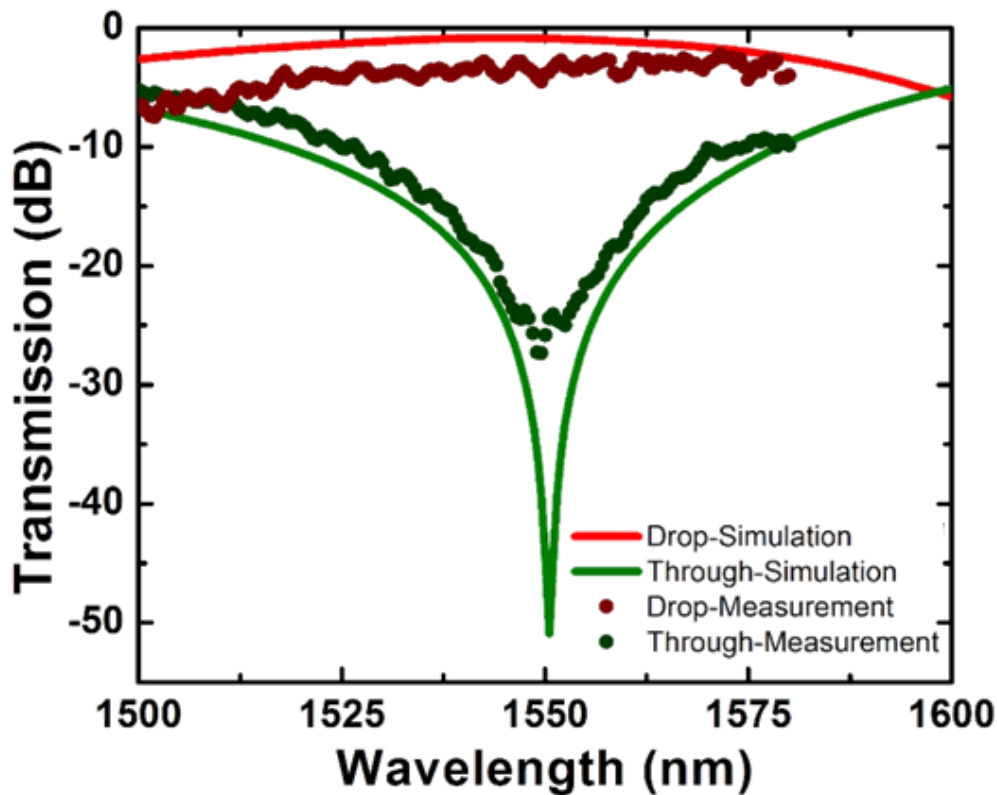
Figure 2.10 Spectral response of a switch cell.

The spectral response of a switch cell at the drop-state is shown in Figure 2.10. The dots represent measurements while the continuous lines represent simulation results. For simulation, we use time-domain analysis with CST STUDIO SUITE [64]. For the measurement, we use a tunable laser source. It is clearly shown from the graph that the maximum extinction ratio is located at 1550 nm wavelength for both the simulation and the measurement results. The extinction ratio at

1550 nm wavelength is measured as 22 dB. The -20 dB bandwidth of the through-port is measured to be 13 nm.

2.3.4 Temporal response measurement
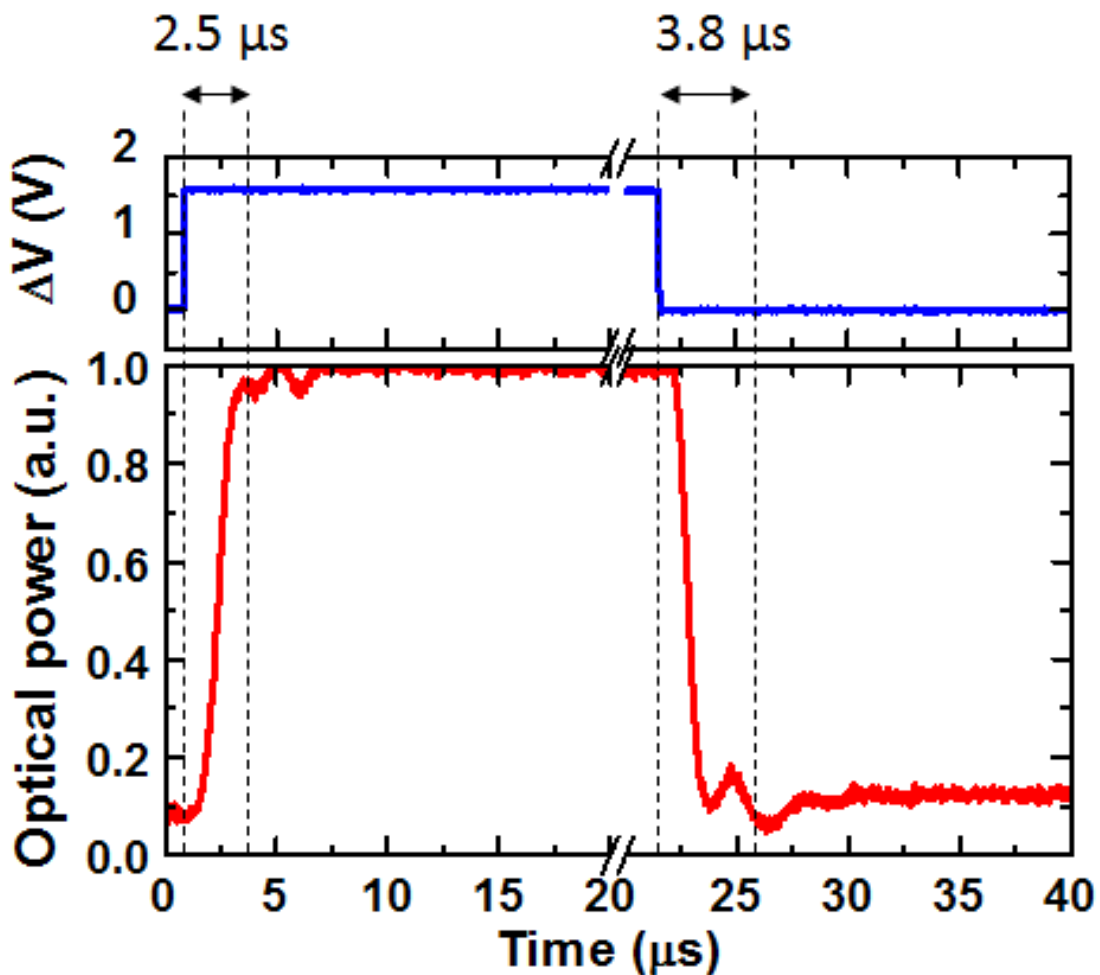
Figure 2.11 Measured temporal response of a switch cell in respect to a square bias voltage. Modified and reprinted from [63].

A measured time response of a switch cell is shown in Figure 2.11. The upper field of the graph represents differential voltages applied to the switch cell while the lower field of the graph represents optical power transmitted to the drop port in response to the voltage applied. A rise time (to 90 % of the maximum power) was measured as 2.5 μs and a fall time (to 10 % of the maximum power) was measured as 3.8 μs. Slight ringings are shown when the switch is turned-on or -off. These ringings can be suppressed by employing more sophisticated voltage waveforms

23

such as two-step voltage waveforms [68]. The response time of the switch can be shortened by utilizing stiffer cantilevers at the expense of needing higher actuation voltages [69,70].

2.3.5 Frequency response of the MEMS cantilever
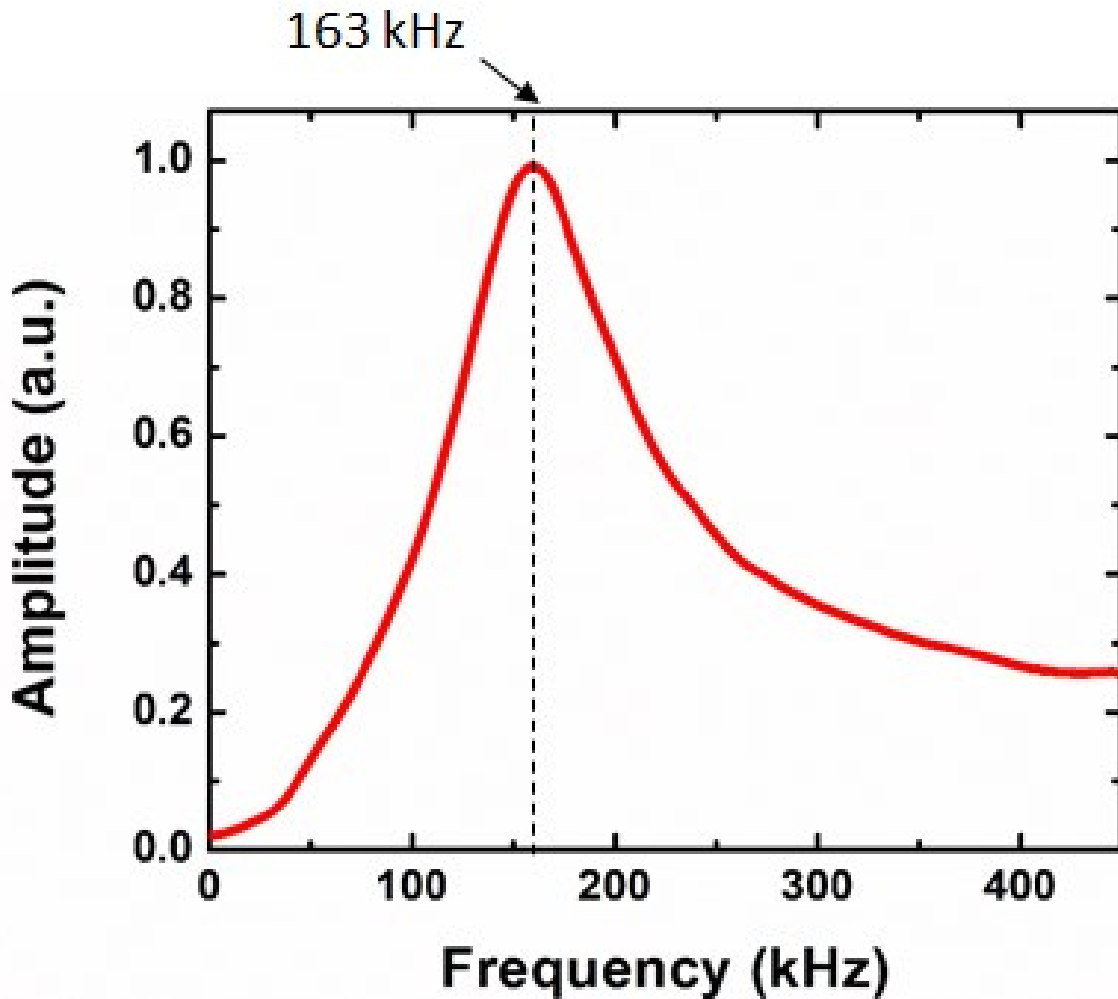
Figure 2.12 Measured frequency response of the MEMS cantilever. Modified and reprinted from [63].

Figure 2.12 shows the frequency response of a MEMS cantilever measured using a Laser Doppler Vibrometer (LDV) [71,72]. The vertical motion of the cantilever was measured while AC voltages having various frequencies were applied to the actuator. The resonance peak was near 163 kHz, agreeing well with the theoretical calculation (179 kHz) using equation (2.1). We calculate a mechanical quality factor of the cantilever by using the following equation.

$$Q = \frac{f_{res}}{\Delta f} \qquad (2.3)$$

24

where f_{res} is the resonant frequency of the cantilever, and Δf is a full-width-at-half-maximum of the amplitude square. From Figure 2.12, we can extract f_{res} as 163 kHz, and Δf as 74.4 kHz. With these values, the quality factor Q is calculated as 2.19.

2.3.6 Insertion loss measurement
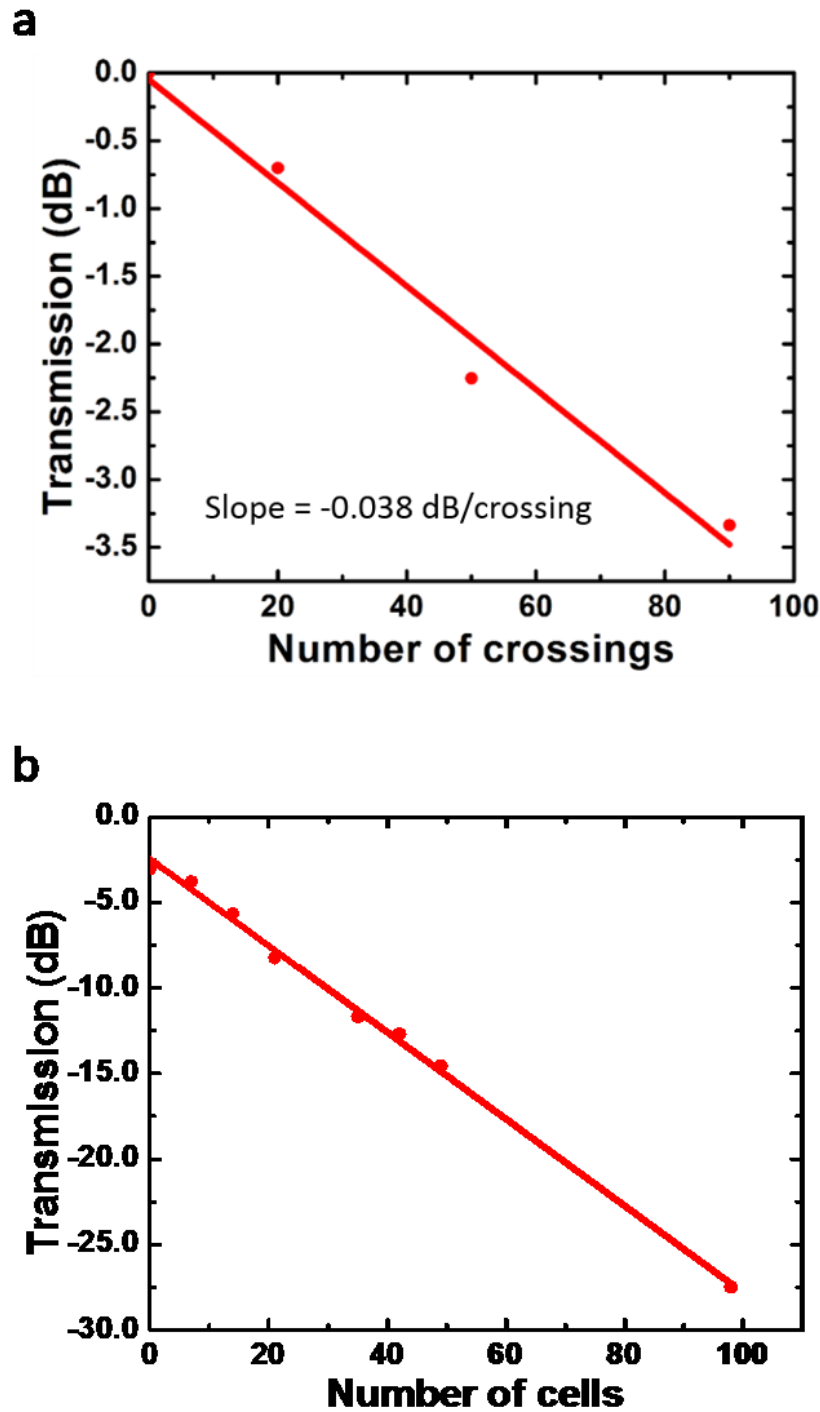
Figure 2.13 Insertion loss measurement of waveguide crossings (a) and 50x50 switch network (b). Modified and reprinted from [63].

We measured losses in test structures having 20,50, and 90 cascaded waveguide crossings to extract the loss of a single waveguide crossing (Figure 2.13 (a)). By linear fit of the data, the loss of a single waveguide crossing was extracted as 0.038 dB. This value is 2.5 times higher than we obtained in simulation (0.015 dB), but still a very small value.

To study the path-dependent loss of the 50x50 switch network, the insertion loss of the optical paths with different path length was measured (Figure 2.13 (b)). The widths of the waveguides in the directional couplers are mostly in the range of 350 to 480 nm due to lithographical variations. The insertion losses of the through-state and the drop-state of a cell were extracted by linear fitting of the measured data points. The slope and the y-intercept of the fitted line represent the through-state loss and the drop-state loss respectively. Therefore, the through-state loss is 0.253 dB and the drop-state loss is 2.47 dB. The optical insertion loss of the longest path was measured as 27.5 dB. The through-state loss is primarily due to the propagation loss of the waveguides. The propagation loss of the waveguides can be suppressed by using a more advanced fabrication process [73–80] or using wider waveguides. The drop-state loss is primarily due to poor coupling in the directional couplers due to the change in its waveguide width.

The maximum insertion loss of the switch is high (27.5 dB). However, the major part of optical loss is coming from waveguide-propagation losses as that are induced from sidewall roughness. We find further evidence for this statement in Chapter 3 where we use wider waveguides and find reduced sidewall-roughness losses. Using 500 nm-wide waveguides, we reduce insertion loss-per-cell (0.087 dB/cell) by nearly a factor of three. This is equivalent to 8.5 dB of loss for a 50x50 switch-array. If we were able to eliminate waveguide propagation losses, the optical insertion loss of the longest path would be reduced to 1.47 dB (0.015 dB x 98) solely due to the waveguide-crossing losses [73].

Chapter 3

Silicon-photonic-switch-array on a waveguide crossbar with laterally moving directional couplers that allow point-to-multipoint connections

Multicast is a form of communication that sends identical information from one source to multiple destinations. Optical multicast [81,82] is desirable for applications that transmitting high-bandwidth signals from one sender to multiple subscribers, such as distributed data-storage-systems [83]. Optical switches that allow point-to-multipoint connections (or multicast optical switches) are needed to operate optical multicast systems. However, at this time typical optical multicast switches use "broadcast-and-select architecture" which sends information, and thus optical power, to all the connected outputs. As a result, there is high optical loss from excessive splitting of the optical power [84].

In this chapter, we introduce a silicon-photonic-switch-array that is capable of multicast operation. This switch-array (which we identify as Generation-B) splits optical power from a source only to the destinations that are subscribing to the source. The architecture of the switch-array is similar to that of Gen-A except that here we use laterally moving directional couplers instead of the vertically cantilevered couplers of Gen-A. Pairs of laterally moving directional couplers are located for switching at each node of the waveguide crossbar allowing incoming signals either to be sent to a drop port or else to continue on the through-waveguide.

In addition, optical loss of the switch is reduced compared to that of the 50x50 switch-array presented in Chapter 2. We use wider waveguides to reduce induced scattering losses due to sidewall roughness. In addition, the laterally moving directional couplers have more precise tuning of coupling, and the switching loss (e.g. drop-state loss) is reduced. As a result, the through-state loss of a switch cell is reduced to 0.087 dB and the drop-state loss of the switch is reduced to 1.376 dB.

To save process cost in the initial testing stage we have implemented a 4x20 switch for a proof-of-concept. This design makes "mask-sharing" with other projects possible. However, the switch can be readily expanded to a port-count of 50x50 or larger by using larger chip area. The 4x20 silicon photonic switch has area of 1.2 x 4.5 mm^2, the longest path on-chip optical insertion of 4.0 dB, and response time of 9.6 μs. We have experimentally demonstrated 1-to-2 and 1-to-4 multicast operation using this Gen-B switch.

3.1 Switch design
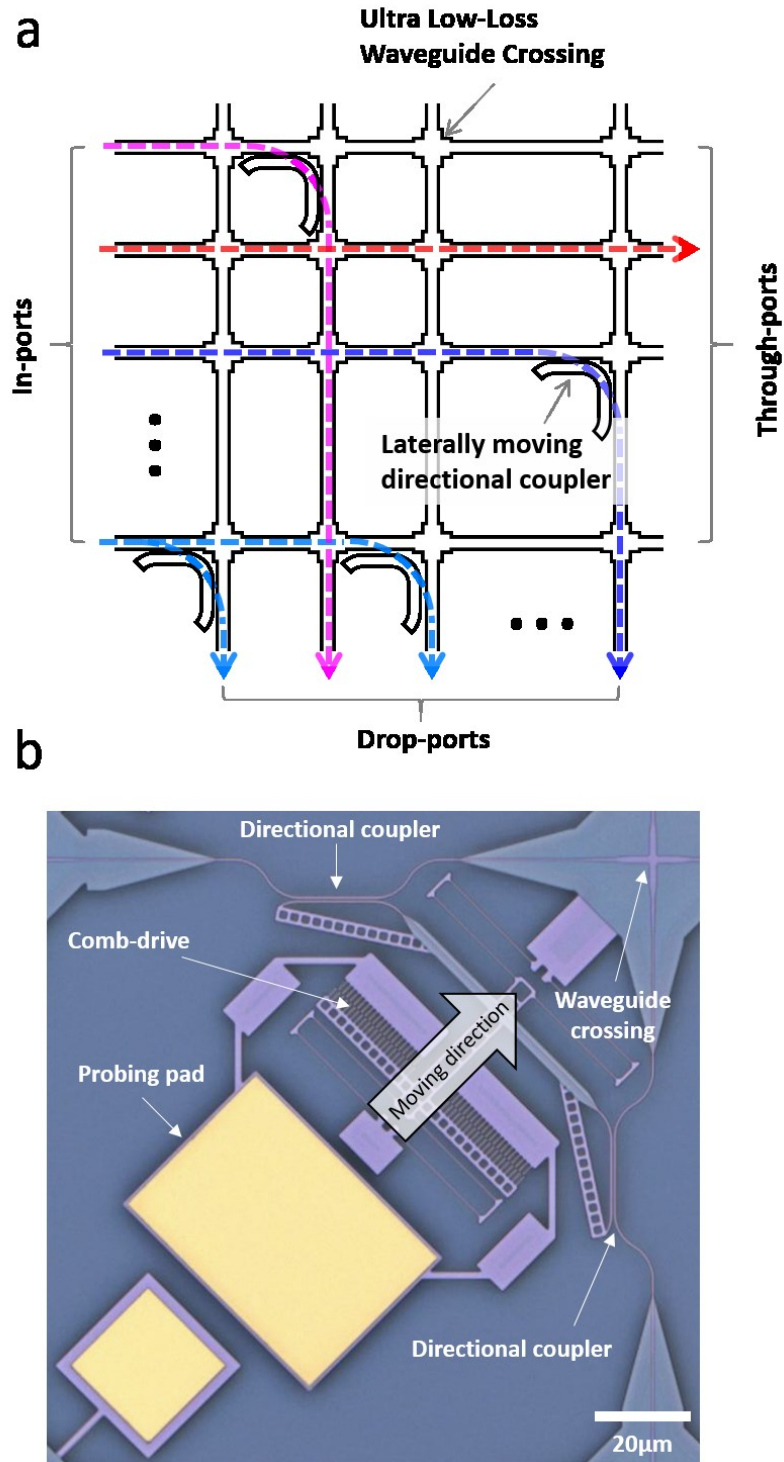
Figure 3.1 (a) Schematic of the multicast switch architecture. (b) Optical image of a switch cell. Modified and reprinted from [85].

Figure 3.1 (a) shows the architecture of the silicon-photonic-switch-array. The architecture has optical crossbar as a light path. For switching operation, the architecture uses *laterally* moving directional couplers. Coupling ratios of the laterally moving directional couplers can be precisely tuned, and optical signal from one source can be divided into multiple destinations by choosing appropriate coupling ratios of the couplers.

Figure 3.1 (b) shows an optical micrograph of a fabricated switch cell. There are two directional couplers and each directional coupler consists of a fixed-waveguide and a movable-waveguide. The movable-waveguide is attached to an electro-static MEMS comb-drive actuator that is capable of moving in diagonal direction. The comb-drive controls the gap of the directional couplers by moving the movable waveguide as similar to [38]. As controlling the gap, the coupling between the fixed- and movable-waveguide changes, and power splitting ratio of the directional coupler changes.

3.1.1 Laterally moving directional coupler

The movable-waveguide and the fixed-waveguide of the laterally moving waveguide are parallel and have symmetric shape. The thickness of the waveguides is 220 nm as determined by the silicon layer thickness on the SOI wafer used for fabrication. We set the width of the waveguides as 500 nm, which is 150 nm wider than that of the 50x50 switch-array in the previous chapter. With the widened waveguide, the optical-field outside of it and thereby the optical-scattering-loss at the waveguide side-wall. However, this change reduces the optical-coupling-strength between the waveguides because there is less optical-field outside. To counteract this fact, we increased the length of the waveguide to 20 μm (from 11.9 μm).

To develop the transfer characteristics of the directional coupler we use the following equations as derived in [35].

$$P_{through} = 1 - sin^2(\kappa L) \tag{3.1}$$

$$P_{drop} = sin^2(\kappa L) \tag{3.2}$$

where $P_{through}$, P_{drop}, κ and L denote optical power transferred to the through port, optical power transferred to the drop-port, coupling coefficient of the directional coupler, and length of the directional coupler, (=20 μm) respectively.

The coupling coefficient of the directional coupler is calculated using the following equation.

$$\kappa = \frac{\beta_{even} - \beta_{odd}}{2} \tag{3.3}$$

where β_{even} and β_{odd} denote the propagation constants of even- and odd-modes of the directional coupler, respectively. We calculated β_{even} and β_{odd} using CST STUDIO SUITE [64] with different gap

size g, and calculated κ. The calculated value is plotted in Figure 3.2. Since coupling coefficient is proportional to exponential of coupling gap size [35], we can obtain the following relationship by fitting the calculated points with exponential function.

$$\kappa = 175289 \left[\frac{1}{m}\right] * e^{-0.01219 \left[\frac{1}{nm}\right] g} \qquad (3.4)$$

where g is the coupling gap size.
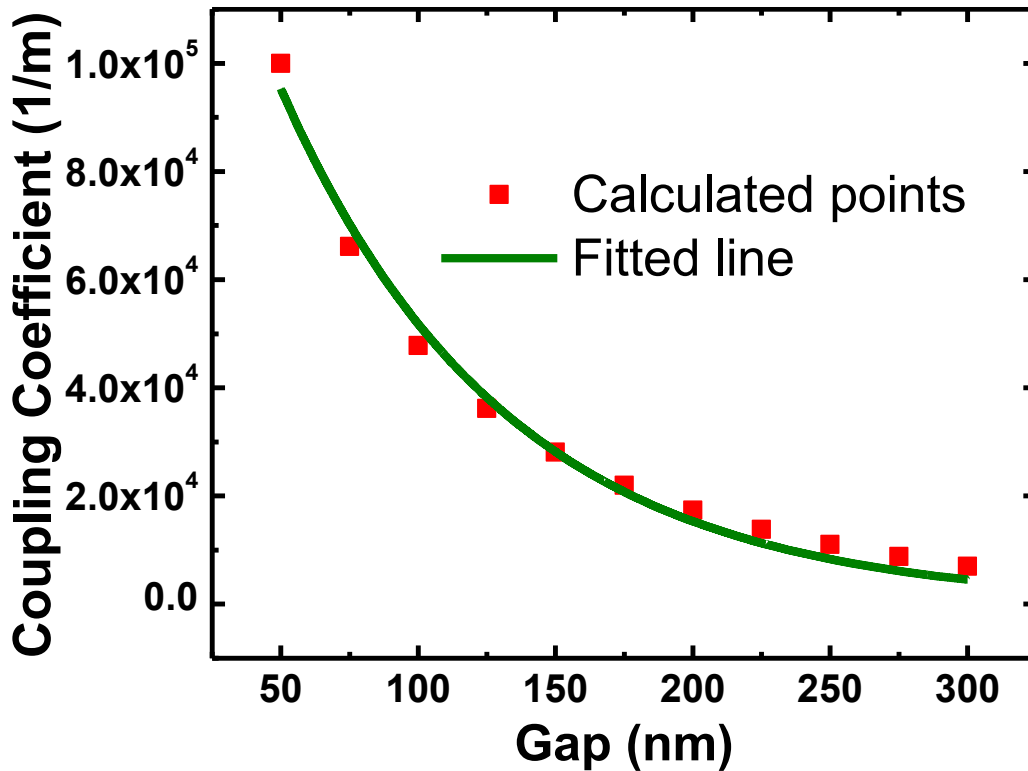
Figure 3.2 Calculated coupling coefficient (red dots) and a curve fitted with equation (3.4) (red line).

By combining (3.1)and (3.2) with (3.4), we calculate the transmission characteristic of the directional coupler as a function of gap size, and it is plotted in Figure 3.3. Optical power transferred to drop-port is maximum when the gap size is near 60 nm. With the gap size below 60 nm, the part of optical power transferred to the drop-port couples back to the through-port due to over-coupling. Figure 3.4 shows the mode-profile obtained by using a full 3D-time-domain simulation [64] of the directional coupler. The simulation result shows that optical power transfers to drop-port completely when the gap is 95 nm (Figure 3.4 (a)). On the other hand, with a 500 nm gap-size, all of the optical power transfers to the through-port (Figure 3.4 (b)).
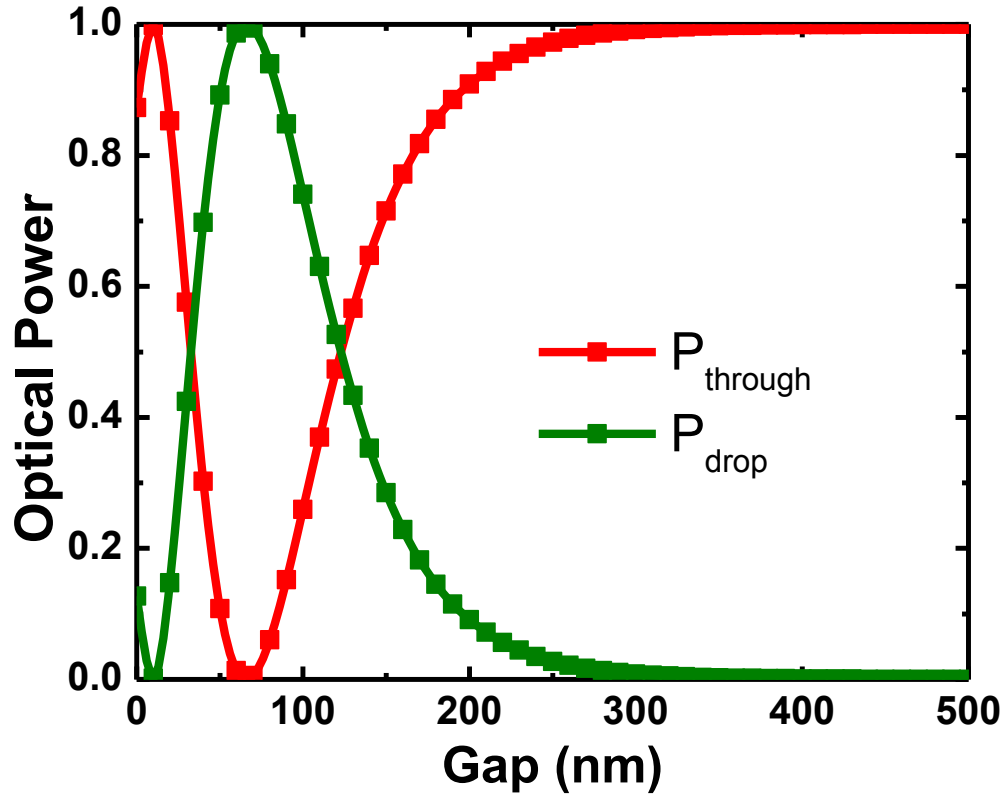
Figure 3.3 Optical power transmission with various gaps.
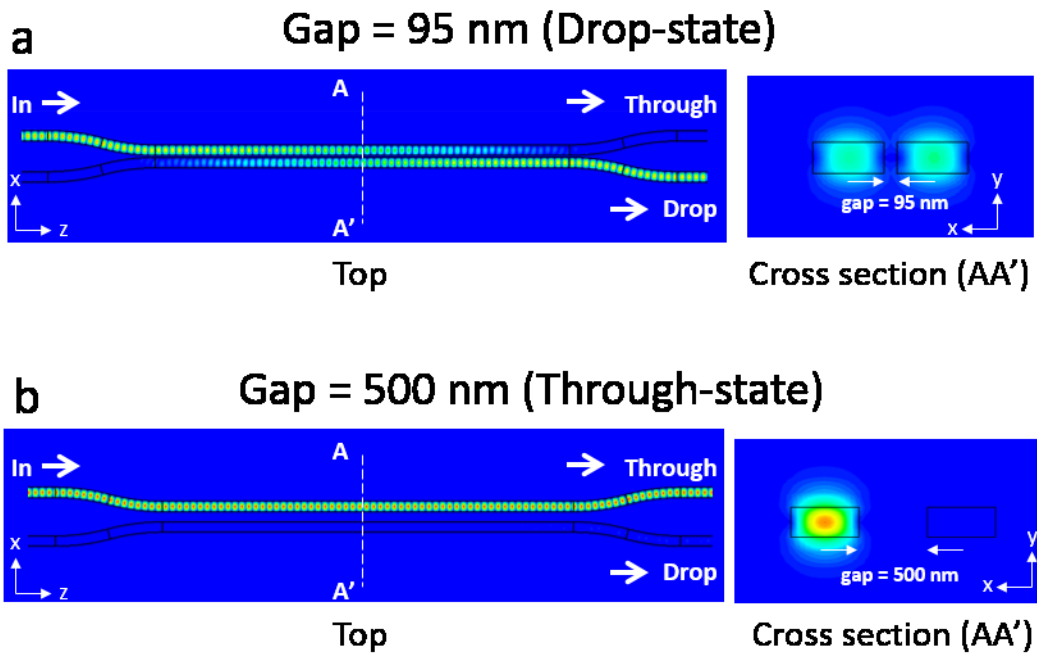
Figure 3.4 H_y-field (magnetic field in y-direction) profile of directional couplers with gap = 95 nm (a) and gap = 500 nm (b).

3.1.2 Comb-drive actuator design
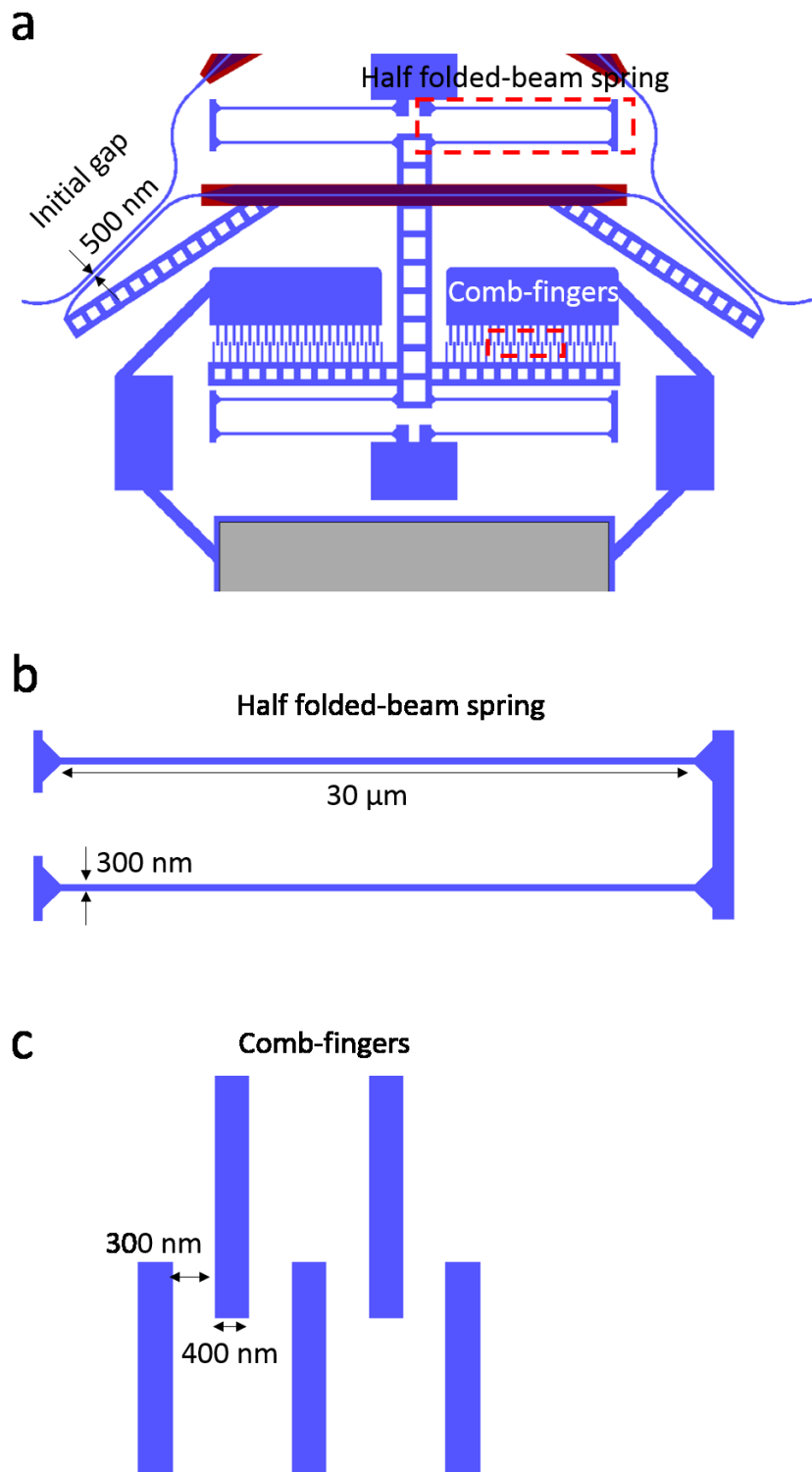
Figure 3.5 (a) Switch unitcell layout. (b) Layout of half-folded spring. (c) Layout of comb-drive.

Figure 3.5 shows the layout of a switch cell. The initial gap of the directional c   oupler is 500 nm when no bias voltage is applied. There are four-half-folded-beam springs holding a comb-drive shuttle. The spring is 220 nm thick, 300 nm wide, and 30 μm long (Figure 3.5 (b)). There are total 44 pairs of comb-fingers. The widths of the comb-fingers and the spacings between them are 300 nm and 400 nm respectively (Figure 3.5 (c)). The moving mass of the actuator is 0.49 ng as estimated from its area (957 μm^2) and thickness (220 nm).

The spring constant of the half-folded-beam spring is 0.0165 N/m as calculated using the equation(3.5) [86].

$$k_{sp} = \frac{Etw^3}{2l^3}$$

(3.5)

where E = 150 GPa (Young's modulus of Si), t = 220 nm (the thickness of the spring), w = 300 nm (the width of the spring), and l = 30 μm (the length of the spring).

Since there are four of the half-folded-beam springs in the actuator, the total spring constant of the actuator is 0.066 N/m (4 x 0.0165 N/m).

The resonant frequency of the actuator is calculated to be 58.4 kHz using the equation (3.6) [87].

$$f_{res} = \frac{1}{2\pi}\sqrt{\frac{k_{total}}{m}}$$

(3.6)

and taking k_{total} = 0.066 N/m and m = 0.49 ng.

The relationship between displacement (d) and applied voltage (V) based on equating the electrostatic force of the comb-drive and the restoring force of the springs, is expressed in (3.7) [88].

$$d = \frac{\varepsilon_0 nt}{k_{total}g_{comb}}V^2$$

(3.7)

or

$$V = \sqrt{\frac{k_{total}g_{comb}}{\varepsilon_0 nt}d}$$

(3.8)

where ε_0 = 8.85 x 10^{-12} F/m (Permittivity of air), n = 44 (number of comb-finger pairs), t = 220 nm (thickness of a comb-finger), k_{total} = 0.066 N/m (total spring constant), g_{comb} = 400 nm (gap between the comb-fingers). V and d denote voltage and displacement, respectively.

Based on (3.8), the voltage versus displacement relationship is calculated and plotted on Figure 3.6. Since the coupler-waveguides move in a direction that is 45° from the actuator motion, the coupler-waveguides move $1/\sqrt{2}$ times the actuator motion. To bring the switch to a drop-state, we need to move the coupler-waveguides by 405 nm (difference between gap = 500 nm and gap = 95 nm). Thus the actuator needs to move by 573 nm (=$\sqrt{2}$ x 405 nm) to bring the coupler-waveguides to the on-state. This requires around 13 V according to Figure 3.6.
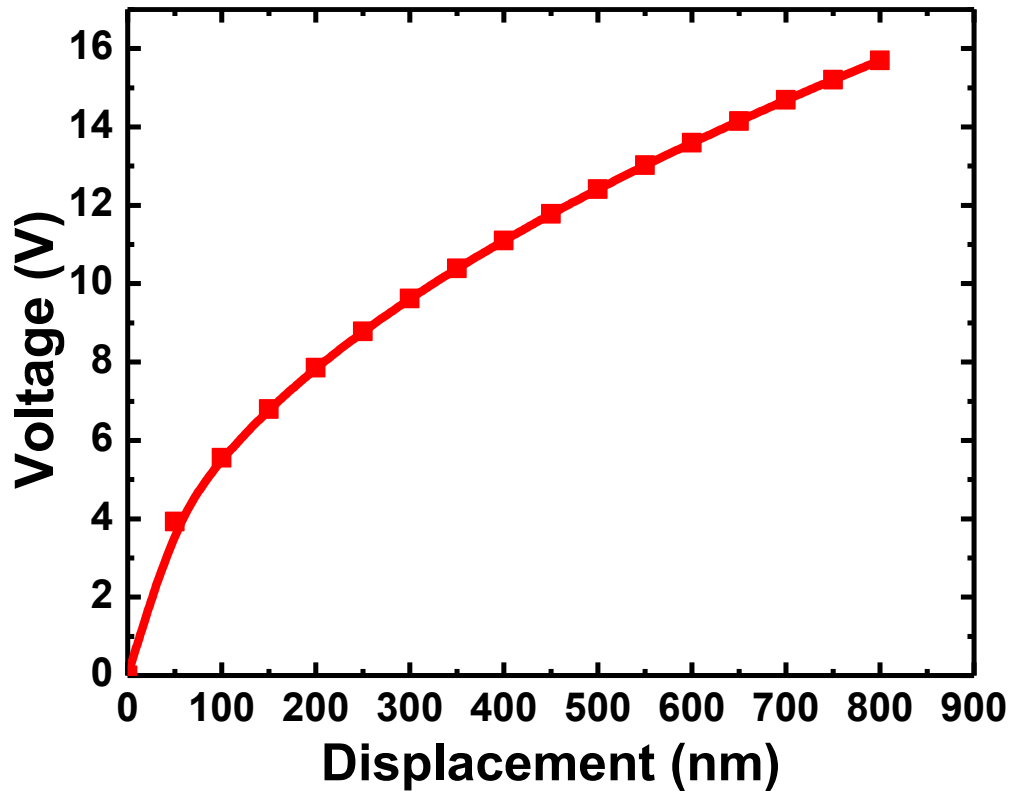
Figure 3.6 Simulated voltage *vs* displacement relationship of the actuator.

3.2 Fabrication of switch

The fabrication process for the laterally moving optical switch is similar to that shown in Chapter 2.2, except that a photoresist reflow process was used [89] in place of an LTO hard mask. This modification reduces the sidewall roughness of the Si waveguides and thus reduces their optical-scattering-losses. The fabrication process was done in the Marvell Nanofabrication Lab at the University of California, Berkeley.

Figure 3.7 shows cross sections of the steps in fabrication process. We started with 6'' Silicon-On-Insulator (SOI) wafers having 220 nm-thick Si layers, and 3 µm thick buried-oxide (BOX) layers. There were a total of three lithography steps made using a 248 nm DUV stepper. The first lithography step was done on the wafer to define an etch mask to define 70 nm-deep Si etching. After the first lithography step, the photoresist was reflowed at 158 $^{\circ}$C for 1 minute to reduce its roughness [89]. Then the Si layer is dry-etched 70 nm deep using a TCP etcher. After the etching, the photoresist is removed using an oxygen plasma. The second lithography step is to define an etch mask for 220 nm-deep Si etching. Again, the photoresist was reflowed at 158 $^{\circ}$C for 1 minute after the lithography step. The second Si etching step followed etching the Si layer 220 nm deep. The photoresist was removed again using an oxygen plasma. The third lithography step was done for a metal lift-off process to define metal probing pads. After the third lithography step, 50 nm of Cr and 100 nm of Au were evaporated on the wafer using an electron-beam evaporation tool. Then the evaporated metal is lifted-off using Acetone. Finally, an HF vapor-etching process was done to release the directional couplers and the MEMS actuators.

Figure 3.8 shows an optical micrograph of the fabricated 4x20 switch. The cell size of the switch is 170x170 µm^2 and the size of the entire switch chip including grating couplers is 1.2x4.5 mm^2.

220 nm thick Si layer

3 µm thick buried-oxide (BOX) layer

a

b

c

d

e

f

g

h

i

j

k

Grating couplers, ridge waveguides

Movable directional couplers, MEMS actuators

Si

SiO$_2$ (BOX)

Au/Cr coating

Photoresist
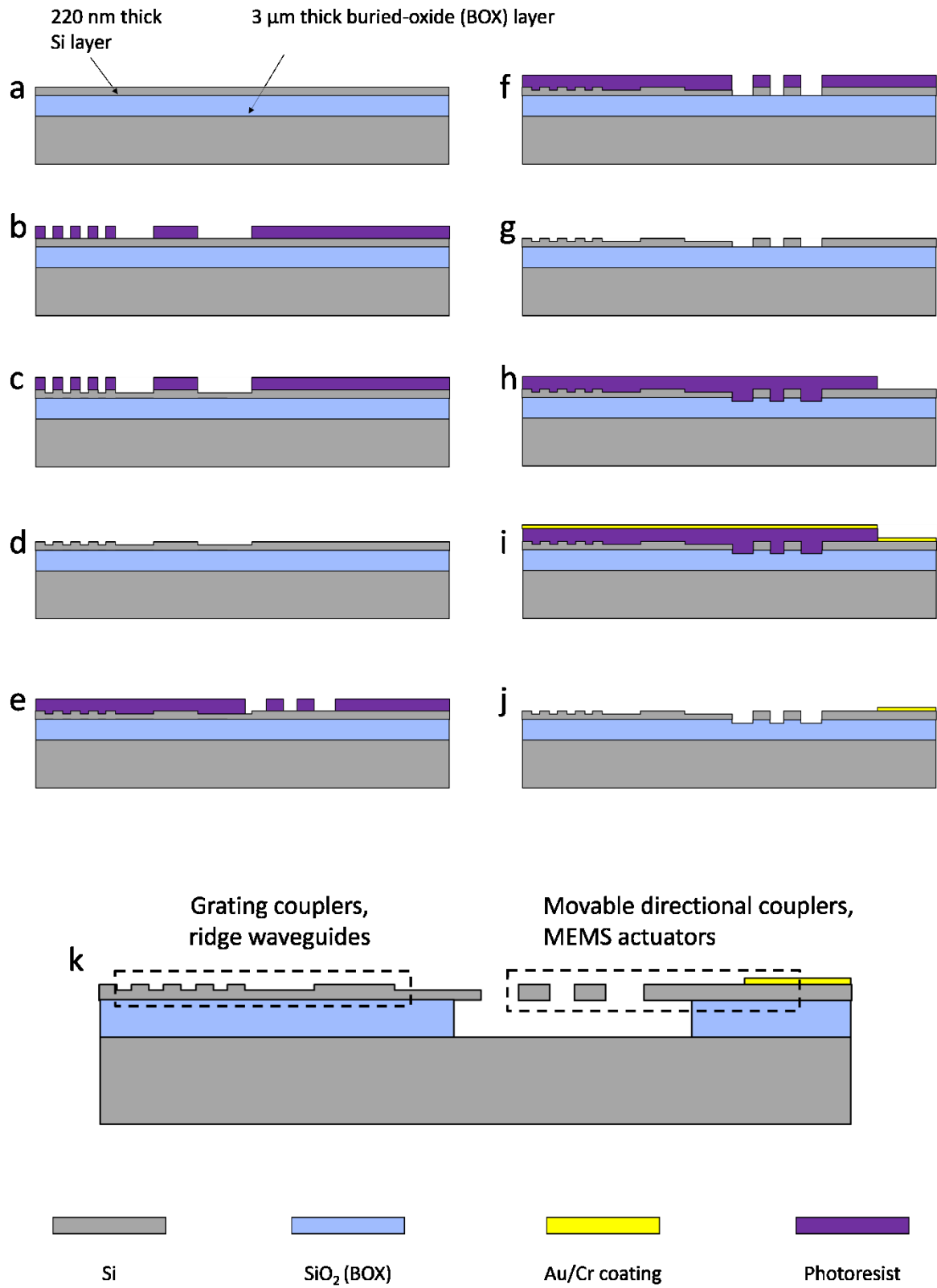
Figure 3.7 Cross section showing process flow for the switch
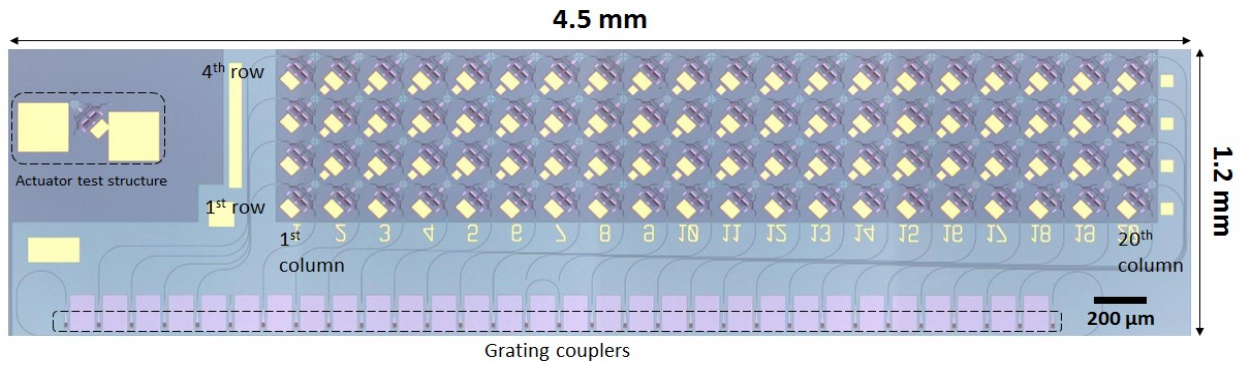
Figure 3.8 Optical micrograph of fabricated 4x20 switch. Modified and reprinted from [85].

3.3 Measured switch characteristics

In the 4x20 switch layout, all the columns and the rows are connected to grating couplers except for columns 9 and 10 due to a mistake in the switch layout. There are variations of initial gap sizes built in to the directional couplers. The initial gap size is 1000 nm in the 1st, 2nd, and 3rd rows, and 500 nm in the 4th row (Figure 3.8). Unfortunately, the travel-range of the comb-drive actuator was not sufficient to close the gap size of 1000 nm due to lateral stiction [88] of comb-fingers. Therefore, for measurement, we narrowed down our scope to the 4th row.

3.3.1 Voltage transfer curve
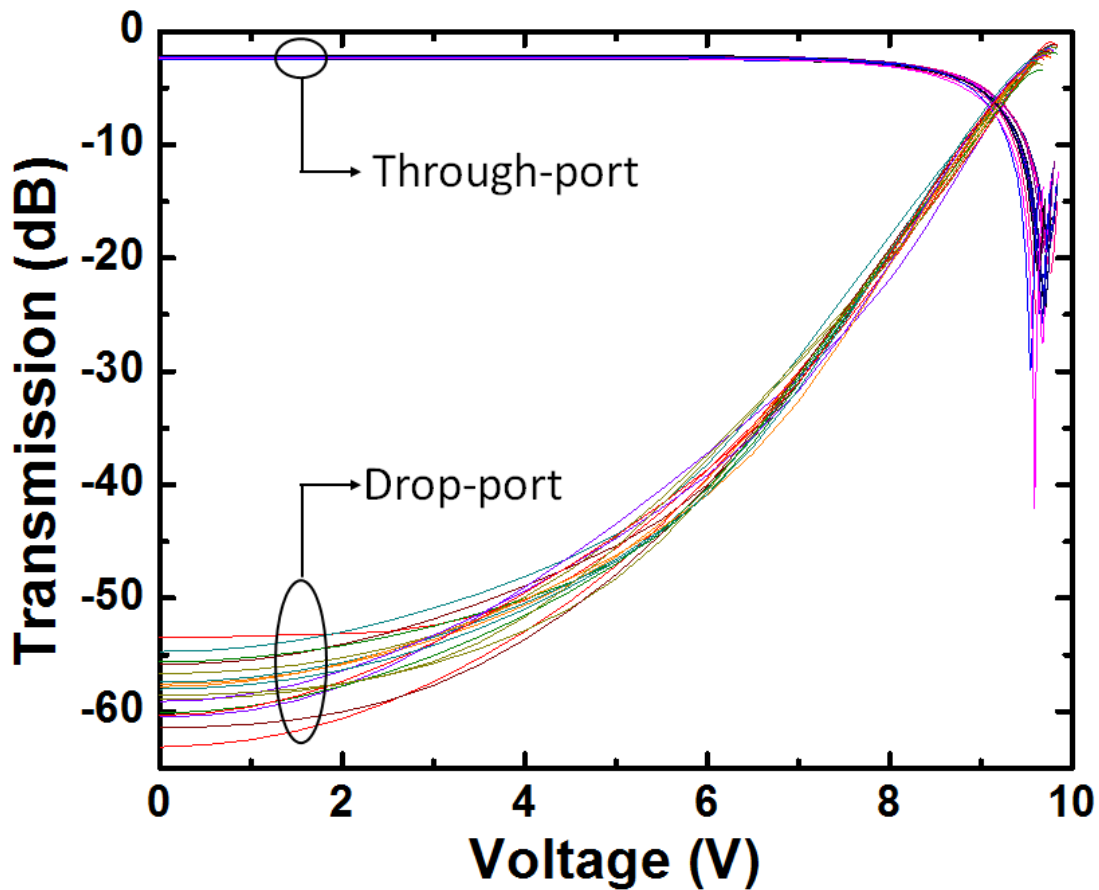
Figure 3.9 Measured transmission characteristics as a function of bias voltage. Modified and reprinted from [85].

We measured transmission characteristics of switch cells in the 4th row of the switch using 1550 nm-wavelength. As mentioned above, two of the columns (9 and 10) were not connected to grating couplers, so there are a total of 18 measurable cells in the 4th row. 17 out of the 18 measurable cells were fully functional and their responses to bias voltages are plotted in Figure 3.9 (One non-fully functional cell may have been damaged when handling the chip). As shown in the plot, optical power transmitted to the drop-port is maximum near 9.7 V. At 0 V, the optical

39

powers transmitted to the drop-port are all less than -50 dB with respect to the input power. The on-off extinction ratio is 56.26 dB for drop-ports and 21.46 dB for through-ports on average.

3.3.2 Spectral response
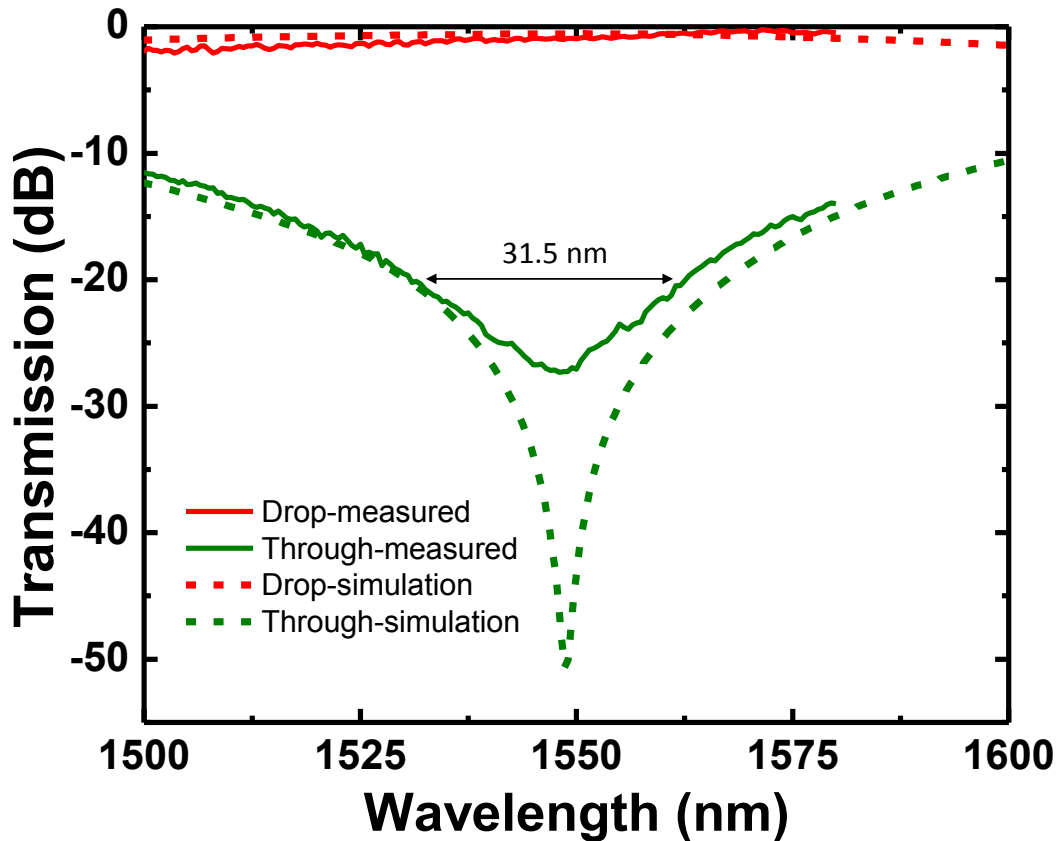
Figure 3.10 Spectral response of switch cell at drop-state. Modified and reprinted from [85].

Figure 3.10 shows the spectral response of a switch cell at drop-state. Both the simulated and measured results show the maximum extinction ratio (between the drop-port and the through-port) near 1550 nm. The 20 dB bandwidth of the through-port is measured to be 31.5 nm.

3.3.3 Temporal response
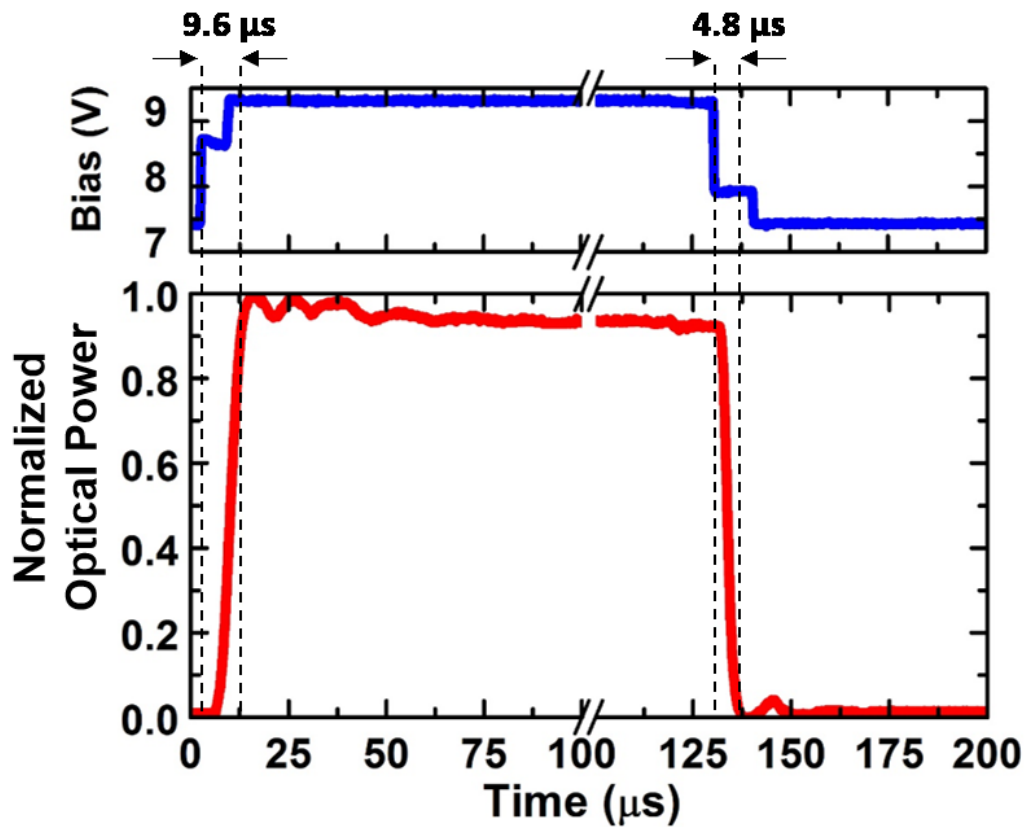
Figure 3.11 Optical power in a drop-port in response to an applied voltage. Modified and reprinted from [85].

Figure 3.11 shows the measured time response of a switch cell. The optical power was measured at the drop-port. In order to suppress ringing of the actuator, a feedforward control signal with two voltage steps was applied (Figure 3.11 top) [68]. The rise time (to 90 % of the maximum power) and the fall time (to 10 % of the maximum power) were measured as 9.6 μs and 4.8 μs respectively. Response time of the actuator can be reduced by simply reducing the length of the springs in the actuator, at the expense of needing higher switching voltage values.

3.3.4 Insertion loss measurement
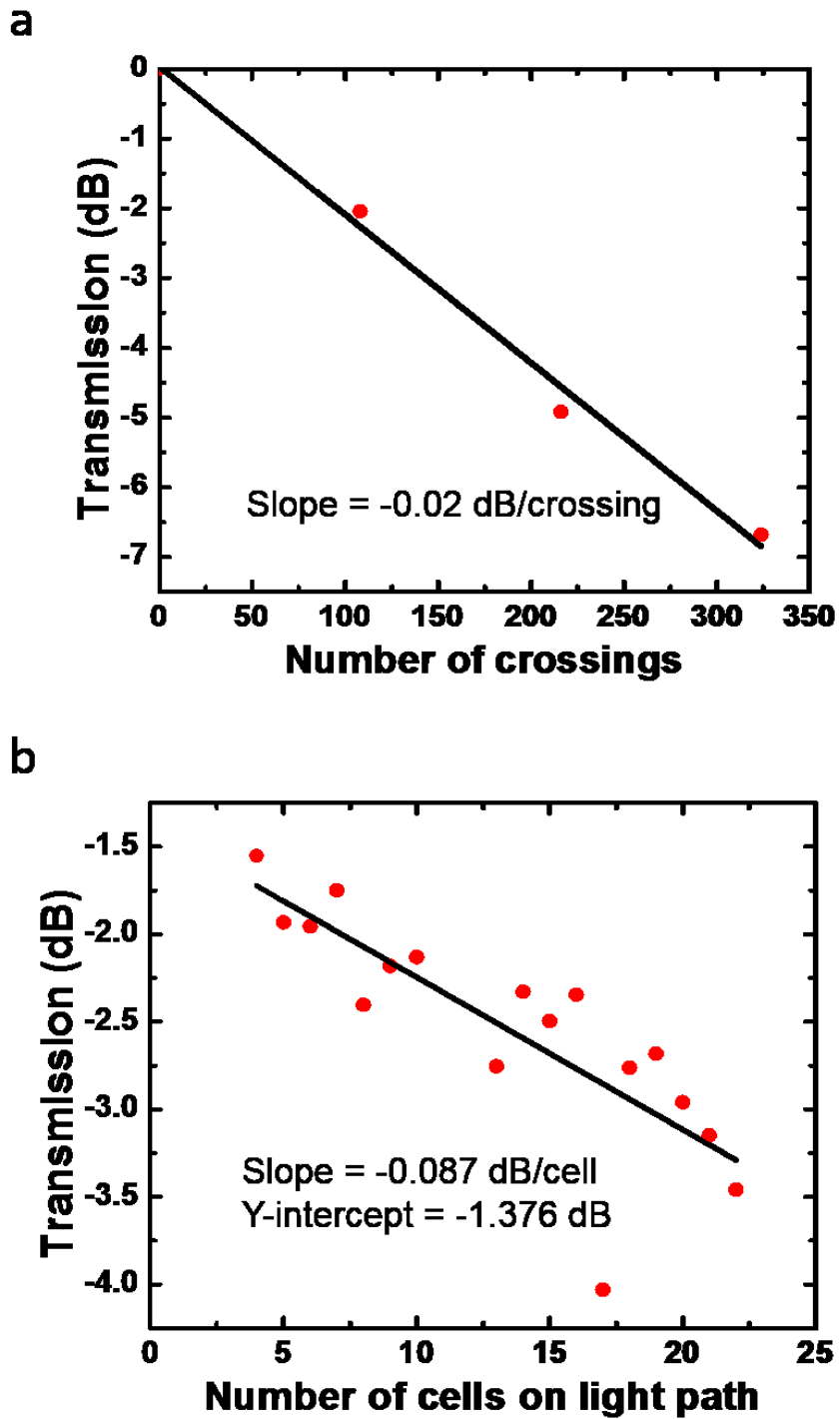
Figure 3.12 Insertion loss measurements at different numbers of waveguide crossings (a), and in 4x20 switch network (b). Modified and reprinted from [85].

To measure loss of waveguide crossings, we measured loss of test structures with 108, 216, and 324 cascaded crossings that were located on the same chip as the switch device (**Error! Reference source not found.** (a)). The loss of a waveguide crossing was extracted by linearly fitting the measured data and it was 0.02 dB. This value is very close to the designed value that is 0.015 dB.

We also measured the insertion loss of 17 measurable cells in the 4th row of the switch to characterize a path dependence of the switch (**Error! Reference source not found.** (b)). By linear fitting of the data, the through-state loss (slope) and the drop-state loss (Y-intercept) were extracted and the corresponding values were 0.087 dB and 1.376 dB respectively. The through-state loss could be much reduced compared to that in the 50x50 switch because the following reasons: (1) increased widths of the waveguides (500 nm VS 350 nm), (2) lower side wall roughness in the waveguides (photoresist reflow process), (3) better dimensional control on the waveguide crossings. The drop-state loss could be reduced because the laterally moving directional coupler has better control on optical coupling than the vertically moving directional coupler. If we were to extend this switch to 50x50 ports, the maximum insertion loss would be less than 10 dB (98 x 0.087 dB + 1.376 dB = 9.902 dB). This value is closer to the theoretical prediction (1.47 dB) than in the loss of the 50x50 switch presented in Chapter 2 (27.5 dB).

3.4 Multicast operation

Optical multicast switches are desirable for use in many applications that require high-bandwidth transmission from one source to multiple destinations, such as video streaming and video conferences. The most widely used approach for multicast optical switches is using a broadcast-and-select approach [84]. In this approach, every sender is sending optical signals to every receiver by default and thus optical power is wasted. It is desirable to have an optical switch that directs optical power from a sender only to receivers that are meant to subscribe to the sender. In this chapter, I discuss the implementation of such switches with laterally moving directional couplers and show experimental demonstrations using the fabricated 4x20 switch.

3.4.1 Multicast operation and corresponding optical loss
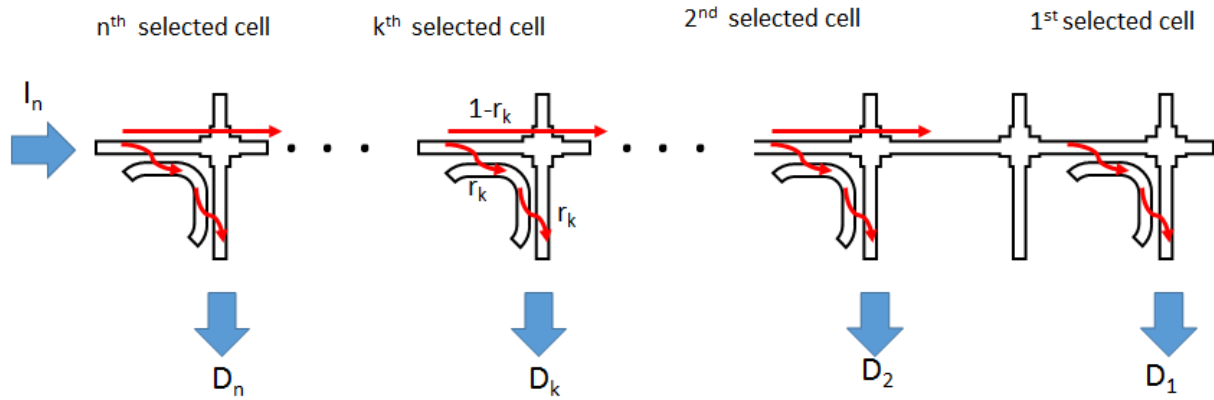
Figure 3.13 Illustration of multicast operation.

Figure 3.13 illustrates multicast operation using our switch. Optical power from the input port (= I_n) is distributed to n selected ports. The optical power entering the kth selected cell is denoted as I_k and the optical power dropped to the kth selected port is denoted as D_k. Because of the symmetry, the coupling ratios (optical-power-sent to drop-port relative to the optical-power-entering-a-directional-coupler) of two-directional couplers in a cell are equal. We denote the coupling ratio of the directional coupler (optical power transferred to drop-port relative to input power) at k^{th} selected cell as r_k. The optical power passed down to k^{th} selected cell can be calculated from the values of the input power (I_n) and the coupling ratios (r_k) of the directional couplers, and it can be expressed as the equation (3.9).

$$I_n * (1 - r_{k+1}) * (1 - r_{k+2}) * \ldots * (1 - r_n)$$

(3.9)

The optical power drop to the kth selected port can be calculated by multiplying the equation (3.9) by square of coupling ratio of the kth selected cell (r_k^2). Thus, the optical power dropped to k^{th} selected port can be expressed by the following equation.

$$D_k = I_n * r_k{}^2 * \prod_{m=k+1}^{n} (1 - r_m) \qquad (3.10)$$

Since the amounts of optical power sent to each selected drop-port are equal, the following equation holds.

$$D_1 = D_2 = \cdots D_{k-1} = D_k = \cdots D_{n-1} = D_n \qquad (3.11)$$

By combining (3.10) and (3.11), we get the following recursive equation.

$$r_{k-1}{}^2 = \frac{r_k{}^2}{1 - r_k} \ (k = 2, 3, \ldots, n) \qquad (3.12)$$

with $r_1 = 1$ because we don't want any power leaving the 1_{st} selected cell. It should be noted that the equation is not dependent on n.

The solutions for (3.12) are listed in Table 3-1 with three decimal places.

Table 3-1 Coupling ratio (r_k) for k^{th} selected cell.

k	1	2	3	4	5	6	7	8	9	10
r_k	1.000	0.618	0.456	0.364	0.304	0.261	0.229	0.204	0.185	0.168

Based on the r_k values in Table 3-1 with the equation (3.10), we can calculate the optical power (relative to the input power, I_n) delivered to each selected port with different number of selected cells. The value is listed in the following table.

Table 3-2 Optical power delivered to each selected port when casting to n ports.

n	1	2	3	4	5	6	7	8	9	10
D_k dB (for any $k \leq n$)	0.00	-4.18	-6.82	-8.79	-10.36	-11.67	-12.80	-13.79	-14.68	-15.48

3.4.2 Cell design which does not waste any optical power when multicasting

The present implementation of the switch sets the coupling ratio of the two directional couplers equal (Figure 3.14 (a)) since the comb-drive actuator can only move in diagonal direction. As a result, there is optical power loss at the output coupler when the value of *r* is less than 1. Ideally, we want the coupling ratio of the output coupler to be either 0 (when not selected) or 1 (when selected) while the coupling ratio of the input coupler can be tuned to a value between 0 and 1

(Figure 3.14 (b)). In this way, we do not waste any optical power, and optical power delivered to each port is 1/*n* when delivering to *n*-ports with equal distributions of the power. Figure 3.15 shows the optical power delivered to each selected port with different numbers of selected ports for the present design and an ideal design. When delivering to 10 ports, the optical power penalty of the present-design compare to the ideal-design is around 5.5 dB. In the future, we can implement the ideal design by using comb drives with 2-axis movement [90,91] to control the coupling ratio of the input coupler and the output coupler independently.
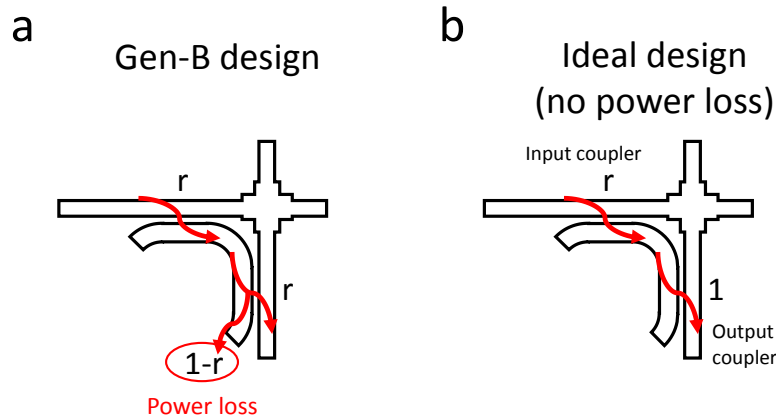
Figure 3.14 Switch implementation. (a) Gen-B design. (b) Ideal design (no power loss).
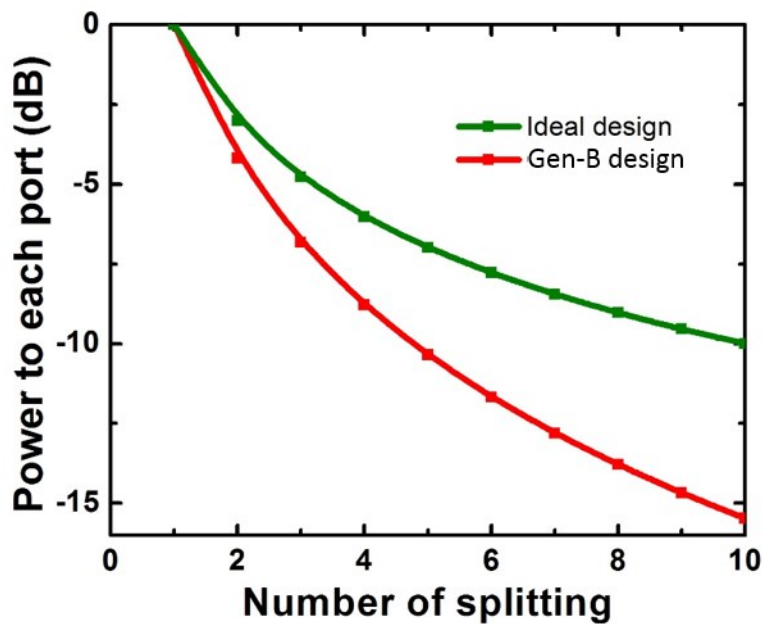
Figure 3.15 Optical power delivered to each port.

3.4.3 Measured point-to-multipoint switching operation

We have measured 1-to-2 and 1-to-4 switching operation with the fabricated switch. Figure 3.16 shows the setup we used to measure the multicast operation. There is a fiber-ribbon aligned to the chip and four of optical-powermeters are connected to column-17, -18, -19, and -20. A continuous-wave-laser-source with a polarization controller is connected to row-4. We used four of DC-voltage-source to bias cell <4,17>, <4,18>, <4,19>, and <4,20>. Figure 3.17 shows the applied voltages and the corresponding optical power casted to output ports. For 1-to-4 multicast, we first tune the voltage of cell-<4,20> to make it at drop-state (coupling ratio of 1). Then tune the voltage of cell-<4,19> until the optical power to column-19 and -20 become equal. Then tune the voltage of cell-<4,18> until all three ports (column-18, -19, -20) have equal power. Finally the voltage applied to cell-<4,17> is tuned until all the optical-powers to the four-ports are at the same value. We used voltage-sources with precision of 0.001 V. One-to-2 switching operation is done with similar manner with 1-to-4 switching operation. The number of selected cells is limited by the number of probe-tip-manipulators we can fit in to the setup. In the future, we can increase the number of selected cells by using probe cards, or by having integrated-control-circuitry on the same chip.
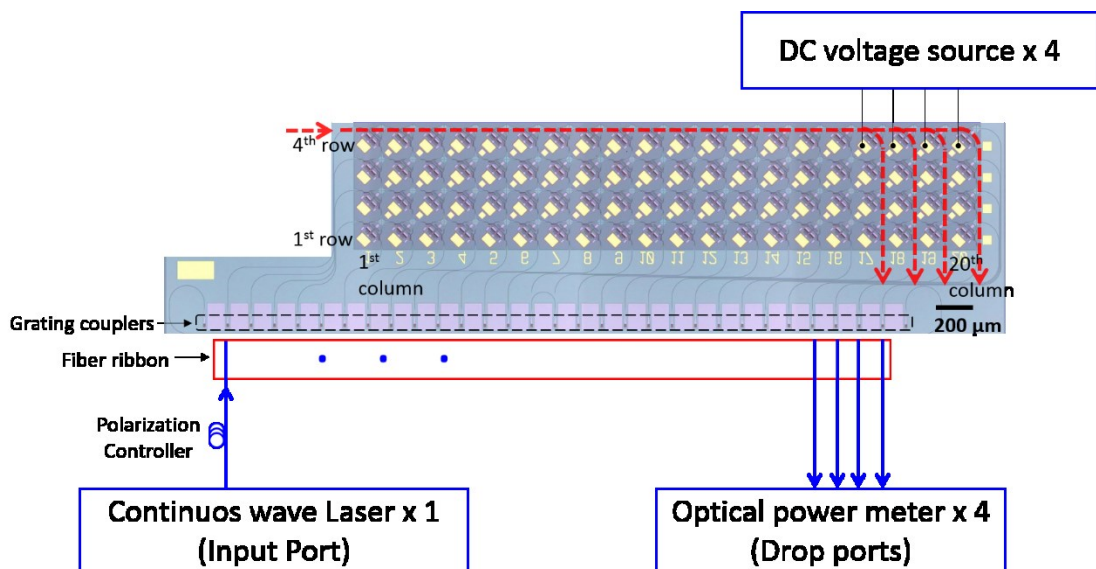
Figure 3.16 Point-to-multipoint operation measurement setup.
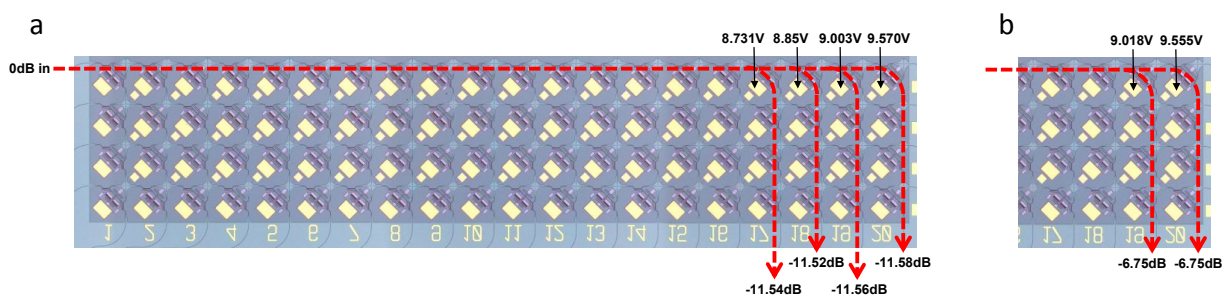
Figure 3.17 Multicast experiment. (a) 1-to-4. (b) 1-to-2. Modified and reprinted from [85].

47

Chapter 4

Silicon-photonic-switch-array on two-layer waveguide-crossbar that can switch any incoming polarization

In most practical cases, optical fibers carry diverse polarizations of light. To make full use of optical fiber's bandwidth capacity, it is desirable to have an optical switch that operates for any incoming polarization. However, demonstrations of silicon photonic switches are mostly limited to single polarization operation. To my knowledge, the demonstration in [92] is the only demonstration of switching any incoming polarization using a silicon photonic switch. However, the demonstration relies on fiber-based polarization beam splitters and combiners.

In this chapter, we present a silicon photonic switch design that can operate for any incoming polarization with low Polarization-Dependent-Loss (PDL). We use two-layer waveguide-crossbar to eliminate the waveguide crossings that have high polarization dependent loss. For switching operation, we use adiabatically tapered waveguide couplers that can switch any incoming polarization. We identify this switch as switch Generation-C.

4.1 Switch design

4.1.1 Three optical layers

a

In Ports

Coupler layer
BUS2 layer
BUS1 layer
Light path

Drop Ports

Through Ports

b

In

Coupler-A

Coupler-B

Through

Large vertical gap

Through-state

c

In

Small vertical gap
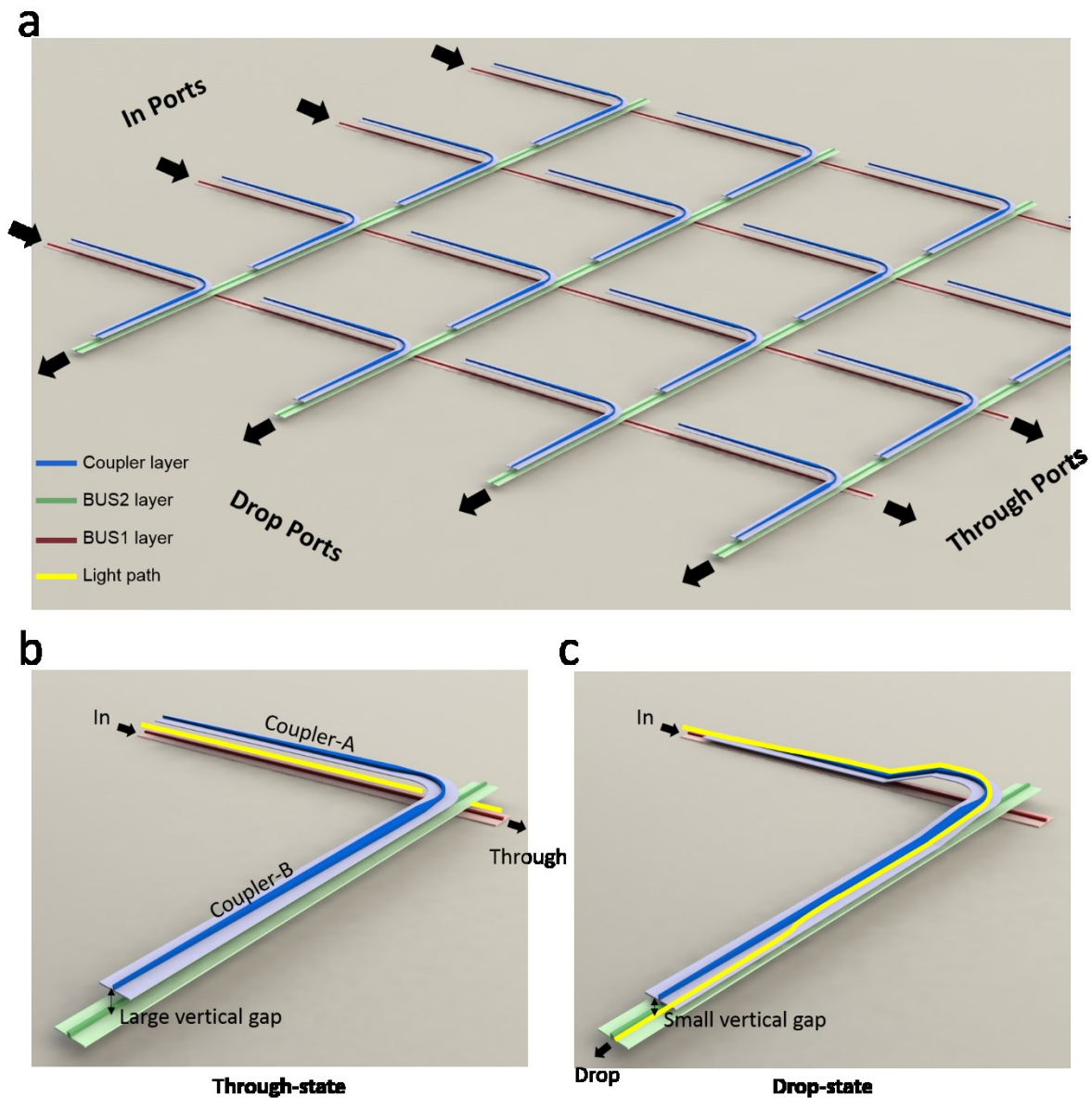
Drop

Drop-state

Figure 4.1 Illustration of the switch. (a) Switch overview. (b) Cell at Drop-state. (c) Cell at Through-state. There are total three optical layers, each colored with red (Bus1), green (Bus2), and blue (Poly-C).

Figure 4.1 shows the structure of the switch. There are three optical layers. There are bus waveguides on the first (Bus1) and the second layer (Bus2), and they form a waveguide crossbar network. On the third layers (Poly-C), there are coupler waveguides that switch the light paths from the through to the drop waveguides. The waveguides are designed to support both

Transverse-Electric (TE) and Transverse-Magnetic (TM) modes. Because the optical-crossbar network is made of two layers, there are no stacked crossings of the waveguides, and thus this design eliminates any optical losses from waveguide crossings. The optical losses in this architecture are only due to propagation losses in the waveguides which can be made very small. Therefore, this architecture is more scalable than the single-layer crossbar architectures that used in Gen-A and Gen-B. For coupling to optical fibers, we use thick oxide waveguides and mode transformers that work for both TE and TM polarization as designed in [93].

There are two waveguide couplers (Coupler-A and Coupler-B) in a switching cell (Figure 4.1 (b)). These couplers are adiabatic-couplers [94–97] instead of directional couplers that we used for Gen-A and Gen-B. As shown in section 3.1.1, directional couplers have a fixed length for a complete power transfer from one waveguide to the other, and the designed fixed lengths are usually different for TE-mode and TM-mode [35]. As a result, it is difficult to design a directional coupler that has high switching efficiency for the both TE- and TM-modes. On the other hand, adiabatic-couplers do not have fixed lengths for a complete power transfer condition. As long as the length of the coupler is longer than a critical length, optical power transfers can be nearly 100 % from a source waveguide to a receiver waveguide in the coupler [94–97]. Thus, by having coupler lengths that are longer than the critical lengths for the both TE- and TM-modes, an optical switch can achieve nearly 100 % power transfer for the both TE- and TM-modes of optical date waves.

Figure 4.1 (b) and (c) show the through-state and drop-state cross sections of a switch cell. When set in the through-state, the coupler waveguides are located far from the Bus1 and Bus2 layers, and light coming from the in-port remains confined to the Bus1 layer and continues to the output through-port without interruption. With the switch in the drop-state, Coupler-A and Coupler-B are positioned at very close distances to the Bus1 layer and the Bus2 layer, respectively. In this configuration, light in the Bus1 layer transfers by evanescent couplings through the waveguide to Coupler-A and propagate to Coupler-B through a 90-degree bend in the guide. There the light is transferred similarly to the Bus2 layer. Switches in the array are selected when the couplers are activated using electrostatic MEMS actuator where it is guided to a drop-port similar to [97].
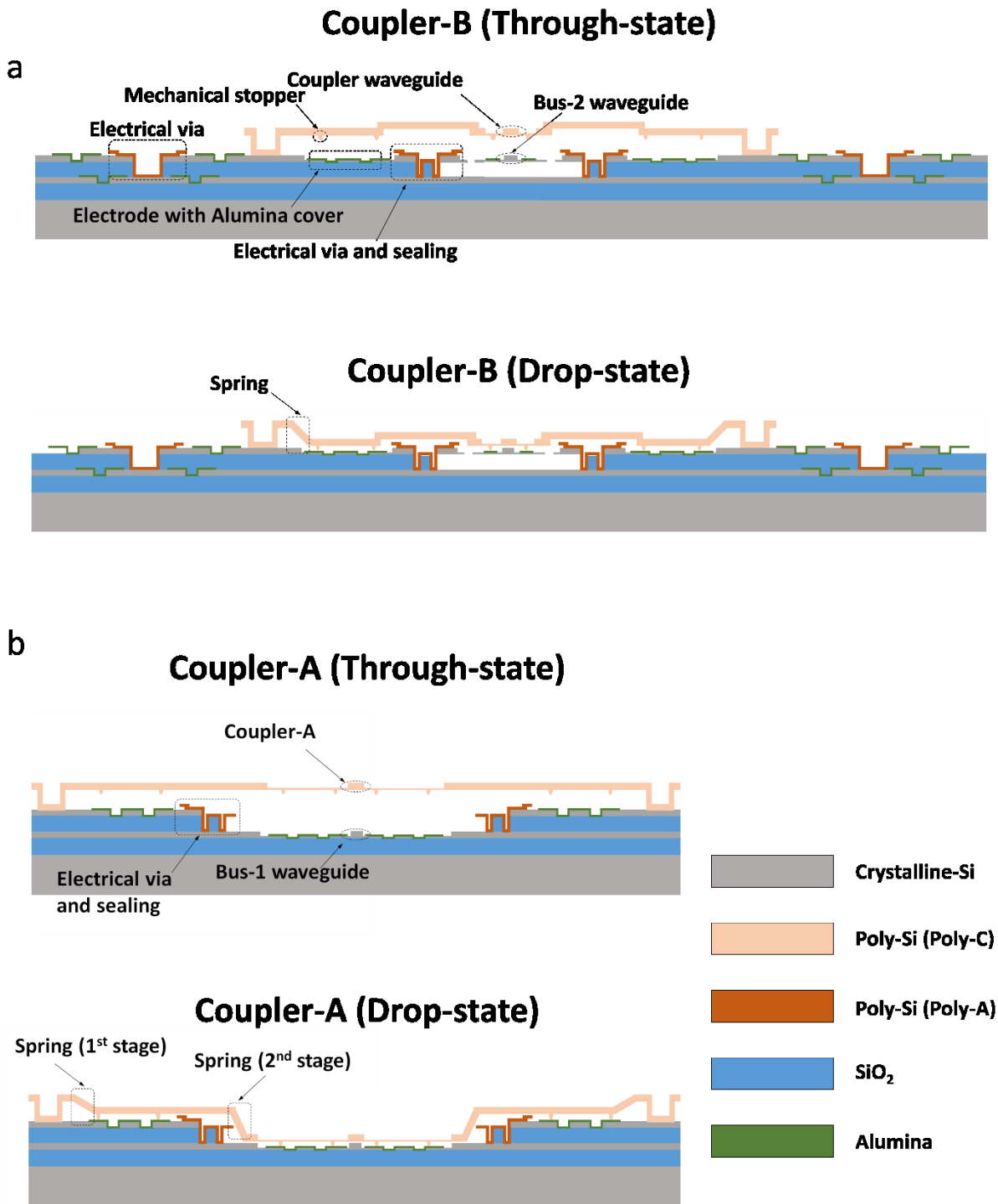
Figure 4.2 Cross-section of Polarization-Independent-Photonic-Switch. (a) Coupler-B. (b) Coupler-A.

Figure 4.2 shows cross sections of the switch. There are three optical layers, Bus1-, Bus2-, and Poly-C-layers. The purpose of the Bus1- and Bus2-layers is to provide waveguide layers for the

waveguide crossbar. The purpose of the Poly-C-layer is to provide a waveguide layer for the couplers. Bus1- and Bus2-layers consist of crystalline silicon while Poly-C-layer consists of poly-silicon. The Bus1-layer overlays a 3 μm-thick buried-oxide layer. The Bus2-layer is located 1 μm above the Bus1-layer and there is either SiO_2 or air between the two layers. Bus1- and Bus-2-layers are electrically connected through electrical vias. Poly-C layer is located 1 μm above BUS2 layer. All the waveguides on Bus1-, Bus2-, and Poly-C-layers are rib type having wings as thick as 100 nm. The detailed dimensions of the waveguides are shown in Chapter 4.1.2 and Chapter 4.1.3. We designed parallel-plate-type electrostatic actuators with folded-springs to move the couplers. By moving the actuator down or up, we can turn the switch on or off. In Chapter 4.1.4, we show details of the actuator design.

4.1.2 Bus waveguide design

We designed waveguides which support the both TE- and TM-modes for polarization diverse operation. The dimensions of the new waveguides for each layer are shown in Table 4-1, and the schematics showing the cross-sections of the waveguides are shown in Figure 4.3 (a) and Figure 4.4 (a). The major difference to the waveguides in Gen-A and Gen-B is the thickness. To have similar optical properties between TE- and TM-modes, we increase the thickness of the waveguide to have it comparable to the width of the waveguide. To have mechanical support, we added wings to the waveguides.

Table 4-1 Dimensions of the waveguides.

	Thickness of wing (nm)	Thickness of core (nm)	Width of core (nm)
Bus1-layer		320	550
Bus2-layer	100	340	550
Poly-C-layer		380	Tapered from 150 to 850
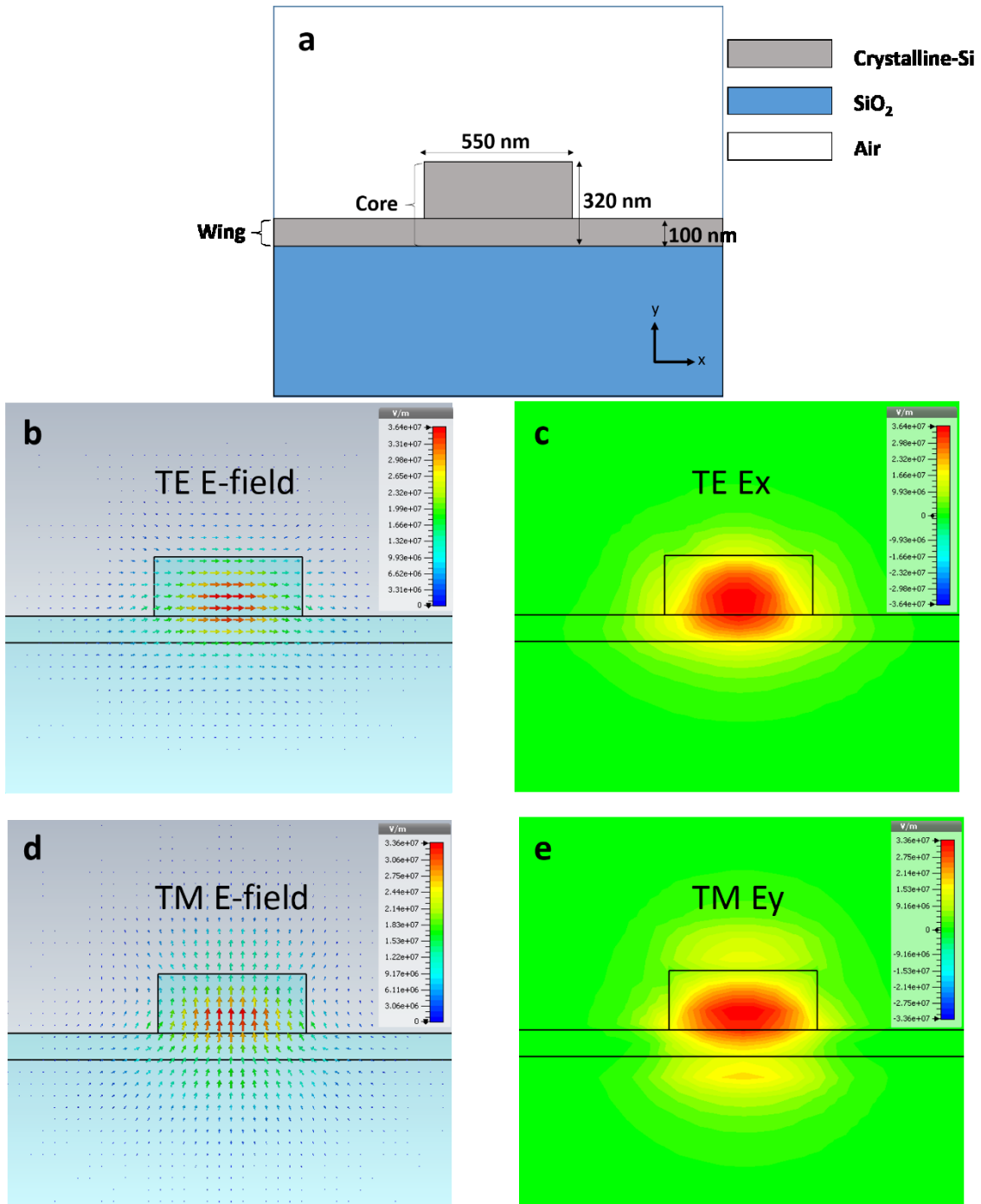
Figure 4.3 Bus1 waveguide design. (a) Dimensions and materials. (b) TE E-field profile. (c) TE Ex field profile. (d) TM E-field profile. (e) TM E_y field profile.
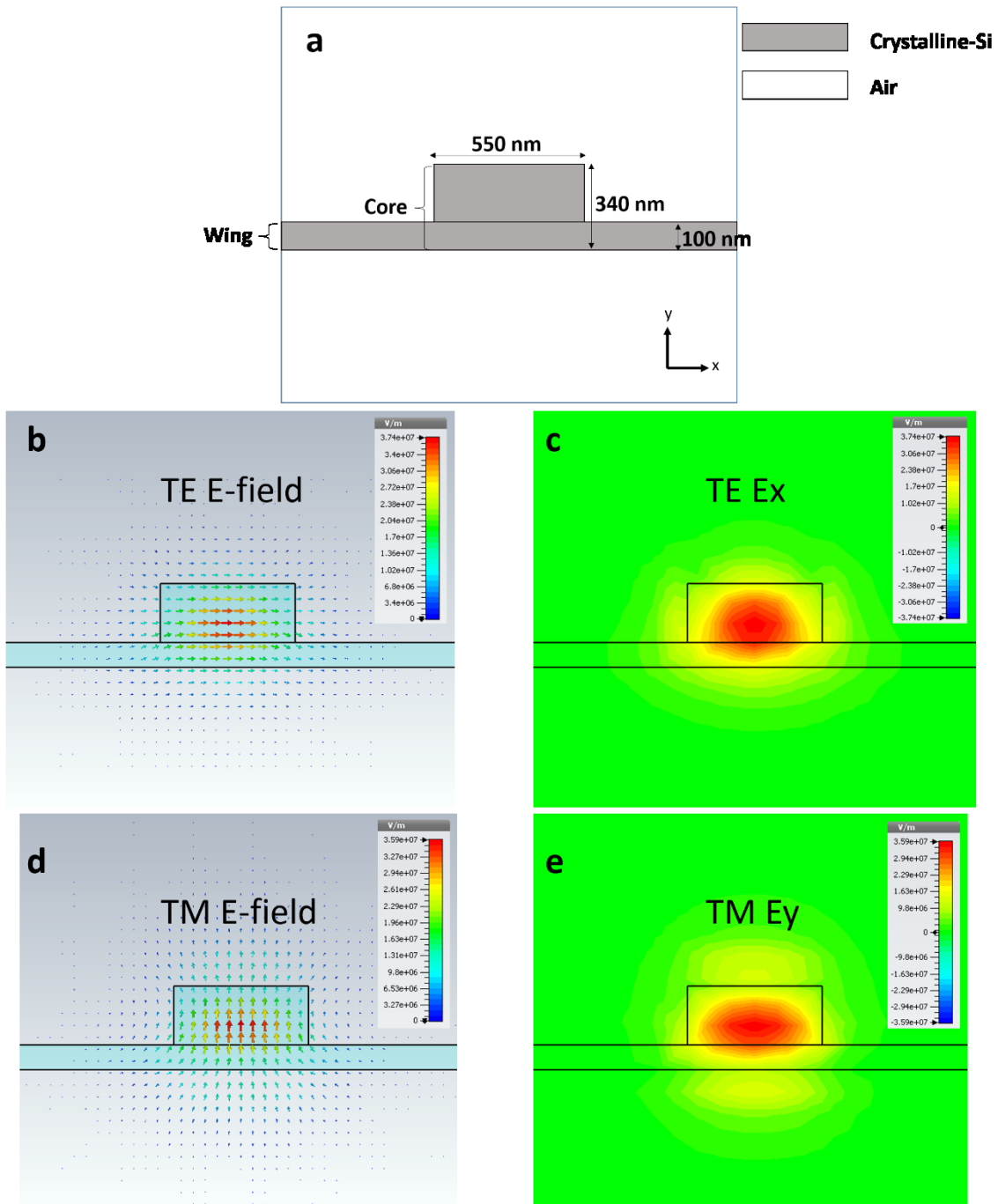
Figure 4.4 Bus2 waveguide design. (a) Dimensions and materials. (b) TE E-field profile. (c) TE Ex field profile. (d) TM E-field profile. (e) TM E_y field profile.

Figure 4.3 (b-e) and Figure 4.4 (b-e) show mode profiles of TE- and TM-modes of Bus1- and Bus-2 waveguides which are simulated using CST STUDIO SUITE [64]. Because the waveguides do not have circular symmetry, there are different group velocities for each of the polarization-modes. The differences in the group velocities between the polarization modes create differing group delays [98,99]. We calculated group indices using CST STUDIO SUITE [64] and the results are

54

shown in the first row of Table 4-2. The group velocities can be calculated from the group indices using equation (4.1).

$$v_g = \frac{c}{n_g}$$

(4.1)

where c, n_g, and v_g denote speed of light, group index, and group velocity respectively.

In each cell, there is a 147 µm-long waveguide. Using the group-index values in Table 4-2 with equation (4.1) and the length of the waveguide (147 µm), we calculated the group delay in a cell for each polarization mode and listed it in the second row of Table 4-2. From the values of the group delay, we calculated differences in group delays between TE- and TM-modes and listed them in the third row of Table 4-2. The differences are -0.29 ps/cell and -0.33 ps/cell for Bus1- and Bus2-waveguides, respectively. In the longest path in a 100x100 switch array, for example, light goes through 99 cells of Bus1-waveguides and 99 cells of Bus2-waveguides. Therefore, the total input-to-output group-delay difference between TE- and TM-modes is 61 ps. However, the differences in group delay can be compensated by electronics such as shown in [100] or by using circularly symmetric waveguides.

Table 4-2 Polarization-mode dispersion at 1550 nm wavelength

	Bus1 TE	Bus1 TM	Bus2 TE	Bus2 TM
Group-index	3.85	4.44	3.87	4.54
Group-delay (ps/cell)	1.89	2.18	1.90	2.23
Difference in group delay of TE- and TM-modes (ps/cell)	-0.29		-0.33	

4.1.3 Vertically moving adiabatic coupler
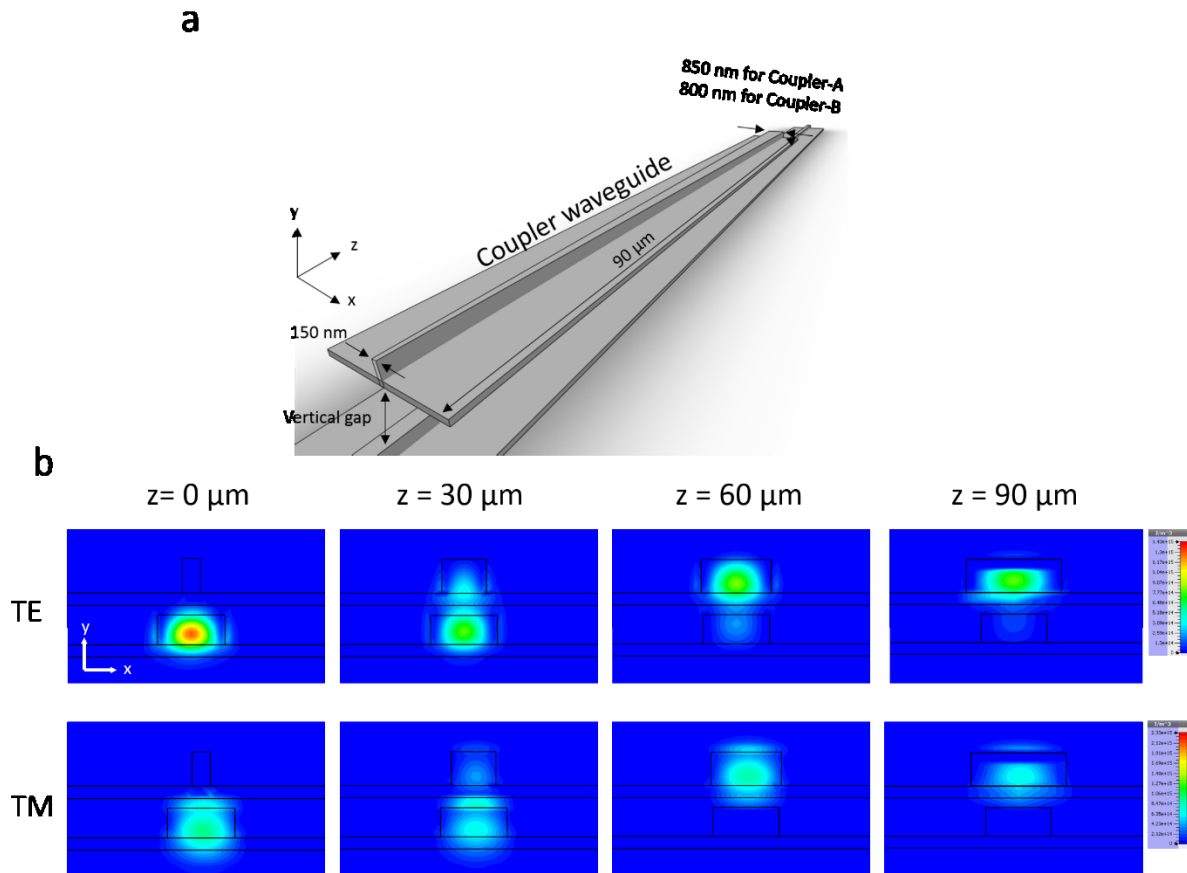
Figure 4.5 Coupler simulations. (a) Coupler dimensions. (b) E_x field profile (TE), and E_y field profile (TM) of Coupler-B with 80 nm coupling gap.

Figure 4.5 (a) shows the geometry of the couplers. The waveguide in when switched-on Coupler-A is designed to have optimal coupling with that in Bus1. Coupler-B is designed similarly with the Bus2 waveguide. Since the Bus1- and Bus2-waveguides have different geometries, there are different designs for Coupler-A. In order for an adiabatic coupler to transfer optical power from one waveguide to the other with nearly 100 % efficiency, an effective-index of the coupler waveguide needs to be smaller than that in the Bus-waveguide at the beginning of the coupler and needs to be bigger than that in the Bus-waveguide at the end of the coupler. To achieve this condition, we designed the thickness of the coupler-waveguide to be 380 nm which is thicker than the Bus-waveguides. At the thin end of the coupler, we reduced the effective index of the coupler below that of the Bus-waveguide by thinning its width to 150 nm. At the other end of the coupler, we increase its width to 800 nm to give it an effective index larger than that of the Bus-waveguides. We fixed the length of the coupler to 90 µm in consideration of making the size of the switch cell smaller than 150x150 um². The reason we chose 150x150 um² as a limit is to integrate a 50x50 switch array in 1 cm² area. To find detailed designs, we ran parameter-sweeps

with full 3D simulations using CST STUDIO SUITE [64]. The swept parameters are lengths of the couplers, the final widths of the couplers, and the gap sizes of the couplers. We found that a maximum-power transfer condition holds when the final widths are 850 nm and 800 nm for Coupler-A and Coupler-B, respectively, with an optimal gap size of 80 nm. The simulated mode-profiles (at 1550 nm wavelength) are shown in Figure 4.5 (b) for Coupler-B. The profiles clearly show the gradual transfer of optical power from the Bus2-waveguide to the coupler-waveguide. Figure 4.6 shows the spectral responses of the couplers at the optimal coupling gap (80 nm). For a spectral range of 300 nm (1400 – 1700 nm), the extinction ratios between the drop-ports and the through-ports are larger than 10 dB, and the optical power sent to the drop-ports are roughly -0.5 dB relative to input power. Figure 4.7 shows the transmission characteristics of the drop-ports of the couplers with various gaps at 1550 nm wavelength. At the optimal spacing (80 nm), the optical power transmitted to the drop-port is larger than -0.25 dB for TE-mode waves and larger than -0.5 dB for TM-mode waves (for both Couplers-A and B). Thus, polarization-dependent loss in the couplers only totals -0.5 dB. The transmission to the drop port decreases as coupling gaps increase, and the optical power transmitted to a drop port is less than -30 dB with gaps larger than 600 nm. Thus a gap of 1000 nm with the switch in the through state is large enough to decouple the Bus-waveguides and the coupler-waveguides. Figure 4.8 shows spectral responses of drop-states with various gap sizes. From Figure 4.8 we see that when gaps are larger than 600 nm, optical power going to a drop-port is less than -25 dB throughout the wavelength range of 1400 to 1700 nm.
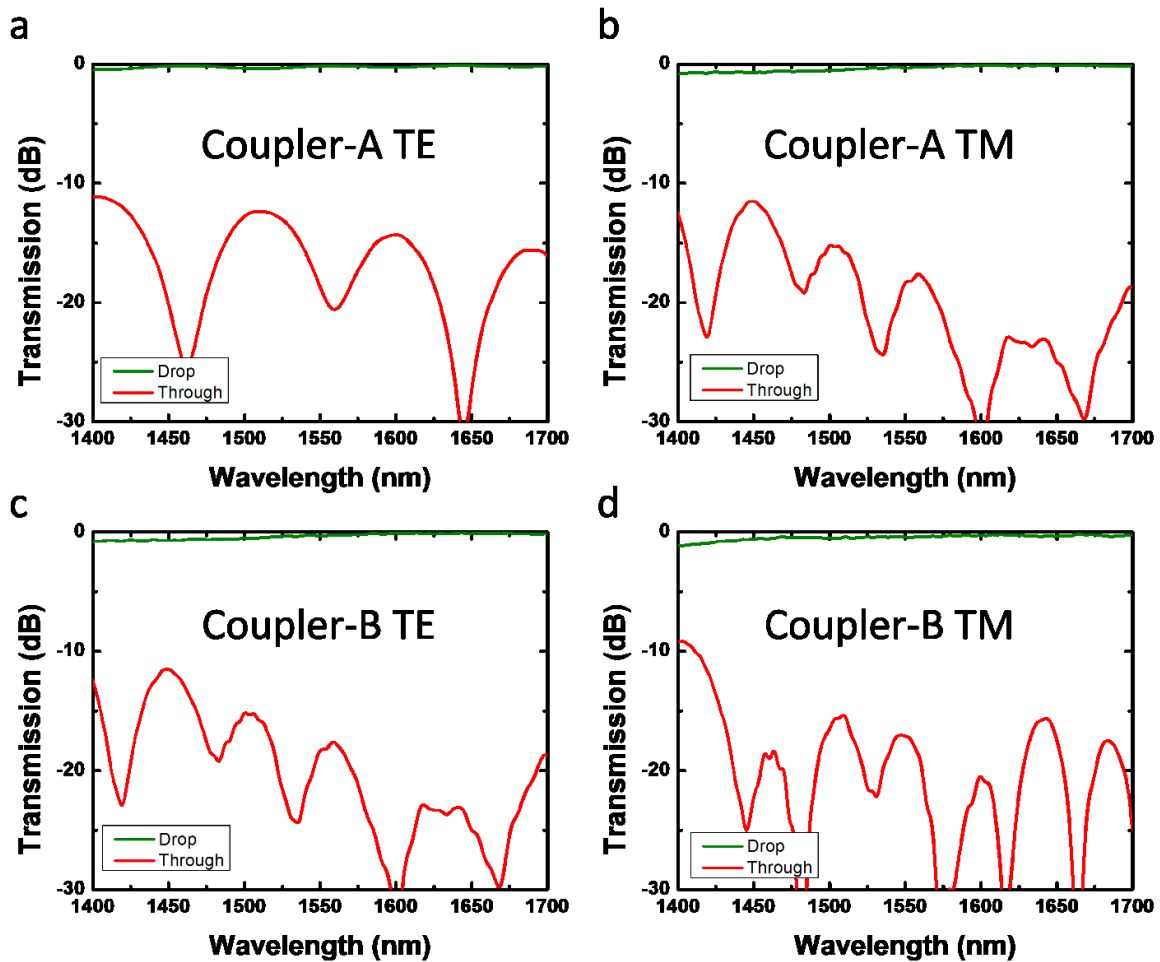
Figure 4.6 Spectral response of the couplers at the optical gap (80 nm). (a) Coupler-A TE. (b) Coupler-A TM. (c) Coupler-B TE. (d) Coupler-B TM.

We ran simulations with differing tip widths to check the effect of increasing widths (Figure 4.9). The simulation result shows that the tip width does not significantly affect the performance of the couplers. For the TE-mode, the power transmitted to a drop port stays above -0.5 dB for most wavelengths (1300 to 1700 nm) when the tip width is less than 300 nm. For the TM-mode, the power transmitted to a drop port stays above -1 dB for most of the wavelength range (1300 to 1700 nm) if the tip width is smaller than 300 nm. The large tolerance can help to relax a complexity of fabrication processes.
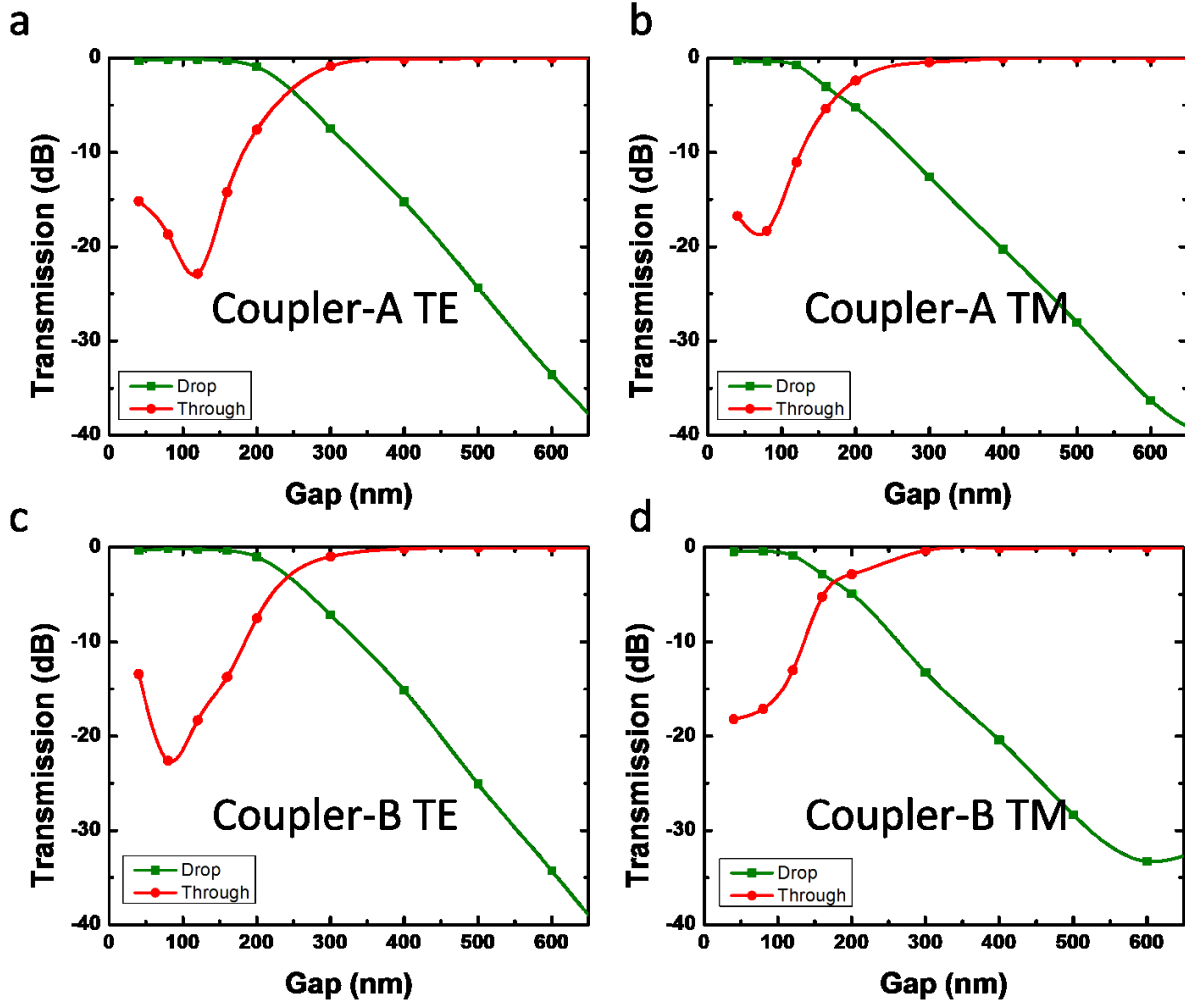
Figure 4.7 Transmission characteristics of the couplers with various gaps. (a) Coupler-A TE. (b) Coupler-A TM. (c) Coupler-B TE. (d) Coupler-B TM.
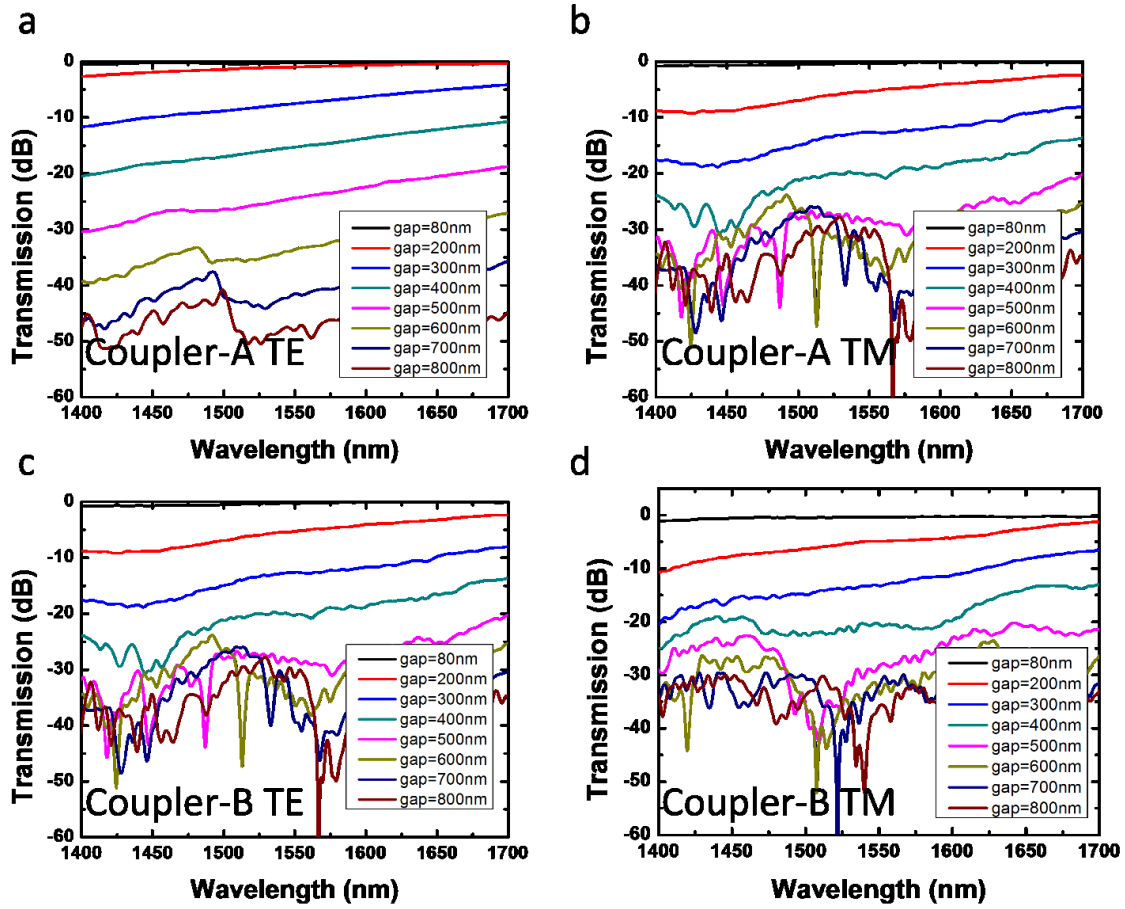
Figure 4.8 Spectral response of drop ports with various gaps. (a) Coupler-A TE. (b) Coupler-A TM. (c) Coupler-B TE. (d) Coupler-B TM.
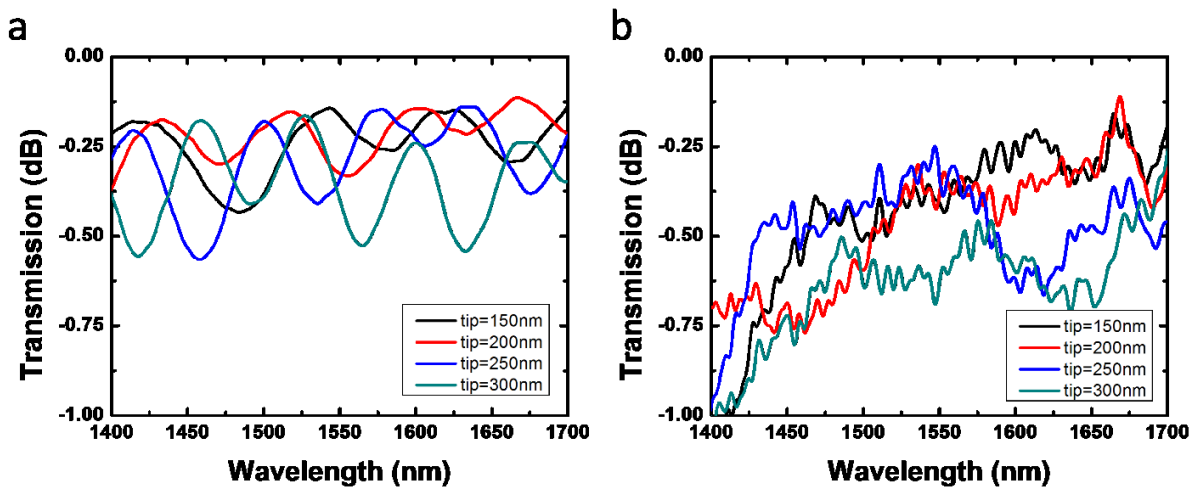
Figure 4.9 Spectral response of coupler-B (drop-port) with varying tip widths. (a) TE mode. (b) TM mode.

4.1.4 Actuator design of Switch Gen-C
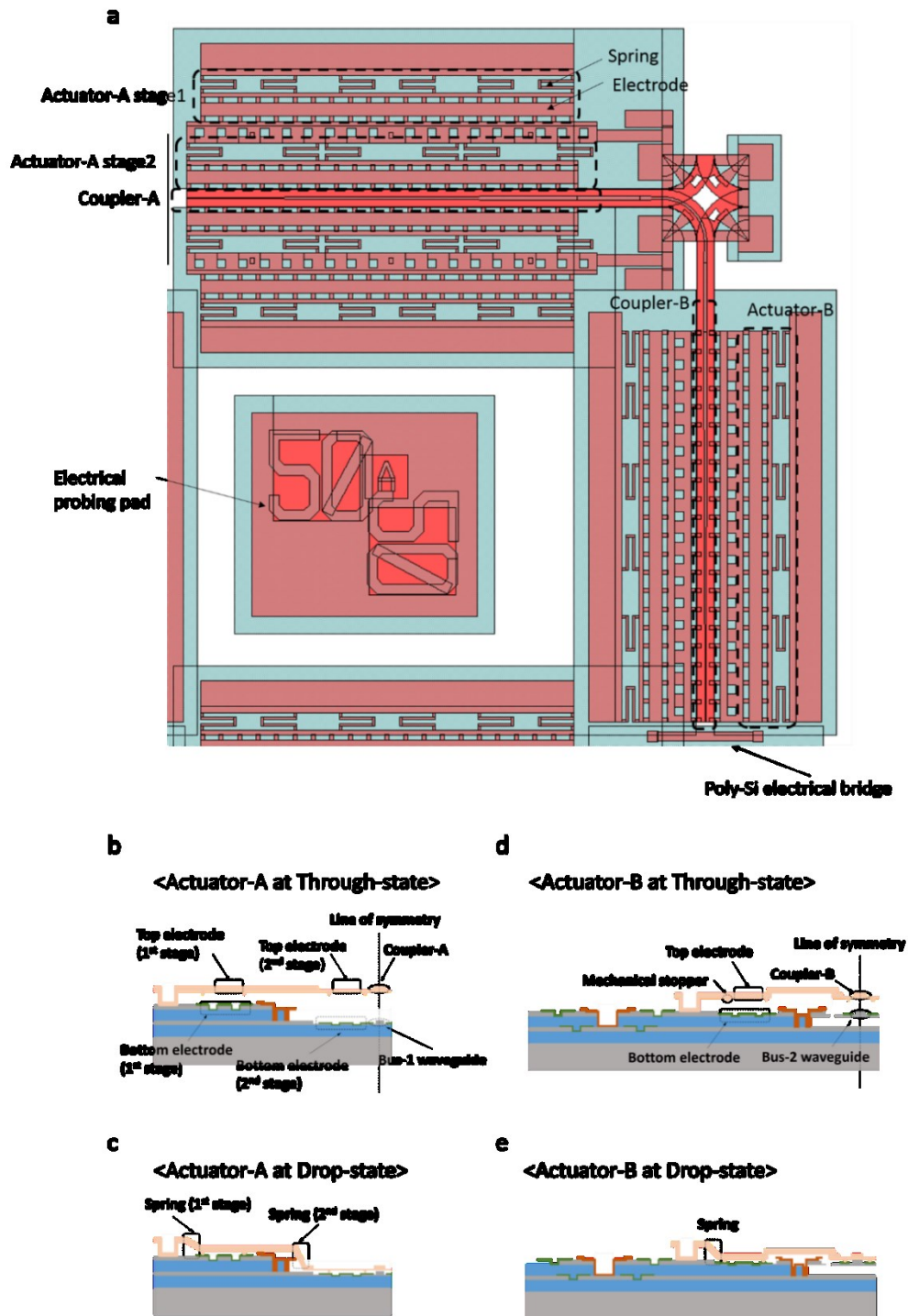
Figure 4.10 Schematics of actuators. (a) Switch cell layout of Poly-C layer. Cross sectional view of Actuator-A at through-state (b), and drop-state (c). Cross sectional view of Actuator-B at through-state (d), and drop-state (e). Figures (b), (c), (d), (e) are copied from the cross-sections in Figure 4.2. Here only the left half of cross-sections are presented.

Figure 4.10 (a) shows the cell layout of the Poly-C layer in the switch area containing the couplers and actuators. The actuators consist of parallel-plate electrodes and folded springs. The cross-sectional view of actuator for coupler-B (Actuator-B) is shown in Figure 4.10 (d), (e). Coupler-B is attached to the top electrodes, and the electrodes are attached to the folded-springs. There are bottom electrodes located under the top electrodes that pull the top electrodes downward when voltage is applied between them. The distance between the two electrodes is 1220 nm in the OFF state. We use the pull-in phenomenon [101] of the parallel-plate actuators to turn the switch on and rely on relaxation of bending stress to turn it off. When the switch is activated, sets of mechanical stoppers prevent the top electrodes from direct contact with the bottom electrodes, and hold the coupling gap to 80 nm. The actuator for coupler-A (Actuator-A) is shown in Figure 4.10 (b), (c). Its actuation gap size is twice as large as the gap for Coupler-B. In order to have both Couplers-A and B to be tuned on at the same drive voltage, we cascaded two actuators that have similar design to Actuator-B. The first stage of the actuator has an actuation gap of 1000 nm. When the first stage of the actuator is pulled down, the actuation gap of the second stage becomes 1640 nm. Therefore, the turn-on actuation gap of the cascaded actuator becomes 1640 nm.

We calculated resonant frequencies and pull-in voltages of the actuators by approximating the actuators as simple parallel-plate-driven structures. We first calculate the spring constants of the actuator springs by using equation (4.2) [88] with the values in Table 4-3.

$$k_{sp} = \frac{Ewt^3}{l^3}$$

(4.2)

Table 4-3 Parameters and corresponding values of the springs.

Parameter	Value
E (Young's modulus of Si)	150 GPa
t (thickness of spring)	220 nm
w (width of spring)	500 nm
l (unfolded length of spring)	19.3 µm

The calculated spring constant is 0.57 N/m. Since there are 12 springs in each actuator stage, the total spring constant of each actuator stage is 6.84 N/m. The resonant frequencies of the actuator stages are calculated using equation (4.3) with k (total spring constant) = 6.84 N/m and, m (the moving mass) has values shown in Table 4-4 as determined from the volume of the moving parts and their densities. The calculated resonant frequencies are listed in Table 4-5.

$$f_{res} = \frac{1}{2\pi}\sqrt{\frac{k}{m}} \qquad (4.3)$$

Table 4-4 Moving mass of the actuator stages.

	Coupler-A 1st stage	Coupler-A 2nd stage	Coupler-B
m (moving mass)	2.48 ng	0.89 ng	1.68 ng

Table 4-5 Resonant frequencies of actuator stages.

	Coupler-A 1st stage	Coupler-A 2nd stage	Coupler-B
f_{res} (resonant frequency)	264 kHz	441 kHz	321 kHz

Next, we calculated the pull-in voltages of the actuator stages using equation (4.4) with values of k = 6.84 N/m, and ε_0 (permittivity of air) = 8.85*10^{-12} F/m. The areas (A) and actuation gaps (d) are listed in Table 4-6. The calculated pull-in voltages are in Table 4-7.

$$V_{PI} = \sqrt{\frac{8}{27\varepsilon_0}\frac{kd^3}{A}} \qquad (4.4)$$

Table 4-6 Areas and actuation gaps of electrodes in each actuator stages.

	Actuator-A 1st stage	Actuator-A 2nd stage	Actuator-B
Area of one electrode	3 μm x 86 μm	3 μm x 90.25 μm	3 μm x 90.25 μm
Total number of electrodes	2	2	2
A (total area of electrode)	516 μm^2	541.5 μm^2	541.5 μm^2
d (Actuation gap)	1000 nm	1640 nm	1220 nm

Table 4-7 Pull-in voltages of actuator stages.

	Coupler-A 1st stage	Coupler-A 2nd stage	Coupler-B
V_{PI}	21 V	43 V	28 V

4.2 Oxide waveguide

We use oxide (SiO_2) waveguides to couple the switch chip to optical fibers. Since the mode-field-diameter of a fiber-core is larger than 10 µm, we use thick and wide waveguides to match the mode sizes. Figure 4.11 shows the cross-sectional view of the oxide waveguide. The thickness and the width of the waveguide are 8 µm and 14 µm respectively. The thick oxide layer is built-up from a combination of the buried-oxide layer of SOI wafer and the intermediate low-temperature-oxide layers. There is an alumina coating surrounding the waveguide to protect it during the HF vapor-release process that ultimately releases the MEMS structures. The silicon substrate under the waveguide is etched away to prevent optical-mode leakage into the substrate. Optical modes coupled to the oxide waveguide are transferred either to Bus1-layer or to Bus2-layer using mode transformers similar to those designed in [93].
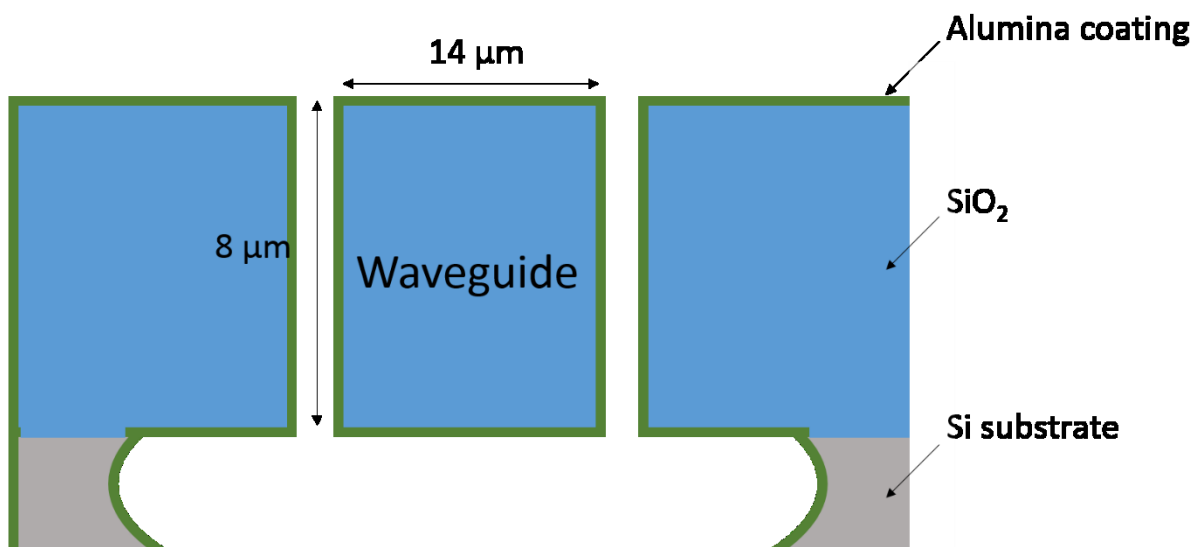
Figure 4.11 Cross-sectional view of oxide waveguide.

4.3 Fabrication of switch Gen-C

Figure 4.12 indicates the fabrication flow for switch Gen-C showing cross sections detailing steps in the process. The fabrication starts with 6'' SOI wafers having 320 nm-thick Si layers and 3 μm-thick BOX layers. The first bus layer (Bus-1) is patterned using dry-etchings and photoresist layers as etch masks. After defining Bus-1, 20 nm-thick alumina is deposited and patterned by wet etching to cover electrical isolation trenches. We transfer the second bus layer (Bus-2) to the wafer by direct wafer bonding to a different SOI wafer. Prior to bonding, LTO is deposited on both wafers and polished down to a 500 nm final thickness on each wafer. The total LTO thickness after bonding is therefore 1000 nm which defines the vertical offset between the Bus-1 and Bus-2 layers. Bus-2 and the second alumina layer are defined by using same processes as were used for Bus-1 and the 1st alumina layer. Electrical vias are then defined to connect the Bus-1 and Bus-2 layers electrically and mechanically. The vias are defined by etching through the 1000 nm thick LTO layer followed by poly-Si deposition and etching (Figure 4.12 Fabrication flow of Low PDL switch. (g), (h), (i)). After defining the vias, we deposit 2500 nm thick LTO and polish it to have thickness of 1400 nm. Then we carry out three steps of lithography and dry-etching to define oxide topology, anchor holes, and dimple holes followed by a 380 nm thick amorphous silicon deposition. To make poly-Si with a low optical loss, we anneal the wafer to reduce its grain size [102]. After annealing, dry etchings define the couplers and the actuators on the poly-Si layer (Poly-C). Then we deposit 2000 nm of LTO, and etch through the whole LTO stack and the BOX layer to define oxide waveguides. We follow this with an isotropic silicon etch to etch the Si substrate beneath the oxide waveguides. Then 100 nm thick alumina is deposited to protect the oxide waveguides and it is patterned to define actuator release windows. A final step is HF vapor etching of LTO to release the actuators and couplers.

Near coupler-B   **Near coupler-A**   **Oxide waveguide**

a

320 nm thick Si (Bus-1)
3 µm thick SiO₂ (BOX)
Si substrate

The fabrication process starts with a SOI wafer with 320 nm thick Si layer and 3 µm thick SiO₂ layer

b

Electrode

Electrode   Waveguide

Bus-1 layer is pattered with two steps of etch to form waveguides and electrodes.

c

Alumina cover

20 nm thick alumina layer is deposited by Atomic Layer Deposition and patterned by wet etching. The purpose of the deposition is to cover the isolation trenches of the electrodes.

d

Bus-2   Bonding interfacial oxide.

340 nm thick Si layer (Bus-2 layer) is transferred to the wafer by direct wafer bonding and consecutive substrate removal. There are total 1000 nm thick Low Temperature Oxide (LTO) at the bonding interface.

e

Electrode   Waveguide   Electrode
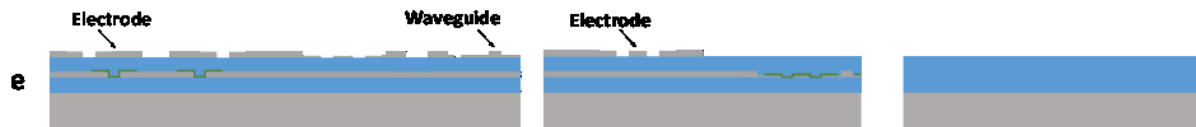
Bus-2 layer is patterned with two steps of etch to define waveguides and electrodes.

f

Alumina cover

20 nm thick Alumina layer is deposited by Atomic Layer Deposition and patterned by wet etching. The purpose of the deposition is to cover the isolation trenches of the electrodes.

100 nm thick LTO

g

100 nm thick LTO is deposited.

Via hole   **Via hole**   **Via hole**

h
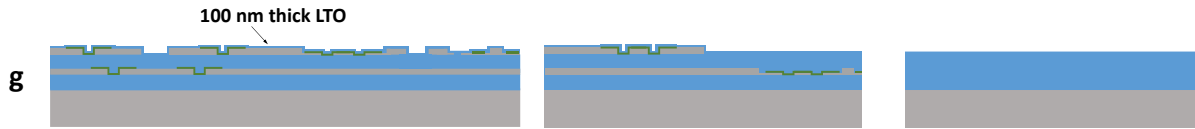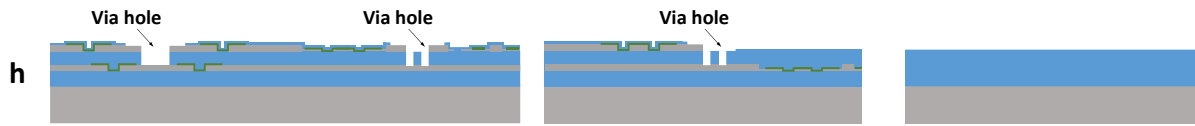
Etch Via holes through the oxide.

Electrical via   **Electrical via & sealing**   **Electrical via & sealing**

i
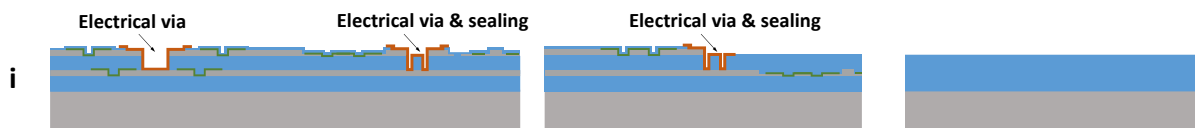
150 nm thick poly-Si is deposited and patterned to define electrical vias and sealings.

1400 nm thick LTO

j
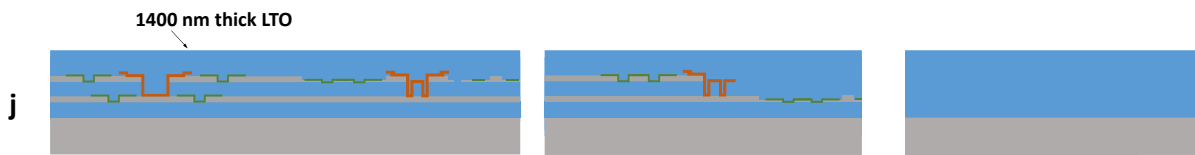
2500 nm thick LTO is deposit and planarized to 1400 nm thick by Chemical Mechanical Polishing (CMP).

Mold of mechanical stopper   **Oxide topology**

Anchor hole

k
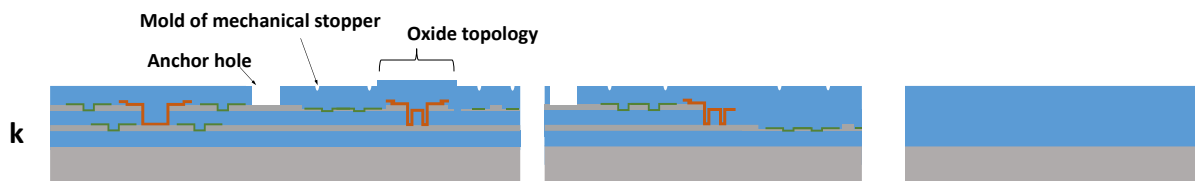
Three steps of etch are done to define oxide topology, mold of mechanical stoppers, and anchor holes.

Mechanical stopper   **Waveguide**

l
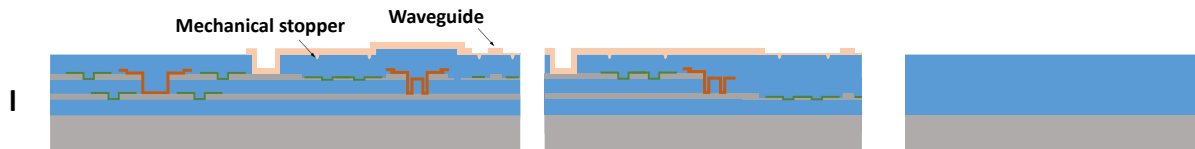
Amorphous-Si is deposited and annealed (final thickness of 380 nm). Then two steps of etch are done to define waveguides and actuators.
*deposition condition: LPCVD, 570ºC.
**annealing condition: N$_2$ environment. 600 ºC, 15 hours + 850 ºC, 1 hour.

2000 nm thick LTO

m

2000 nm of LTO is deposited.

Oxide waveguide

n

Etch through the entire oxide stack to define oxide waveguides.

o

Si substrate is etched by highly selective and isotropic etch.

100 nm thick Alumina

p

100 nm thick Alumina is deposited by ALD and patterned to define Hydrofluoric Acid (HF) vapor release window.

Near coupler-B

Near coupler-A

Oxide waveguide

Oxide waveguide

Line of symmetry

Line of symmetry

Coupler waveguide

Mechanical stopper

Electrical via

q

Electrode with Alumina cover   **Bus-2 waveguide**

Electrical via and sealing

Electrical via and sealing   **Bus-1 waveguide**

Etch oxide layers to release actuators and couplers using HF vapor etch.

Figure 4.12 Fabrication flow of Low PDL switch.

Chapter 5

Conclusions

In this dissertation, I proposed and experimentally demonstrated a new architecture for silicon-photonic-switch-arrays that have a high scalability. In this new architecture, light passes through only a single switching stage regardless of port counts. This is enabled by combining moving waveguides with waveguide crossbars. Using the proposed architecture, a 50x50 silicon-photonic-switch-array was experimentally demonstrated. A vertically moving directional coupler was designed to position waveguide couplers, and ultra-low-loss crossings were designed for unswitched through- and drop-waveguides. This switch, when presented at [103], was the largest port count silicon-photonic-switch-array ever reported. In spite of the large port count, the area of the switch chip was only 9 mm x 9 mm. The switch response time of 2.5 μs is as fast as previously reported for thermo-optic based silicon photonic switches.

After the successful demonstration of the 50x50 switch (Gen-A), I demonstrated a silicon photonic switch (Gen-B) that allows point-to-multipoint connections. A laterally moving directional coupler was used to allow more precise switching operation than was possible with the vertically moving directional coupler used in Gen-A. The laterally moving directional coupler allowed distributing optical power from one port to many ports at the same time. Unlike "broadcast-and-select" method which sends optical power to all destinations, Gen-B switch split optical power only to the destinations which subscribe to the source. In this way, we can deliver more optical power to the destinations.

As a proof of concept, Gen-B was implemented with 4x20 ports. By having a wider waveguide width, optical loss per cell is reduced by nearly a factor of three compared to that of Gen-A switch. If we were to scale Gen-B switch to 50x50 ports, the total optical loss of the switch would be 10 dB. Response time of the switch was 9.6 μs and voltage required for switching was 9.6 V. The lower voltage will make integration with CMOS driving circuit easier.
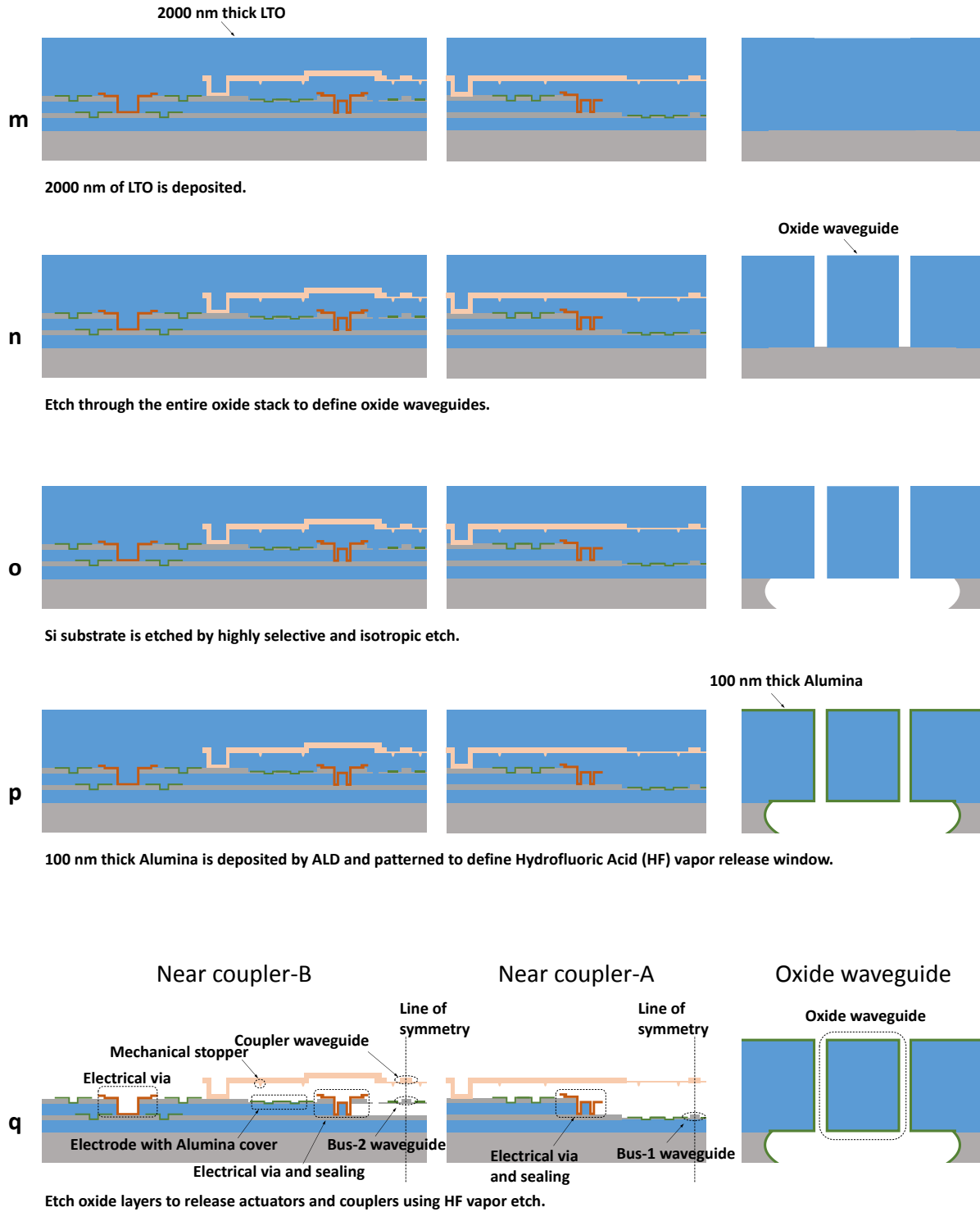
Lastly, I presented a switch design (Gen-C) that can switch any polarization of light and can eliminate optical losses from waveguide crossings. In most of practical applications, optical fibers carry various polarizations of light, and therefore we need optical switches that can switch any incoming polarizations of light. However, most of silicon photonic switches support a single polarization. To have polarization-diverse operation, I designed moving waveguide couplers that can switch both TE- and TM-modes of light wave by using adiabatic coupling methods. Moreover, I designed two-layer waveguide crossbars to eliminate the optical losses induced from waveguide crossings.

Throughout this dissertation, large benefits of using MEMS in silicon photonic switches are shown. However, the benefits shown here demonstrate only a small part of what MEMS can bring to silicon photonics platforms. I believe that MEMS can open up a new paradigm of design for silicon photonic devices in the future. I hope this dissertation can be an initial trigger for this new paradigm.

Bibliography

1.   J. Kim, C. J. Nuzman, B. Kumar, D. F. Lieuwen, J. S. Kraus, A. Weiss, C. P. Lichtenwalner, A. R. Papazian, R. E. Frahm, N. R. Basavanhally, D. A. Ramsey, V. A. Aksyuk, F. Pardo, M. E. Simon, V. Lifton, H. B. Chan, M. Haueis, A. Gasparyan, H. R. Shea, S. Arney, C. A. Bolle, P. R. Kolodner, R. Ryf, D. T. Neilson, and J. V. Gates, "1100 × 1100 port MEMS-based optical crossconnect with 4-dB maximum loss," IEEE Phot. Tech. Lett. **15**, 1537–1539 (2003).

2.   M. Kozhevnikov, N. R. Basavanhally, J. D. Weld, Y. L. Low, P. Kolodner, C. A. Bolle, R. Ryf, A. R. Papazian, A. Olkhovets, F. Pardo, J. Kim, D. T. Neilson, V. A. Aksyuk, and J. V. Gates, "Compact 64 × 64 micromechanical optical cross connect," IEEE Photonics Technol. Lett. **15**, 993–995 (2003).

3.   T. Yamamoto, J. Yamaguchi, N. Takeuchi, A. Shimizu, E. Higurashi, R. Sawada, and Y. Uenishi, "A three-dimensional MEMS optical switching module having 100 input and 100 output ports," IEEE Photonics Technol. Lett. **15**, 1360–1362 (2003).

4.   M. Yano, F. Yamagishi, and T. Tsuda, "Optical MEMS for photonic switching - Compact and stable optical crossconnect switches for simple, fast, and flexible wavelength applications in recent photonic networks," IEEE J. Sel. Top. Quantum Electron. **11**, 383–394 (2005).

5.   W. Mellette and J. E. Ford, "Scaling Limits of Free-Space Tilt Mirror MEMS Switches for Data Center Networks," Opt. Fiber Commun. Conf. **33**, M2B.1 (2015).

6.   C. Sun, M. T. Wade, Y. Lee, J. S. Orcutt, L. Alloatti, M. S. Georgas, A. S. Waterman, J. M. Shainline, R. R. Avizienis, S. Lin, B. R. Moss, R. Kumar, F. Pavanello, A. H. Atabaki, H. M. Cook, A. J. Ou, J. C. Leu, Y.-H. Chen, K. Asanović, R. J. Ram, M. A. Popović, and V. M. Stojanović, "Single-chip microprocessor that communicates directly using light," Nature **528**, 534–538 (2015).

7.   C. Batten, A. Joshi, J. Orcutt, A. Khilo, B. Moss, C. Holzwarth, M. Popovic, H. Li, H. Smith, J. Hoyt, F. Kartner, R. Ram, V. Stojanovic, and K. Asanovic, "Building Manycore Processor-to-DRAM Networks with Monolithic Silicon Photonics," 2008 16th IEEE Symp. High Perform. Interconnects 21–30 (2008).

8.   A. Joshi, C. Batten, Y. Kwon, S. Beamer, I. Shamim, K. Asanovi, and V. Stojanovi, "Silicon-Photonic Clos Networks for Global On-Chip Communication," (2009).

9.   R. Meade, O. Tehar-zahav, J. S. Orcutt, R. Ram, V. Stojanović, and R. Michael, "Integration of Silicon Photonics in a Bulk CMOS Memory Flow," **1**, 114–115 (2013).

10. M. Ruggeri, S. R. Uhlhorn, C. De Freitas, A. Ho, F. Manns, and J.-M. Parel, "Imaging and full-length biometry of the eye during accommodation using spectral domain OCT with an optical switch," Biomed. Opt. Express **3**, 1506 (2012).

11. J. C. F. Matthews, A. Politi, A. Stefanov, and J. L. O'Brien, "Manipulation of multiphoton entanglement in waveguide quantum circuits," Nat. Photonics **3**, 346–350 (2009).

12. K. Bergman, "Silicon Photonics for Exascale Systems Today ' s leading systems (January 2014)," 1–34 (2014).

13. T. Barwicz, H. Byun, F. Gan, C. W. Holzwarth, M. a. Popovic, P. T. Rakich, M. R.

Watts, E. P. Ippen, F. X. Kärtner, H. I. Smith, J. S. Orcutt, R. J. Ram, V. Stojanovic, O. O. Olubuyide, J. L. Hoyt, S. Spector, M. Geis, M. Grein, T. Lyszczarz, and J. U. Yoon, "Silicon photonics for compact, energy-efficient interconnects [Invited]," J. Opt. Netw. **6**, 63 (2007).

14.   T. Baehr-jones, T. Pinguet, P. Lo Guo-qiang, S. Danziger, D. Prather, and M. Hochberg, "Myths and rumours of silicon photonics," **6**, 6–8 (2012).

15.   A. E.-J. Lim, J. Song, Q. Fang, C. Li, X. Tu, N. Duan, K. K. Chen, R. P.-C. Tern, and T.-Y. Liow, "Review of Silicon Photonics Foundry Efforts," IEEE J. Sel. Top. Quantum Electron. **20**, 8300112 (2014).

16.   M. Hochberg, N. C. Harris, R. Ding, Y. Zhang, A. Novack, Z. Xuan, and T. Baehr-Jones, "Silicon photonics: the next fabless semiconductor industry," Solid-State Circuits Mag. IEEE **5**, 48–58 (2013).

17.   M. Hochberg and T. Baehr-Jones, "Towards fabless silicon photonics," Nat. Photonics **4**, 492–494 (2010).

18.   B. Jalali, "Silicon photonics: Nonlinear optics in the mid-infrared," Nat. Photonics **4**, 506–508 (2010).

19.   M. Paniccia and N. Photonics, "Integrating silicon photonics," Nat. Photonics **4**, 498–499 (2010).

20.   K.-W. Ang, T.-Y. Liow, Q. Fang, M. B. Yu, F. F. Ren, S. Y. Zhu, J. Zhang, J. W. Ng, J. F. Song, Y. Z. Xiong, G. Q. Lo, and D.-L. Kwong, "Silicon photonics technologies for monolithic electronic-photonic integrated circuit (EPIC) applications: Current progress and future outlook," 2009 IEEE Int. Electron Devices Meet. 1–4 (2009).

21.   B. Jalali and S. Fathpour, "Silicon Photonics," J. Light. Technol. **24**, 4600–4615 (2006).

22.   R. Soref, L. Fellow, and I. Paper, "The Past , Present , and Future of Silicon Photonics," **12**, 1678–1687 (2006).

23.   G. Li, J. Yao, Y. Luo, H. Thacker, A. Mekis, X. Zheng, J. Lee, K. Raj, J. E. Cunningham, and V. Ashok, "Ultralow-loss, high-density SOI optical waveguide routing for macrochip interconnects," **20**, 12035–12039 (2012).

24.   J. Notaros, F. Pavanello, M. T. Wade, C. M. Gentry, A. Atabaki, L. Alloatti, R. J. Ram, and A. Popovi, "Ultra-Efficient CMOS Fiber-to-Chip Grating Couplers," 2–4 (2016).

25.   G. T. Reed, G. Mashanovich, F. Y. Gardes, and D. J. Thomson, "Silicon optical modulators," Nat. Photonics **4**, 518–526 (2010).

26.   K. Goi, N. Ishikura, H. Ishihara, S. Sakamoto, K. Ogawa, T. Liow, X. Tu, G. Lo, and D. Kwong, "Low-Voltage Silicon Mach-Zehnder Modulator Operating at High Temperatures without Thermo-Electric Cooling," Opt. Fiber Commun. Conf. W2A.23 (2016).

27.   L. Chen and Y. Chen, "Compact, low-loss and low-power 8×8 broadband silicon optical switch," Opt. Express **20**, 18977–18985 (2012).

28.   Y. Shoji, K. Kintaka, S. Suda, H. Kawashima, T. Hasama, and H. Ishikawa, "Low-crosstalk 2 × 2 thermo-optic switch with silicon wire waveguides," Opt. Express **18**, 9071–9075 (2010).

29.   K. Suzuki, K. Tanizawa, T. Matsukawa, G. Cong, S. H. Kim, S. Suda, M. Ohno, T. Chiba, H. Tadokoro, M. Yanagihara, Y. Igarashi, M. Masahara, S. Namiki, and H. Kawashima, "Ultra-compact 8 × 8 strictly-non-blocking Si-wire PILOSS switch," Opt.

Express **22**, 3887–3894 (2014).

30.   G. W. Cong, T. Matsukawa, T. Chiba, H. Tadokoro, M. Yanagihara, M. Ohno, H. Kawashima, H. Kuwatsuka, Y. Igarashi, M. Masahara, and H. Ishikawa, "Large current MOSFET on photonic silicon-on-insulator wafers and its monolithic integration with a thermo-optic 2 × 2 Mach-Zehnder switch," Opt. Express **21**, 6889–6894 (2013).

31.   M. Yang, W. M. J. Green, S. Assefa, J. Van Campenhout, B. G. Lee, C. V. Jahnes, F. E. Doany, C. L. Schow, J. A. Kash, and Y. A. Vlasov, "Non-Blocking 4x4 Electro-Optic Silicon Switch for On-Chip Photonic Networks," **19**, 47–54 (2011).

32.   J. Van Campenhout, W. M. J. Green, S. Assefa, and Y. A. Vlasov, "Low-power, 2×2 silicon electro-optic switch with 110-nm bandwidth for broadband reconfigurable optical networks," Opt. Express **17**, 24020–24029 (2009).

33.   M. W. Pruessner, K. Amarnath, M. Datta, D. P. Kelly, S. Kanakaraju, P. Ho, and R. Ghodssi, "InP-based optical waveguide MEMS switches with evanescent coupling mechanism," J. Microelectromech. Syst. **14**, 1070–1081 (2005).

34.   M. C. M. Lee and M. C. Wu, "MEMS-actuated microdisk resonators with variable power coupling ratios," IEEE Photon. Technol. Lett. **17**, 1034–1036 (2005).

35.   K. Okamoto, *Fandamentals of Optical Waveguides Katsunari Okamoto*, 2nd ed. (Academic Press, 2006).

36.   M. chang M. Lee and M. C. Wu, "Tunable coupling regimes of silicon microdisk resonators using MEMS actuators," Opt. Express **14**, 4703–4712 (2006).

37.   Y. Munemasa and K. Hane, "A compact 1 × 3 silicon photonic waveguide switch based on precise investigation of coupling characteristics of variable-gap coupler," Jpn. J. Appl. Phys. **52**, 06GL15 (2013).

38.   Y. Akihama and K. Hane, "Single and multiple optical switches that use freestanding silicon nanowire waveguide couplers," Light Sci. Appl. **1**, (2012).

39.   P. Dong, W. Qian, S. Liao, H. Liang, C.-C. Kung, N.-N. Feng, R. Shafiiha, J. Fong, D. Feng, A. V Krishnamoorthy, and M. Asghari, "Low loss shallow-ridge silicon waveguides.," Opt. Express **18**, 14474–9 (2010).

40.   Y. Zhang, M. Streshinsky, A. Novack, Y. Ma, S. Yang, A. E.-J. Lim, G.-Q. Lo, T. Baehr-Jones, and M. Hochberg, "A compact and low-loss silicon waveguide crossing for O-band optical interconnect," **8990**, 899002 (2014).

41.   Y. Liu, J. M. Shainline, X. Zeng, and A. Popovi, "Ultra-low-loss CMOS-compatible waveguide crossing arrays based on multimode Bloch waves and imaginary coupling," **39**, 335–338 (2014).

42.   Y. Huang, J. Song, X. Luo, T.-Y. Liow, and G.-Q. Lo, "CMOS compatible monolithic multi-layer Si3N4-on-SOI platform for low-loss high performance silicon photonics dense integration," Opt. Express **22**, 21859 (2014).

43.   K. Shang, S. Pathak, B. Guan, G. Liu, and S. J. B. Yoo, "Low-loss compact multilayer silicon nitride platform for 3D photonic integrated circuits," Opt. Express **23**, 21334 (2015).

44.   T. J. Seok, N. Quack, S. Han, R. S. Muller, and M. C. Wu, "Highly Scalable Digital Silicon Photonic MEMS Switches," J. Light. Technol. **34**, 365–371 (2016).

45.   D. T. Neilson, V. A. Aksyuk, S. Arney, N. R. Basavanhally, K. S. Bhalla, D. J. Bishop, B. A. Boie, C. A. Bolle, J. V Gates, A. M. Gottlieb, J. P. Hickey, N. A. Jackman, P. R. Kolodner, S. K. Korotky, B. Mikkelsen, F. Pardo, G. Raybon, R.

Ruel, R. E. Scotti, T. W. Van Blarcum, L. Zhang, and C. R. Giles, "Fully Provisioned 112x112 Micro-Mechanical Optical Crossconnect With 35.8Tb/s Demonstrated Capacity," Opt. Fiber Commun. Conf. Postdeadline (2000).

46. "Calient's S320 Optical Circuit Switch," www.calient.net.
47. "Polatis Series 6000 Optical Switch," www.polatis.com.
48. S. Sohma, T. Watanabe, N. Ooba, M. Itoh, T. Shibata, and H. Takahashi, "Silica-based PLC Type 32 x 32 Optical Matrix Switch," 2006 Eur. Conf. Opt. Commun. 1– 2 (2006).
49. R. Varrazza, I. B. Djordjevic, and S. Yu, "Active Vertical-Coupler-Based Optical Crosspoint Switch Matrix for Optical Packet-Switching Applications," J. Light. Technol. **22**, 2034–2042 (2004).
50. K. A. Williams, G. F. Roberts, T. Lin, R. V. Penty, I. H. White, M. Glick, and D. McAuley, "Integrated optical 2 x 2 switch for wavelength multiplexed interconnects," IEEE J. Sel. Top. Quantum Electron. **11**, 78–85 (2005).
51. L. Hui, M. Takagi, H. Imaizumi, and H. Morikawa, "Preliminary demonstration of hybrid optical switching node with dynamic wavelength resource allocation using SOA switch," 2009 14th Optoelectron. Commun. Conf. OECC 2009 1–2 (2009).
52. M. J. R. Heck, H. Chen, A. W. Fang, B. R. Koch, S. Member, D. Liang, H. Park, M. N. Sysak, and J. E. Bowers, "Hybrid Silicon Photonics for Optical Interconnects," Quantum **17**, 333–346 (2011).
53. D. Liang, G. Roelkens, R. Baets, and J. E. Bowers, "Hybrid Integrated Platforms for Silicon Photonics," Materials (Basel). **3**, 1782–1802 (2010).
54. J. S. Orcutt, B. Moss, C. Sun, J. Leu, M. Georgas, J. Shainline, E. Zgraggen, H. Li, J. Sun, M. Weaver, S. Urošević, M. Popović, R. J. Ram, and V. Stojanović, "Open foundry platform for high-performance electronic-photonic integration.," Opt. Express **20**, 12222–32 (2012).
55. J. S. Orcutt, A. Khilo, C. W. Holzwarth, M. a Popović, H. Li, J. Sun, T. Bonifield, R. Hollingsworth, F. X. Kärtner, H. I. Smith, V. Stojanović, and R. J. Ram, "Nanophotonic integration in state-of-the-art CMOS foundries," Opt. Express **19**, 2335–46 (2011).
56. P. Dumon, S. Member, W. Bogaerts, V. Wiaux, J. Wouters, S. Beckx, J. Van Campenhout, D. Taillaert, B. Luyssaert, P. Bienstman, and D. Van Thourhout, "Low-Loss SOI Photonic Wires and Ring Resonators Fabricated With Deep UV Lithography," **16**, 1328–1330 (2004).
57. W. Bogaerts and S. K. Selvaraja, "Compact Single-Mode Silicon Hybrid Rib/Strip Waveguide With Adiabatic Bends," IEEE Photonics J. **3**, 422–432 (2011).
58. A. V Rylyakov, C. L. Schow, B. G. Lee, W. M. J. Green, S. Assefa, F. E. Doany, M. Yang, J. Van Campenhout, C. V Jahnes, J. A. Kash, and Y. A. Vlasov, "Silicon photonic switches hybrid-integrated with CMOS drivers," IEEE J. Solid-State Circuits **47**, 345–354 (2012).
59. B. G. Lee, A. V Rylyakov, W. M. J. Green, S. Assefa, C. W. Baks, R. Rimolo-donadio, D. M. Kuchta, M. H. Khater, T. Barwicz, C. Reinholm, E. Kiewra, S. M. Shank, C. L. Schow, and Y. A. Vlasov, "Monolithic silicon integration of scaled photonic switch fabrics, CMOS logic, and device driver circuits," J. Light. Technol. **32**, 743–751 (2014).
60. A. Biberman, K. Preston, G. Hendry, N. Sherwood-Droz, J. Chan, J. S. Levy, H.

Wang, M. Lipson, and K. Bergman, "CMOS-Compatible Scalable Photonic Switch Architecture Using 3D-Integrated Deposited Silicon Materials for High-Performance Data Center Networks," Opt. Fiber Commun. Conf. Fiber Opt. Eng. Conf. 2011 OMM2 (2011).

61. D. Taillaert, F. Van Laere, M. Ayre, W. Bogaerts, D. Van Thourhout, P. Bienstman, and R. Baets, "Grating Couplers for Coupling between Optical Fibers and Nanophotonic Waveguides," Jpn. J. Appl. Phys. **45**, 6071–6077 (2006).

62. A. Mekis, S. Gloeckner, G. Masini, A. Narasimha, T. Pinguet, S. Sahni, P. De Dobbelaere, and A. L. Components, "A Grating-Coupler-Enabled CMOS Photonics Platform," **17**, 597–608 (2011).

63. S. Han, T. J. Seok, N. Quack, B.-W. Yoo, and M. C. Wu, "Large-scale silicon photonic switches with movable directional couplers," Optica **2**, 1–6 (2015).

64. "CST STUDIO SUITE," www.cst.com.

65. R. T. Chen, H. Nguyen, and M. C. Wu, "A high-speed low-voltage stress-induced micromachined 2 x 2 optical switch," **11**, 1396–1398 (1999).

66. W. Young, R. Budynas, and A. Sadegh, *Roark's Formulas for Stress and Strain*, 8th ed. (McGraw-Hill, 2011).

67. G. J. O. Brien, D. J. Monk, and L. Lin, "MEMS cantilever beam electrostatic pull-in model," Proc. SPIE **4593**, 31–41 (2001).

68. T. K. Chan, M. Megens, B. W. Yoo, J. Wyras, C. J. Chang-Hasnain, M. C. Wu, and D. A. Horsley, "Optical beamsteering using an 8 × 8 MEMS phased array with closed-loop interferometric phase control," Opt. Express **21**, 2807–2815 (2013).

69. S. Pamidighantam, R. Puers, K. Baert, and H. a. C. Tilmans, "Pull-in voltage analysis of electrostatically actuated beam structures with fixed-fixed and fixed-free end conditions," J. Micromechanics Microengineering **12**, 458–464 (2002).

70. D. J. Bell, T. J. Lu, N. A. Fleck, and S. M. Spearing, "MEMS actuators and sensors: observations on their performance and selection for purpose," J. Micromechanics Microengineering **15**, S153 (2005).

71. W. Osten, *Optical Inspection of Microsystems* (CRC Press, 2006).

72. P. Castellini, M. Martarelli, and E. P. Tomasini, "Laser Doppler Vibrometry: Development of advanced solutions answering to technology's needs," Mech. Syst. Signal Process. **20**, 1265–1285 (2006).

73. S. K. Selvaraja, W. Bogaerts, and D. Van Thourhout, "Loss reduction in silicon nanophotonic waveguide micro-bends through etch profile improvement," Opt. Commun. **284**, 2141–2144 (2011).

74. D. K. Sparacin, S. J. Spector, and L. C. Kimerling, "Silicon waveguide sidewall smoothing by wet chemical oxidation," J. Light. Technol. **23**, 2455–2461 (2005).

75. Y. A. Vlasov and S. McNab, "Losses in single-mode silicon-on-insulator strip waveguides and bends," Opt. Express **12**, 1622–31 (2004).

76. J. Cardenas, C. B. Poitras, J. T. Robinson, K. Preston, L. Chen, and M. Lipson, "Low loss etchless silicon photonic waveguides," Opt. Express **17**, 4752–7 (2009).

77. T. Alasaarela, D. Korn, L. Alloatti, A. Säynätjoki, A. Tervonen, R. Palmer, J. Leuthold, W. Freude, and S. Honkanen, "Reduced propagation loss in silicon strip and slot waveguides coated by atomic layer deposition," Opt. Express **19**, 11529–38 (2011).

78. S. K. Selvaraja, S. Member, P. Jaenen, and W. Bogaerts, "Fabrication of Photonic

Wire and Crystal Circuits in Silicon-on-Insulator Using 193-nm Optical Lithography," **27**, 4076–4083 (2009).

79.   M. Gnan, S. Thoms, D. S. Macintyre, R. M. D. La Rue, and M. Sorel, "Fabrication of low-loss photonic wires in silicon-on-insulator using hydrogen silsesquioxane electron-beam resist," Electron. Lett. **44**, (2008).

80.   W. Bogaerts, R. Baets, P. Dumon, V. Wiaux, S. Beckx, D. Taillaert, B. Luyssaert, J. Van Campenhout, P. Bienstman, and D. Van Thourhout, "Nanophotonic waveguides in silicon-on-insulator fabricated with CMOS technology," J. Light. Technol. **23**, 401–412 (2005).

81.   G. N. Rouskas, "Optical layer multicast: Rationale, building blocks, and challenges," IEEE Netw. **17**, 60–65 (2003).

82.   R. Malli, X. Zhang, and C. Qiao, "Benefits of Multicasting in All-Optical Networks," SPIE 3531, All-Optical Netw. Archit. Control. Manag. Issues **3531**, 209–220 (1998).

83.   P. Samadi, V. Gupta, J. Xu, H. Wang, G. Zussman, and K. Bergman, "Optical multicast system for data center networks," Opt. Express **23**, 22162 (2015).

84.   T. Watanabe, K. Suzuki, and T. Takahashi, "Silica-based PLC Transponder Aggregators for Colorless, Directionless, and Contentionless ROADM," OFC/NFOEC Tech. Dig. OTh3D.1 (2012).

85.   S. Han, T. J. Seok, C. K. Kim, R. S. Muller, and M. C. Wu, "Multicast 4x20 Silicon Photonic MEMS Switches," 4– (2015).

86.   Z. Zhou, Z. Wang, and L. Lin, *Microsystems and Nanotechnology*, 1st ed. (Springer-Verlag Berlin Heidelberg, 2012).

87.   S. D. Senturia, *Microsystem Design*, 1st ed. (Springer US, 2001).

88.   H. Search, C. Journals, A. Contact, M. Iopscience, and I. P. Address, "Comb-drive actuators for large displacements," **320**, (n.d.).

89.   S. T. S. Cheung, B. Guan, S. S. Djordjevic, K. Okamoto, and S. J. B. Yoo, "Low-loss and high contrast silicon-on-insulator (SOI) arrayed waveguide grating," Conf. Lasers Electro-Optics Techincal Dig. (2012).

90.   K. Laszczyk, S. Bargiel, C. Gorecki, J. Krel, P. Dziuban, M. Kujawińska, D. Callet, and S. Frank, "A two directional electrostatic comb-drive X-Y micro-stage for MOEMS applications," Sensors Actuators, A Phys. **163**, 255–265 (2010).

91.   Y. Sun, D. Piyabongkarn, A. Sezen, B. J. Nelson, and R. Rajamani, "A high-aspect-ratio two-axis electrostatic microactuator with extended travel range," Sensors Actuators, A Phys. **102**, 49–60 (2002).

92.   K. Tanizawa, K. Suzuki, K. Ikeda, S. Namiki, and H. Kawashima, "Novel polarization diversity without switch duplication of a Si-wire PILOSS optical switch," Opt. Express **24**, 6861 (2016).

93.   Q. Fang, J. Song, X. Luo, M. Yu, G. Lo, and Y. Liu, "Mode-size converter with high coupling efficiency and broad bandwidth.," Opt. Express **19**, 21588–94 (2011).

94.   A. F. Milton and W. K. Burns, "Mode Coupling in Tapered Optical Waveguide Structures and Electro-Optic Switches," IEEE Trans. Circuits Syst. **26**, 1020–1028 (1979).

95.   A. F. Milton and W. K. Burns, "Tapered velocity couplers for integrated optics: design.," Appl. Opt. **14**, 1207–1212 (1975).

96.   T. A. Ramadan, R. Scarmozzino, and R. M. Osgood, "Adiabatic couplers: design rules and optimization," J. Light. Technol. **16**, 277–283 (1998).

97. T. J. Seok, N. Quack, S. Han, R. S. Muller, and M. C. Wu, "Large-scale broadband digital silicon photonic switches with vertical adiabatic couplers," Optica **3**, 64–70 (2016).

98. E. Dulkeith, F. Xia, L. Schares, W. M. J. Green, and Y. a Vlasov, "Group index and group velocity dispersion in silicon-on-insulator photonic wires.," Opt. Express **14**, 3853–3863 (2006).

99. S. T. Lim, C. E. Png, E. a Ong, and Y. L. Ang, "Single mode, polarization-independent submicron silicon waveguides based on geometrical adjustments.," Opt. Express **15**, 11061–11072 (2007).

100. D. Crivelli, M. Hueda, H. Carrer, J. Zachan, V. Gutnik, M. Del Barco, R. Lopez, G. Hatcher, J. Finochietto, M. Yeo, A. Chartrand, N. Swenson, P. Voois, and O. Agazzi, "A 40nm CMOS single-chip 50Gb/s DP-QPSK/BPSK transceiver with electronic dispersion compensation for coherent optical channels," Dig. Tech. Pap. - IEEE Int. Solid-State Circuits Conf. **55**, 328–329 (2012).

101. S. Krylov, B. R. Ilic, D. Schreiber, S. Seretensky, and H. Craighead, "The pull-in behavior of electrostatically actuated bistable microstructures," J. Micromechanics Microengineering **18**, 055026 (2008).

102. D. Kwong, J. Covey, A. Hosseini, Y. Zhang, X. Xu, and R. T. Chen, "Ultralow-loss polycrystalline silicon waveguides and high uniformity 1x12 MMI fanout for 3D photonic integration," Opt. Express **20**, 21722 (2012).

103. S. Han, T. J. Seok, N. Quack, B. Yoo, and M. C. Wu, "Monolithic 50x50 MEMS Silicon Photonic Switches with Microsecond Response Time," Opt. Fiber Commun. Conf. M2K.2 (2014).